Chapter 4

Feature detection and matching

4.1 Points and patches 207
4.1.1 Feature detectors 209
4.1.2 Feature descriptors 222
4.1.3 Feature matching 225
4.1.4 Feature tracking 235
4.1.5 *Application*: Performance-driven animation 237
4.2 Edges 238
4.2.1 Edge detection 238
4.2.2 Edge linking 244
4.2.3 *Application*: Edge editing and enhancement 249
4.3 Lines 250
4.3.1 Successive approximation 250
4.3.2 Hough transforms 251
4.3.3 Vanishing points 254
4.3.4 *Application*: Rectangle detection 257
4.4 Additional reading 257
4.5 Exercises 259

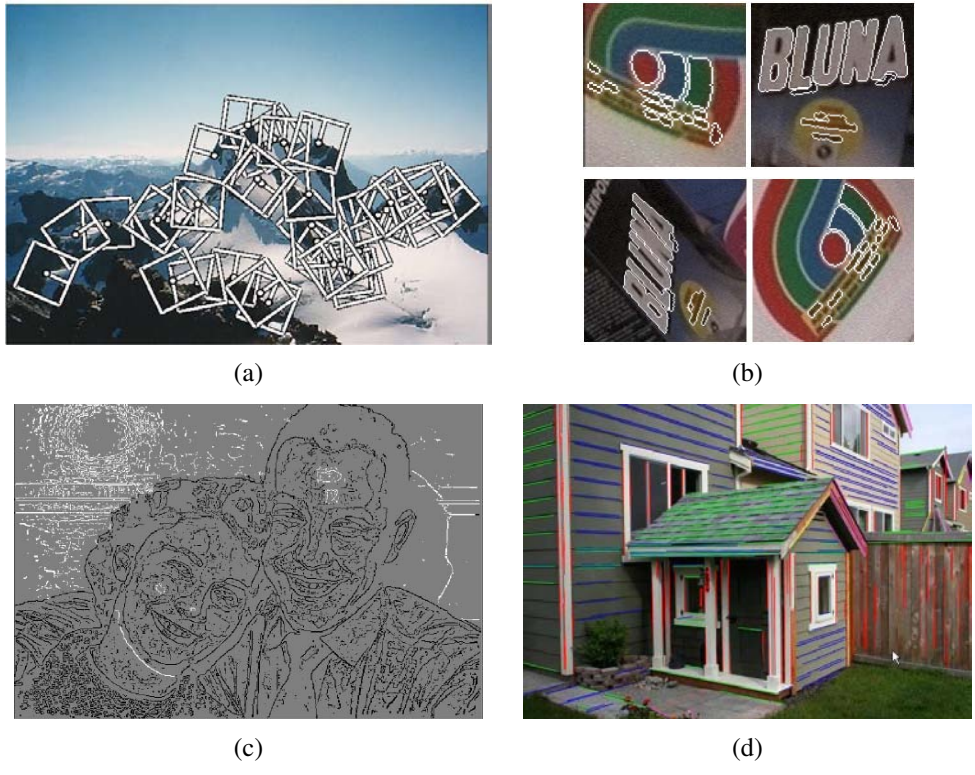

Figure 4.1 A variety of feature detectors and descriptors can be used to analyze, describe and match images: (a) point-like interest operators (Brown, Szeliski, and Winder 2005) © 2005 IEEE; (b) region-like interest operators (Matas, Chum, Urban *et al.* 2004) © 2004 Elsevier; (c) edges (Elder and Goldberg 2001) © 2001 IEEE; (d) straight lines (Sinha, Steedly, Szeliski *et al.* 2008) © 2008 ACM.

Feature detection and matching are an essential component of many computer vision applications. Consider the two pairs of images shown in Figure 4.2. For the first pair, we may wish to *align* the two images so that they can be seamlessly stitched into a composite mosaic (Chapter 9). For the second pair, we may wish to establish a dense set of *correspondences* so that a 3D model can be constructed or an in-between view can be generated (Chapter 11). In either case, what kinds of *features* should you detect and then match in order to establish such an alignment or set of correspondences? Think about this for a few moments before reading on.

The first kind of feature that you may notice are specific locations in the images, such as mountain peaks, building corners, doorways, or interestingly shaped patches of snow. These kinds of localized feature are often called *keypoint features* or *interest points* (or even *corners*) and are often described by the appearance of patches of pixels surrounding the point location (Section 4.1). Another class of important features are *edges*, e.g., the profile of mountains against the sky, (Section 4.2). These kinds of features can be matched based on their orientation and local appearance (edge profiles) and can also be good indicators of object boundaries and *occlusion* events in image sequences. Edges can be grouped into longer *curves* and *straight line segments*, which can be directly matched or analyzed to find *vanishing points* and hence internal and external camera parameters (Section 4.3).

In this chapter, we describe some practical approaches to detecting such features and also discuss how feature correspondences can be established across different images. Point features are now used in such a wide variety of applications that it is good practice to read and implement some of the algorithms from (Section 4.1). Edges and lines provide information that is complementary to both keypoint and region-based descriptors and are well-suited to describing object boundaries and man-made objects. These alternative descriptors, while extremely useful, can be skipped in a short introductory course.

4.1 Points and patches

Point features can be used to find a sparse set of corresponding locations in different images, often as a pre-cursor to computing camera pose (Chapter 7), which is a prerequisite for computing a denser set of correspondences using stereo matching (Chapter 11). Such correspondences can also be used to align different images, e.g., when stitching image mosaics or performing video stabilization (Chapter 9). They are also used extensively to perform object instance and category recognition (Sections 14.3 and 14.4). A key advantage of keypoints is that they permit matching even in the presence of clutter (occlusion) and large scale and orientation changes.

Feature-based correspondence techniques have been used since the early days of stereo

Figure 4.2 Two pairs of images to be matched. What kinds of feature might one use to establish a set of *correspondences* between these images?

matching (Hannah 1974; Moravec 1983; Hannah 1988) and have more recently gained popularity for image-stitching applications (Zoghlami, Faugeras, and Deriche 1997; Brown and Lowe 2007) as well as fully automated 3D modeling (Beardsley, Torr, and Zisserman 1996; Schaffalitzky and Zisserman 2002; Brown and Lowe 2003; Snavely, Seitz, and Szeliski 2006).

There are two main approaches to finding feature points and their correspondences. The first is to find features in one image that can be accurately *tracked* using a local search technique, such as correlation or least squares (Section 4.1.4). The second is to independently detect features in all the images under consideration and then *match* features based on their local appearance (Section 4.1.3). The former approach is more suitable when images are taken from nearby viewpoints or in rapid succession (e.g., video sequences), while the latter is more suitable when a large amount of motion or appearance change is expected, e.g., in stitching together panoramas (Brown and Lowe 2007), establishing correspondences in *wide baseline stereo* (Schaffalitzky and Zisserman 2002), or performing object recognition (Fergus, Perona, and Zisserman 2007).

In this section, we split the keypoint detection and matching pipeline into four separate stages. During the *feature detection* (extraction) stage (Section 4.1.1), each image is searched for locations that are likely to match well in other images. At the *feature description* stage (Section 4.1.2), each region around detected keypoint locations is converted into a more compact and stable (invariant) *descriptor* that can be matched against other descriptors. The

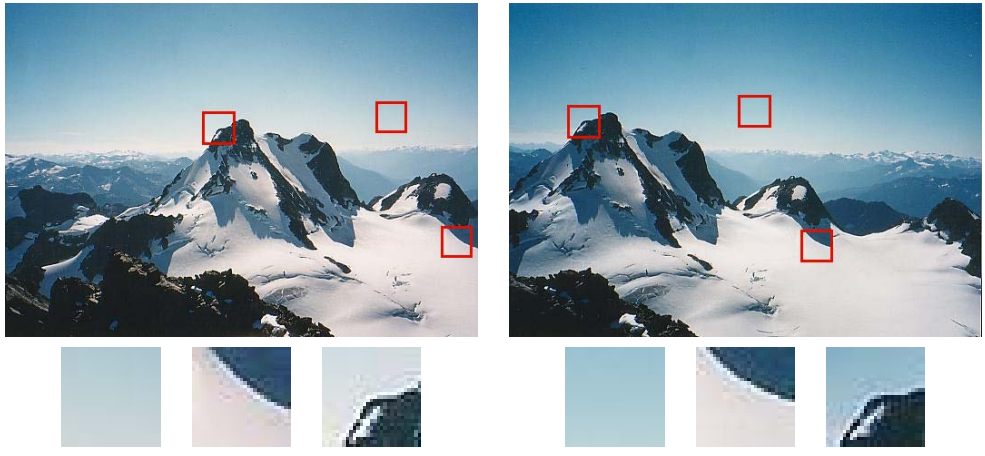

Figure 4.3 Image pairs with extracted patches below. Notice how some patches can be localized or matched with higher accuracy than others.

feature matching stage (Section 4.1.3) efficiently searches for likely matching candidates in other images. The *feature tracking* stage (Section 4.1.4) is an alternative to the third stage that only searches a small neighborhood around each detected feature and is therefore more suitable for video processing.

A wonderful example of all of these stages can be found in David Lowe's (2004) paper, which describes the development and refinement of his *Scale Invariant Feature Transform* (SIFT). Comprehensive descriptions of alternative techniques can be found in a series of survey and evaluation papers covering both feature detection (Schmid, Mohr, and Bauckhage 2000; Mikolajczyk, Tuytelaars, Schmid *et al.* 2005; Tuytelaars and Mikolajczyk 2007) and feature descriptors (Mikolajczyk and Schmid 2005). Shi and Tomasi (1994) and Triggs (2004) also provide nice reviews of feature detection techniques.

4.1.1 Feature detectors

How can we find image locations where we can reliably find correspondences with other images, i.e., what are good features to track (Shi and Tomasi 1994; Triggs 2004)? Look again at the image pair shown in Figure 4.3 and at the three sample *patches* to see how well they might be matched or tracked. As you may notice, textureless patches are nearly impossible to localize. Patches with large contrast changes (gradients) are easier to localize, although straight line segments at a single orientation suffer from the *aperture problem* (Horn and Schunck 1981; Lucas and Kanade 1981; Anandan 1989), i.e., it is only possible to align the patches along the direction *normal* to the edge direction (Figure 4.4b). Patches with

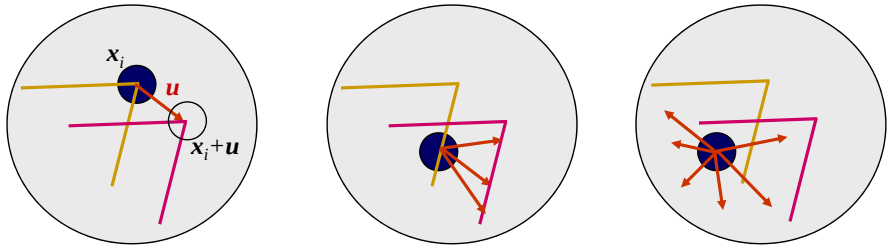

Figure 4.4 Aperture problems for different image patches: (a) stable ("corner-like") flow; (b) classic aperture problem (barber-pole illusion); (c) textureless region. The two images I_0 (yellow) and I_1 (red) are overlaid. The red vector $\boldsymbol{u}$ indicates the displacement between the patch centers and the $w(\boldsymbol{x}_i)$ weighting function (patch window) is shown as a dark circle.

gradients in at least two (significantly) different orientations are the easiest to localize, as shown schematically in Figure 4.4a.

These intuitions can be formalized by looking at the simplest possible matching criterion for comparing two image patches, i.e., their (weighted) summed square difference,

$$E_{\mathrm{WSSD}}(\boldsymbol{u}) = \sum_i w(\boldsymbol{x}_i)[I_1(\boldsymbol{x}_i + \boldsymbol{u}) - I_0(\boldsymbol{x}_i)]^2, \tag{4.1}$$

where I_0 and I_1 are the two images being compared, $\boldsymbol{u} = (u, v)$ is the *displacement* vector, $w(\boldsymbol{x})$ is a spatially varying weighting (or window) function, and the summation i is over all the pixels in the patch. Note that this is the same formulation we later use to estimate motion between complete images (Section 8.1).

When performing feature detection, we do not know which other image locations the feature will end up being matched against. Therefore, we can only compute how stable this metric is with respect to small variations in position $\Delta\boldsymbol{u}$ by comparing an image patch against itself, which is known as an *auto-correlation function* or *surface*

$$E_{\mathrm{AC}}(\Delta\boldsymbol{u}) = \sum_i w(\boldsymbol{x}_i)[I_0(\boldsymbol{x}_i + \Delta\boldsymbol{u}) - I_0(\boldsymbol{x}_i)]^2 \tag{4.2}$$

(Figure 4.5).[1] Note how the auto-correlation surface for the textured flower bed (Figure 4.5b and the red cross in the lower right quadrant of Figure 4.5a) exhibits a strong minimum, indicating that it can be well localized. The correlation surface corresponding to the roof edge (Figure 4.5c) has a strong ambiguity along one direction, while the correlation surface corresponding to the cloud region (Figure 4.5d) has no stable minimum.

[1] Strictly speaking, a correlation is the *product* of two patches (3.12); I'm using the term here in a more qualitative sense. The weighted sum of squared differences is often called an *SSD surface* (Section 8.1).

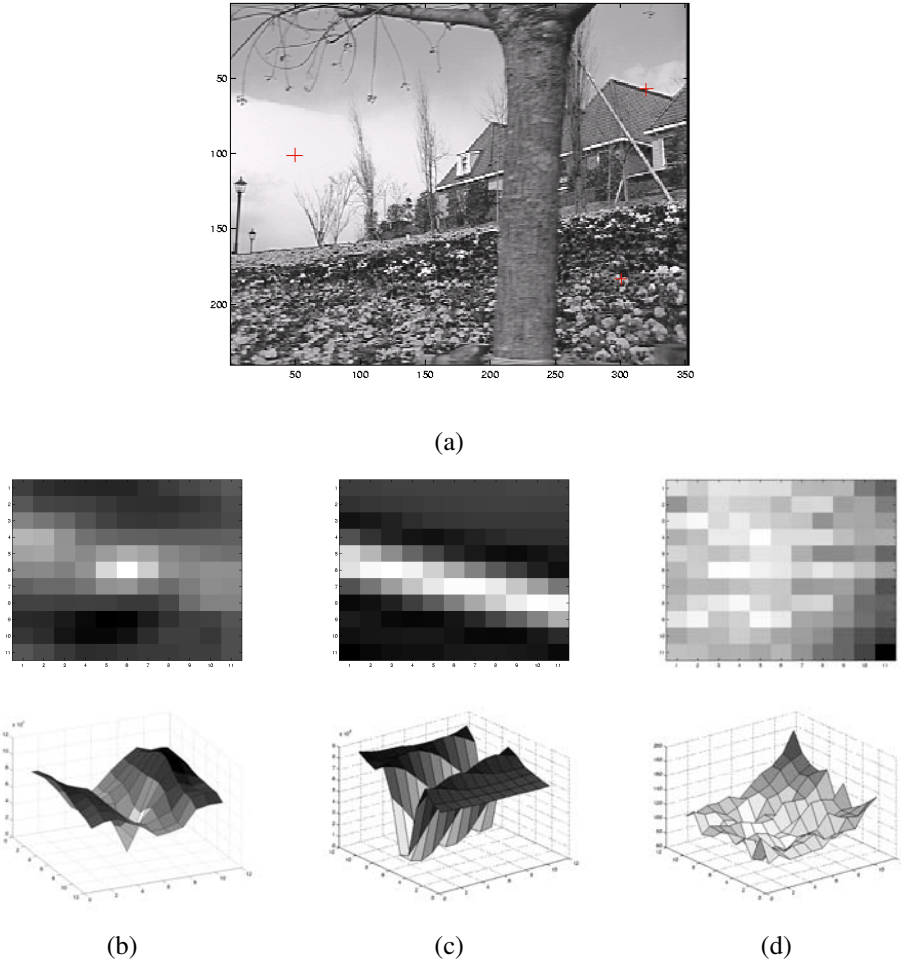

Figure 4.5 Three auto-correlation surfaces $E_{\mathrm{AC}}(\Delta \boldsymbol{u})$ shown as both grayscale images and surface plots: (a) The original image is marked with three red crosses to denote where the auto-correlation surfaces were computed; (b) this patch is from the flower bed (good unique minimum); (c) this patch is from the roof edge (one-dimensional aperture problem); and (d) this patch is from the cloud (no good peak). Each grid point in figures b–d is one value of $\Delta \boldsymbol{u}$.

Using a Taylor Series expansion of the image function $I_0(\boldsymbol{x}_i+\Delta\boldsymbol{u}) \approx I_0(\boldsymbol{x}_i)+\nabla I_0(\boldsymbol{x}_i)\cdot\Delta\boldsymbol{u}$ (Lucas and Kanade 1981; Shi and Tomasi 1994), we can approximate the auto-correlation surface as

$$\begin{aligned} E_{\mathrm{AC}}(\Delta\boldsymbol{u}) &= \sum_i w(\boldsymbol{x}_i)[I_0(\boldsymbol{x}_i+\Delta\boldsymbol{u}) - I_0(\boldsymbol{x}_i)]^2 && (4.3)\\ &\approx \sum_i w(\boldsymbol{x}_i)[I_0(\boldsymbol{x}_i) + \nabla I_0(\boldsymbol{x}_i)\cdot\Delta\boldsymbol{u} - I_0(\boldsymbol{x}_i)]^2 && (4.4)\\ &= \sum_i w(\boldsymbol{x}_i)[\nabla I_0(\boldsymbol{x}_i)\cdot\Delta\boldsymbol{u}]^2 && (4.5)\\ &= \Delta\boldsymbol{u}^T\boldsymbol{A}\Delta\boldsymbol{u}, && (4.6) \end{aligned}$$

where

$$\nabla I_0(\boldsymbol{x}_i) = \left(\frac{\partial I_0}{\partial x}, \frac{\partial I_0}{\partial y}\right)(\boldsymbol{x}_i) \tag{4.7}$$

is the *image gradient* at $\boldsymbol{x}_i$. This gradient can be computed using a variety of techniques (Schmid, Mohr, and Bauckhage 2000). The classic "Harris" detector (Harris and Stephens 1988) uses a [-2 -1 0 1 2] filter, but more modern variants (Schmid, Mohr, and Bauckhage 2000; Triggs 2004) convolve the image with horizontal and vertical derivatives of a Gaussian (typically with $\sigma = 1$).

The auto-correlation matrix $\boldsymbol{A}$ can be written as

$$\boldsymbol{A} = w * \begin{bmatrix} I_x^2 & I_xI_y \\ I_xI_y & I_y^2 \end{bmatrix}, \tag{4.8}$$

where we have replaced the weighted summations with discrete convolutions with the weighting kernel w. This matrix can be interpreted as a tensor (multiband) image, where the outer products of the gradients ∇I are convolved with a weighting function w to provide a per-pixel estimate of the local (quadratic) shape of the auto-correlation function.

As first shown by Anandan (1984; 1989) and further discussed in Section 8.1.3 and (8.44), the inverse of the matrix $\boldsymbol{A}$ provides a lower bound on the uncertainty in the location of a matching patch. It is therefore a useful indicator of which patches can be reliably matched. The easiest way to visualize and reason about this uncertainty is to perform an eigenvalue analysis of the auto-correlation matrix $\boldsymbol{A}$, which produces two eigenvalues (λ_0, λ_1) and two eigenvector directions (Figure 4.6). Since the larger uncertainty depends on the smaller eigenvalue, i.e., $\lambda_0^{-1/2}$, it makes sense to find maxima in the smaller eigenvalue to locate good features to track (Shi and Tomasi 1994).

Förstner–Harris. While Anandan and Lucas and Kanade (1981) were the first to analyze the uncertainty structure of the auto-correlation matrix, they did so in the context of associating certainties with optic flow measurements. Förstner (1986) and Harris and Stephens

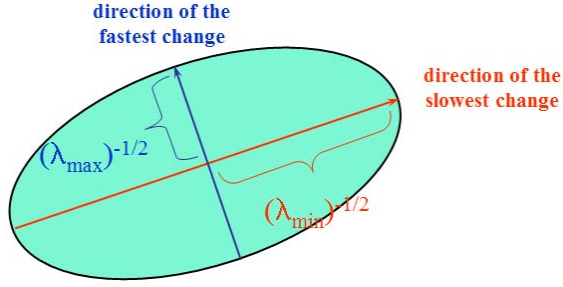

Figure 4.6 Uncertainty ellipse corresponding to an eigenvalue analysis of the auto-correlation matrix $\boldsymbol{A}$.

(1988) were the first to propose using local maxima in rotationally invariant scalar measures derived from the auto-correlation matrix to locate keypoints for the purpose of sparse feature matching. (Schmid, Mohr, and Bauckhage (2000); Triggs (2004) give more detailed historical reviews of feature detection algorithms.) Both of these techniques also proposed using a Gaussian weighting window instead of the previously used square patches, which makes the detector response insensitive to in-plane image rotations.

The minimum eigenvalue λ_0 (Shi and Tomasi 1994) is not the only quantity that can be used to find keypoints. A simpler quantity, proposed by Harris and Stephens (1988), is

$$\det(\boldsymbol{A}) - \alpha \operatorname{trace}(\boldsymbol{A})^2 = \lambda_0\lambda_1 - \alpha(\lambda_0 + \lambda_1)^2 \tag{4.9}$$

with $\alpha = 0.06$. Unlike eigenvalue analysis, this quantity does not require the use of square roots and yet is still rotationally invariant and also downweights edge-like features where $\lambda_1 \gg \lambda_0$. Triggs (2004) suggests using the quantity

$$\lambda_0 - \alpha\lambda_1 \tag{4.10}$$

(say, with $\alpha = 0.05$), which also reduces the response at 1D edges, where aliasing errors sometimes inflate the smaller eigenvalue. He also shows how the basic 2×2 Hessian can be extended to parametric motions to detect points that are also accurately localizable in scale and rotation. Brown, Szeliski, and Winder (2005), on the other hand, use the harmonic mean,

$$\frac{\det \boldsymbol{A}}{\operatorname{tr} \boldsymbol{A}} = \frac{\lambda_0\lambda_1}{\lambda_0 + \lambda_1}, \tag{4.11}$$

which is a smoother function in the region where $\lambda_0 \approx \lambda_1$. Figure 4.7 shows isocontours of the various interest point operators, from which we can see how the two eigenvalues are blended to determine the final interest value.

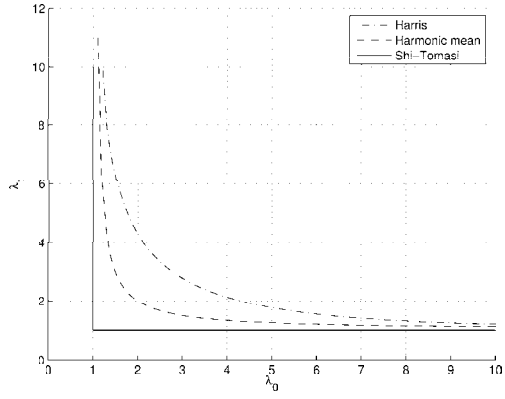

Figure 4.7 Isocontours of popular keypoint detection functions (Brown, Szeliski, and Winder 2004). Each detector looks for points where the eigenvalues λ_0, λ_1 of $\boldsymbol{A} = w * \nabla I \nabla I^T$ are both large.

1. Compute the horizontal and vertical derivatives of the image I_x and I_y by convolving the original image with derivatives of Gaussians (Section 3.2.3).
2. Compute the three images corresponding to the outer products of these gradients. (The matrix $\boldsymbol{A}$ is symmetric, so only three entries are needed.)
3. Convolve each of these images with a larger Gaussian.
4. Compute a scalar interest measure using one of the formulas discussed above.
5. Find local maxima above a certain threshold and report them as detected feature point locations.

Algorithm 4.1 Outline of a basic feature detection algorithm.

(a) (b) (c)

Figure 4.8 Interest operator responses: (a) Sample image, (b) Harris response, and (c) DoG response. The circle sizes and colors indicate the scale at which each interest point was detected. Notice how the two detectors tend to respond at complementary locations.

The steps in the basic auto-correlation-based keypoint detector are summarized in Algorithm 4.1. Figure 4.8 shows the resulting interest operator responses for the classic Harris detector as well as the difference of Gaussian (DoG) detector discussed below.

Adaptive non-maximal suppression (ANMS). While most feature detectors simply look for local maxima in the interest function, this can lead to an uneven distribution of feature points across the image, e.g., points will be denser in regions of higher contrast. To mitigate this problem, Brown, Szeliski, and Winder (2005) only detect features that are both local maxima and whose response value is significantly (10%) greater than that of all of its neighbors within a radius r (Figure 4.9c–d). They devise an efficient way to associate suppression radii with all local maxima by first sorting them by their response strength and then creating a second list sorted by decreasing suppression radius (Brown, Szeliski, and Winder 2005). Figure 4.9 shows a qualitative comparison of selecting the top n features and using ANMS.

Measuring repeatability. Given the large number of feature detectors that have been developed in computer vision, how can we decide which ones to use? Schmid, Mohr, and Bauckhage (2000) were the first to propose measuring the *repeatability* of feature detectors, which they define as the frequency with which keypoints detected in one image are found within ϵ (say, $\epsilon = 1.5$) pixels of the corresponding location in a transformed image. In their paper, they transform their planar images by applying rotations, scale changes, illumination changes, viewpoint changes, and adding noise. They also measure the *information content* available at each detected feature point, which they define as the entropy of a set of rotationally invariant local grayscale descriptors. Among the techniques they survey, they find that the improved (Gaussian derivative) version of the Harris operator with $\sigma_d = 1$ (scale of the derivative Gaussian) and $\sigma_i = 2$ (scale of the integration Gaussian) works best.

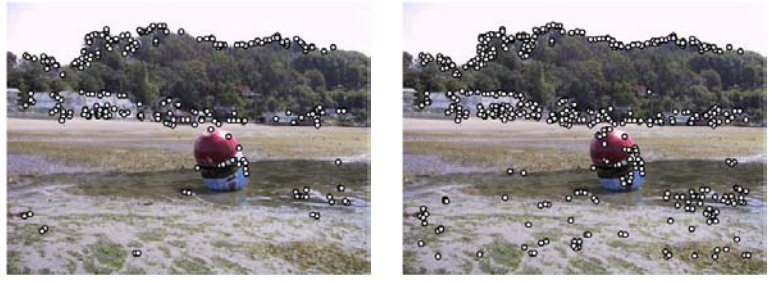

(a) Strongest 250 (b) Strongest 500

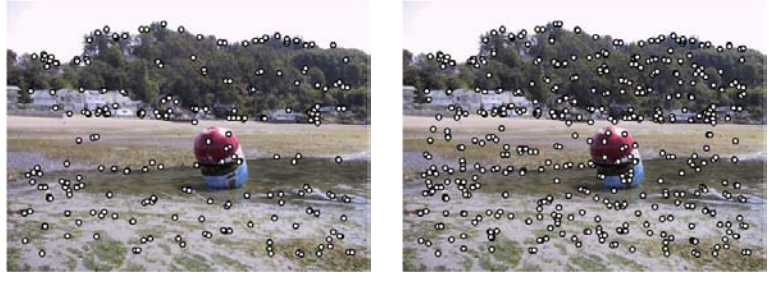

(c) ANMS 250, $r = 24$ (d) ANMS 500, $r = 16$

Figure 4.9 Adaptive non-maximal suppression (ANMS) (Brown, Szeliski, and Winder 2005) © 2005 IEEE: The upper two images show the strongest 250 and 500 interest points, while the lower two images show the interest points selected with adaptive non-maximal suppression, along with the corresponding suppression radius r. Note how the latter features have a much more uniform spatial distribution across the image.

Scale invariance

In many situations, detecting features at the finest stable scale possible may not be appropriate. For example, when matching images with little high frequency detail (e.g., clouds), fine-scale features may not exist.

One solution to the problem is to extract features at a variety of scales, e.g., by performing the same operations at multiple resolutions in a pyramid and then matching features at the same level. This kind of approach is suitable when the images being matched do not undergo large scale changes, e.g., when matching successive aerial images taken from an airplane or stitching panoramas taken with a fixed-focal-length camera. Figure 4.10 shows the output of one such approach, the multi-scale, oriented patch detector of Brown, Szeliski, and Winder (2005), for which responses at five different scales are shown.

However, for most object recognition applications, the scale of the object in the image

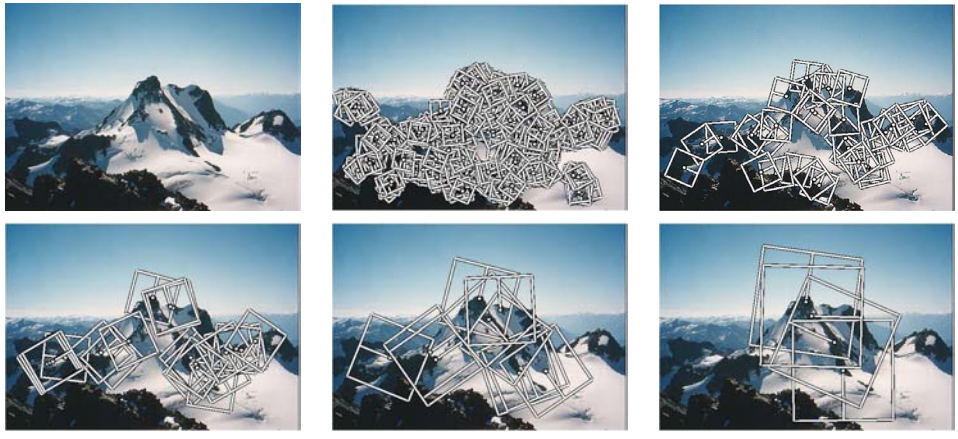

Figure 4.10 Multi-scale oriented patches (MOPS) extracted at five pyramid levels (Brown, Szeliski, and Winder 2005) © 2005 IEEE. The boxes show the feature orientation and the region from which the descriptor vectors are sampled.

is unknown. Instead of extracting features at many different scales and then matching all of them, it is more efficient to extract features that are stable in both location *and* scale (Lowe 2004; Mikolajczyk and Schmid 2004).

Early investigations into scale selection were performed by Lindeberg (1993; 1998b), who first proposed using extrema in the Laplacian of Gaussian (LoG) function as interest point locations. Based on this work, Lowe (2004) proposed computing a set of sub-octave Difference of Gaussian filters (Figure 4.11a), looking for 3D (space+scale) maxima in the resulting structure (Figure 4.11b), and then computing a sub-pixel space+scale location using a quadratic fit (Brown and Lowe 2002). The number of sub-octave levels was determined, after careful empirical investigation, to be three, which corresponds to a quarter-octave pyramid, which is the same as used by Triggs (2004).

As with the Harris operator, pixels where there is strong asymmetry in the local curvature of the indicator function (in this case, the DoG) are rejected. This is implemented by first computing the local Hessian of the difference image D,

$$\boldsymbol{H} = \begin{bmatrix} D_{xx} & D_{xy} \\ D_{xy} & D_{yy} \end{bmatrix}, \tag{4.12}$$

and then rejecting keypoints for which

$$\frac{\mathrm{Tr}(\boldsymbol{H})^2}{\mathrm{Det}(\boldsymbol{H})} > 10. \tag{4.13}$$

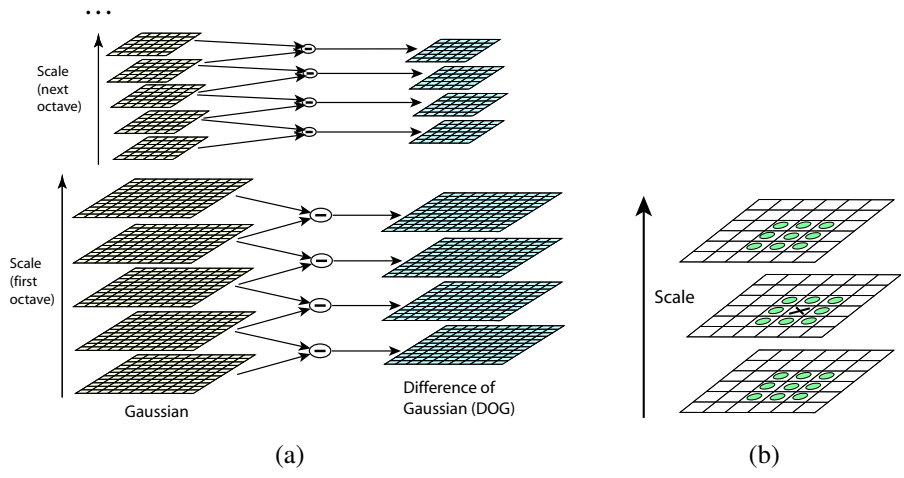

Figure 4.11 Scale-space feature detection using a sub-octave Difference of Gaussian pyramid (Lowe 2004) © 2004 Springer: (a) Adjacent levels of a sub-octave Gaussian pyramid are subtracted to produce Difference of Gaussian images; (b) extrema (maxima and minima) in the resulting 3D volume are detected by comparing a pixel to its 26 neighbors.

While Lowe's Scale Invariant Feature Transform (SIFT) performs well in practice, it is not based on the same theoretical foundation of maximum spatial stability as the auto-correlation-based detectors. (In fact, its detection locations are often complementary to those produced by such techniques and can therefore be used in conjunction with these other approaches.) In order to add a scale selection mechanism to the Harris corner detector, Mikolajczyk and Schmid (2004) evaluate the Laplacian of Gaussian function at each detected Harris point (in a multi-scale pyramid) and keep only those points for which the Laplacian is extremal (larger or smaller than both its coarser and finer-level values). An optional iterative refinement for both scale and position is also proposed and evaluated. Additional examples of scale invariant region detectors are discussed by Mikolajczyk, Tuytelaars, Schmid *et al.* (2005); Tuytelaars and Mikolajczyk (2007).

Rotational invariance and orientation estimation

In addition to dealing with scale changes, most image matching and object recognition algorithms need to deal with (at least) in-plane image rotation. One way to deal with this problem is to design descriptors that are rotationally invariant (Schmid and Mohr 1997), but such descriptors have poor discriminability, i.e. they map different looking patches to the same descriptor.

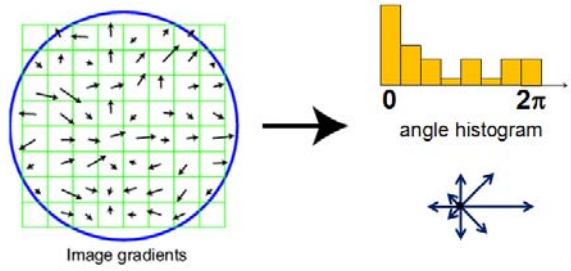

Figure 4.12 A dominant orientation estimate can be computed by creating a histogram of all the gradient orientations (weighted by their magnitudes or after thresholding out small gradients) and then finding the significant peaks in this distribution (Lowe 2004) © 2004 Springer.

A better method is to estimate a *dominant orientation* at each detected keypoint. Once the local orientation and scale of a keypoint have been estimated, a scaled and oriented patch around the detected point can be extracted and used to form a feature descriptor (Figures 4.10 and 4.17).

The simplest possible orientation estimate is the average gradient within a region around the keypoint. If a Gaussian weighting function is used (Brown, Szeliski, and Winder 2005), this average gradient is equivalent to a first-order steerable filter (Section 3.2.3), i.e., it can be computed using an image convolution with the horizontal and vertical derivatives of Gaussian filter (Freeman and Adelson 1991). In order to make this estimate more reliable, it is usually preferable to use a larger aggregation window (Gaussian kernel size) than detection window (Brown, Szeliski, and Winder 2005). The orientations of the square boxes shown in Figure 4.10 were computed using this technique.

Sometimes, however, the averaged (signed) gradient in a region can be small and therefore an unreliable indicator of orientation. A more reliable technique is to look at the *histogram* of orientations computed around the keypoint. Lowe (2004) computes a 36-bin histogram of edge orientations weighted by both gradient magnitude and Gaussian distance to the center, finds all peaks within 80% of the global maximum, and then computes a more accurate orientation estimate using a three-bin parabolic fit (Figure 4.12).

Affine invariance

While scale and rotation invariance are highly desirable, for many applications such as *wide baseline stereo matching* (Pritchett and Zisserman 1998; Schaffalitzky and Zisserman 2002) or location recognition (Chum, Philbin, Sivic *et al.* 2007), full affine invariance is preferred.

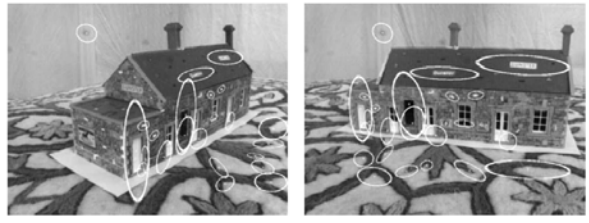

Figure 4.13 Affine region detectors used to match two images taken from dramatically different viewpoints (Mikolajczyk and Schmid 2004) © 2004 Springer.

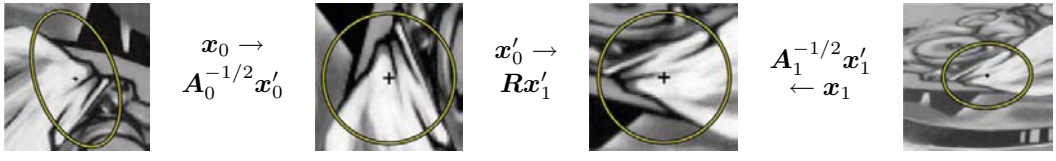

Figure 4.14 Affine normalization using the second moment matrices, as described by Mikolajczyk, Tuytelaars, Schmid *et al.* (2005) © 2005 Springer. After image coordinates are transformed using the matrices $\boldsymbol{A}_0^{-1/2}$ and $\boldsymbol{A}_1^{-1/2}$, they are related by a pure rotation $\boldsymbol{R}$, which can be estimated using a dominant orientation technique.

Affine-invariant detectors not only respond at consistent locations after scale and orientation changes, they also respond consistently across affine deformations such as (local) perspective foreshortening (Figure 4.13). In fact, for a small enough patch, any continuous image warping can be well approximated by an affine deformation.

To introduce affine invariance, several authors have proposed fitting an ellipse to the auto-correlation or Hessian matrix (using eigenvalue analysis) and then using the principal axes and ratios of this fit as the affine coordinate frame (Lindeberg and Garding 1997; Baumberg 2000; Mikolajczyk and Schmid 2004; Mikolajczyk, Tuytelaars, Schmid *et al.* 2005; Tuytelaars and Mikolajczyk 2007). Figure 4.14 shows how the square root of the moment matrix can be used to transform local patches into a frame which is similar up to rotation.

Another important affine invariant region detector is the maximally stable extremal region (MSER) detector developed by Matas, Chum, Urban *et al.* (2004). To detect MSERs, binary regions are computed by thresholding the image at all possible gray levels (the technique therefore only works for grayscale images). This operation can be performed efficiently by first sorting all pixels by gray value and then incrementally adding pixels to each connected component as the threshold is changed (Nistér and Stewénius 2008). As the threshold is changed, the area of each component (region) is monitored; regions whose rate of change of area with respect to the threshold is minimal are defined as *maximally stable*. Such regions

Figure 4.15 Maximally stable extremal regions (MSERs) extracted and matched from a number of images (Matas, Chum, Urban *et al.* 2004) © 2004 Elsevier.

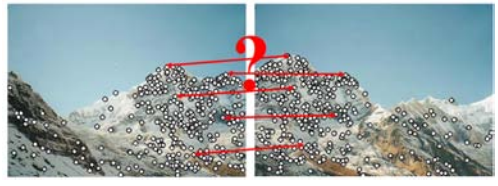

Figure 4.16 Feature matching: how can we extract local descriptors that are invariant to inter-image variations and yet still discriminative enough to establish correct correspondences?

are therefore invariant to both affine geometric and photometric (linear bias-gain or smooth monotonic) transformations (Figure 4.15). If desired, an affine coordinate frame can be fit to each detected region using its moment matrix.

The area of feature point detectors continues to be very active, with papers appearing every year at major computer vision conferences (Xiao and Shah 2003; Koethe 2003; Carneiro and Jepson 2005; Kenney, Zuliani, and Manjunath 2005; Bay, Tuytelaars, and Van Gool 2006; Platel, Balmachnova, Florack *et al.* 2006; Rosten and Drummond 2006). Mikolajczyk, Tuytelaars, Schmid *et al.* (2005) survey a number of popular affine region detectors and provide experimental comparisons of their invariance to common image transformations such as scaling, rotations, noise, and blur. These experimental results, code, and pointers to the surveyed papers can be found on their Web site at http://www.robots.ox.ac.uk/~vgg/research/affine/.

Of course, keypoints are not the only features that can be used for registering images. Zoghlami, Faugeras, and Deriche (1997) use line segments as well as point-like features to estimate homographies between pairs of images, whereas Bartoli, Coquerelle, and Sturm (2004) use line segments with local correspondences along the edges to extract 3D structure and motion. Tuytelaars and Van Gool (2004) use affine invariant regions to detect correspondences for wide baseline stereo matching, whereas Kadir, Zisserman, and Brady (2004) detect salient regions where patch entropy and its rate of change with scale are locally maximal. Corso and Hager (2005) use a related technique to fit 2D oriented Gaussian kernels to homogeneous regions. More details on techniques for finding and matching curves, lines, and regions can be found later in this chapter.

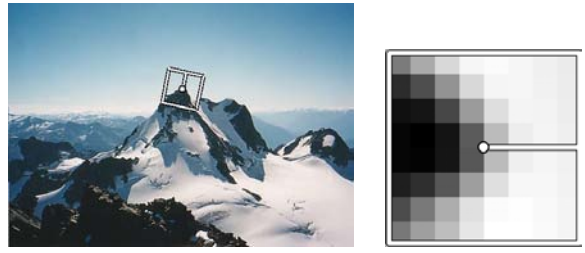

Figure 4.17 MOPS descriptors are formed using an 8×8 sampling of bias and gain normalized intensity values, with a sample spacing of five pixels relative to the detection scale (Brown, Szeliski, and Winder 2005) © 2005 IEEE. This low frequency sampling gives the features some robustness to interest point location error and is achieved by sampling at a higher pyramid level than the detection scale.

4.1.2 Feature descriptors

After detecting features (keypoints), we must *match* them, i.e., we must determine which features come from corresponding locations in different images. In some situations, e.g., for video sequences (Shi and Tomasi 1994) or for stereo pairs that have been *rectified* (Zhang, Deriche, Faugeras *et al.* 1995; Loop and Zhang 1999; Scharstein and Szeliski 2002), the local motion around each feature point may be mostly translational. In this case, simple error metrics, such as the *sum of squared differences* or *normalized cross-correlation*, described in Section 8.1 can be used to directly compare the intensities in small patches around each feature point. (The comparative study by Mikolajczyk and Schmid (2005), discussed below, uses cross-correlation.) Because feature points may not be exactly located, a more accurate matching score can be computed by performing incremental motion refinement as described in Section 8.1.3 but this can be time consuming and can sometimes even decrease performance (Brown, Szeliski, and Winder 2005).

In most cases, however, the local appearance of features will change in orientation and scale, and sometimes even undergo affine deformations. Extracting a local scale, orientation, or affine frame estimate and then using this to resample the patch before forming the feature descriptor is thus usually preferable (Figure 4.17).

Even after compensating for these changes, the local appearance of image patches will usually still vary from image to image. How can we make image descriptors more invariant to such changes, while still preserving discriminability between different (non-corresponding) patches (Figure 4.16)? Mikolajczyk and Schmid (2005) review some recently developed view-invariant local image descriptors and experimentally compare their performance. Below, we describe a few of these descriptors in more detail.

Bias and gain normalization (MOPS). For tasks that do not exhibit large amounts of foreshortening, such as image stitching, simple normalized intensity patches perform reasonably well and are simple to implement (Brown, Szeliski, and Winder 2005) (Figure 4.17). In order to compensate for slight inaccuracies in the feature point detector (location, orientation, and scale), these multi-scale oriented patches (MOPS) are sampled at a spacing of five pixels relative to the detection scale, using a coarser level of the image pyramid to avoid aliasing. To compensate for affine photometric variations (linear exposure changes or bias and gain, (3.3)), patch intensities are re-scaled so that their mean is zero and their variance is one.

Scale invariant feature transform (SIFT). SIFT features are formed by computing the gradient at each pixel in a 16×16 window around the detected keypoint, using the appropriate level of the Gaussian pyramid at which the keypoint was detected. The gradient magnitudes are downweighted by a Gaussian fall-off function (shown as a blue circle in (Figure 4.18a) in order to reduce the influence of gradients far from the center, as these are more affected by small misregistrations.

In each 4×4 quadrant, a gradient orientation histogram is formed by (conceptually) adding the weighted gradient value to one of eight orientation histogram bins. To reduce the effects of location and dominant orientation misestimation, each of the original 256 weighted gradient magnitudes is softly added to $2 \times 2 \times 2$ histogram bins using trilinear interpolation. Softly distributing values to adjacent histogram bins is generally a good idea in any application where histograms are being computed, e.g., for Hough transforms (Section 4.3.2) or local histogram equalization (Section 3.1.4).

The resulting 128 non-negative values form a raw version of the SIFT descriptor vector. To reduce the effects of contrast or gain (additive variations are already removed by the gradient), the 128-D vector is normalized to unit length. To further make the descriptor robust to other photometric variations, values are clipped to 0.2 and the resulting vector is once again renormalized to unit length.

PCA-SIFT. Ke and Sukthankar (2004) propose a simpler way to compute descriptors inspired by SIFT; it computes the x and y (gradient) derivatives over a 39×39 patch and then reduces the resulting 3042-dimensional vector to 36 using principal component analysis (PCA) (Section 14.2.1 and Appendix A.1.2). Another popular variant of SIFT is SURF (Bay, Tuytelaars, and Van Gool 2006), which uses box filters to approximate the derivatives and integrals used in SIFT.

Gradient location-orientation histogram (GLOH). This descriptor, developed by Mikolajczyk and Schmid (2005), is a variant on SIFT that uses a log-polar binning structure instead of the four quadrants used by Lowe (2004) (Figure 4.19). The spatial bins are of radius 6,

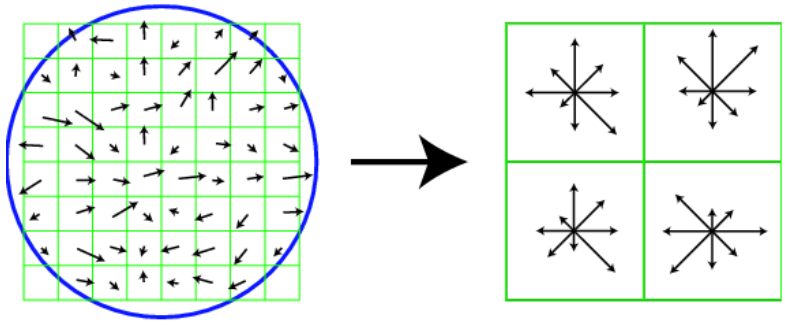

(a) image gradients (b) keypoint descriptor

Figure 4.18 A schematic representation of Lowe's (2004) scale invariant feature transform (SIFT): (a) Gradient orientations and magnitudes are computed at each pixel and weighted by a Gaussian fall-off function (blue circle). (b) A weighted gradient orientation histogram is then computed in each subregion, using trilinear interpolation. While this figure shows an 8×8 pixel patch and a 2×2 descriptor array, Lowe's actual implementation uses 16×16 patches and a 4×4 array of eight-bin histograms.

11, and 15, with eight angular bins (except for the central region), for a total of 17 spatial bins and 16 orientation bins. The 272-dimensional histogram is then projected onto a 128-dimensional descriptor using PCA trained on a large database. In their evaluation, Mikolajczyk and Schmid (2005) found that GLOH, which has the best performance overall, outperforms SIFT by a small margin.

Steerable filters. Steerable filters (Section 3.2.3) are combinations of derivative of Gaussian filters that permit the rapid computation of even and odd (symmetric and anti-symmetric) edge-like and corner-like features at all possible orientations (Freeman and Adelson 1991). Because they use reasonably broad Gaussians, they too are somewhat insensitive to localization and orientation errors.

Performance of local descriptors. Among the local descriptors that Mikolajczyk and Schmid (2005) compared, they found that GLOH performed best, followed closely by SIFT (see Figure 4.25). They also present results for many other descriptors not covered in this book.

The field of feature descriptors continues to evolve rapidly, with some of the newer techniques looking at local color information (van de Weijer and Schmid 2006; Abdel-Hakim and Farag 2006). Winder and Brown (2007) develop a multi-stage framework for feature descriptor computation that subsumes both SIFT and GLOH (Figure 4.20a) and also allows them to learn optimal parameters for newer descriptors that outperform previous hand-tuned

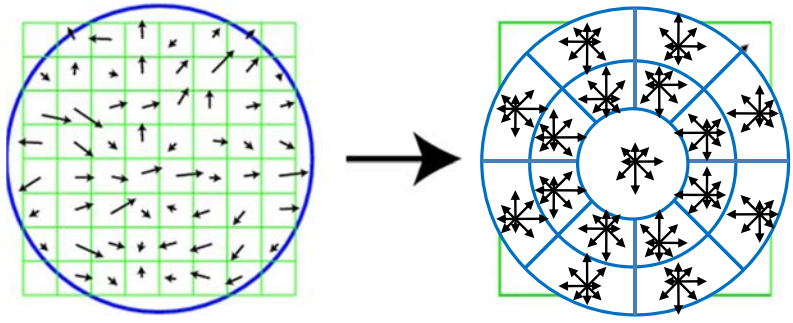

(a) image gradients (b) keypoint descriptor

Figure 4.19 The gradient location-orientation histogram (GLOH) descriptor uses log-polar bins instead of square bins to compute orientation histograms (Mikolajczyk and Schmid 2005).

descriptors. Hua, Brown, and Winder (2007) extend this work by learning lower-dimensional projections of higher-dimensional descriptors that have the best discriminative power. Both of these papers use a database of real-world image patches (Figure 4.20b) obtained by sampling images at locations that were reliably matched using a robust structure-from-motion algorithm applied to Internet photo collections (Snavely, Seitz, and Szeliski 2006; Goesele, Snavely, Curless *et al.* 2007). In concurrent work, Tola, Lepetit, and Fua (2010) developed a similar DAISY descriptor for dense stereo matching and optimized its parameters based on ground truth stereo data.

While these techniques construct feature detectors that optimize for repeatability across *all* object classes, it is also possible to develop class- or instance-specific feature detectors that maximize *discriminability* from other classes (Ferencz, Learned-Miller, and Malik 2008).

4.1.3 Feature matching

Once we have extracted features and their descriptors from two or more images, the next step is to establish some preliminary feature matches between these images. In this section, we divide this problem into two separate components. The first is to select a *matching strategy*, which determines which correspondences are passed on to the next stage for further processing. The second is to devise efficient *data structures* and *algorithms* to perform this matching as quickly as possible. (See the discussion of related techniques in Section 14.3.2.)

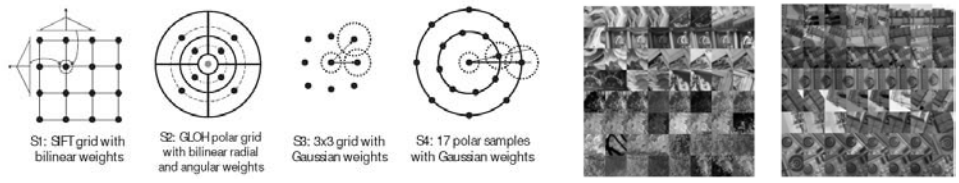

Figure 4.20 Spatial summation blocks for SIFT, GLOH, and some newly developed feature descriptors (Winder and Brown 2007) © 2007 IEEE: (a) The parameters for the new features, e.g., their Gaussian weights, are learned from a training database of (b) matched real-world image patches obtained from robust structure from motion applied to Internet photo collections (Hua, Brown, and Winder 2007).

Matching strategy and error rates

Determining which feature matches are reasonable to process further depends on the context in which the matching is being performed. Say we are given two images that overlap to a fair amount (e.g., for image stitching, as in Figure 4.16, or for tracking objects in a video). We know that most features in one image are likely to match the other image, although some may not match because they are occluded or their appearance has changed too much.

On the other hand, if we are trying to recognize how many known objects appear in a cluttered scene (Figure 4.21), most of the features may not match. Furthermore, a large number of potentially matching objects must be searched, which requires more efficient strategies, as described below.

To begin with, we assume that the feature descriptors have been designed so that Euclidean (vector magnitude) distances in feature space can be directly used for ranking potential matches. If it turns out that certain parameters (axes) in a descriptor are more reliable than others, it is usually preferable to re-scale these axes ahead of time, e.g., by determining how much they vary when compared against other known good matches (Hua, Brown, and Winder 2007). A more general process, which involves transforming feature vectors into a new scaled basis, is called *whitening* and is discussed in more detail in the context of eigenface-based face recognition (Section 14.2.1).

Given a Euclidean distance metric, the simplest matching strategy is to set a threshold (maximum distance) and to return all matches from other images within this threshold. Setting the threshold too high results in too many *false positives*, i.e., incorrect matches being returned. Setting the threshold too low results in too many *false negatives*, i.e., too many correct matches being missed (Figure 4.22).

We can quantify the performance of a matching algorithm at a particular threshold by

Figure 4.21 Recognizing objects in a cluttered scene (Lowe 2004) © 2004 Springer. Two of the training images in the database are shown on the left. These are matched to the cluttered scene in the middle using SIFT features, shown as small squares in the right image. The affine warp of each recognized database image onto the scene is shown as a larger parallelogram in the right image.

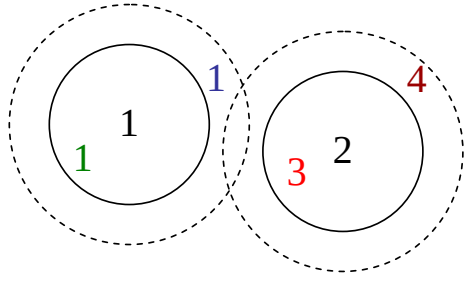

Figure 4.22 False positives and negatives: The black digits 1 and 2 are features being matched against a database of features in other images. At the current threshold setting (the solid circles), the green 1 is a *true positive* (good match), the blue 1 is a *false negative* (failure to match), and the red 3 is a *false positive* (incorrect match). If we set the threshold higher (the dashed circles), the blue 1 becomes a true positive but the brown 4 becomes an additional false positive.

	True matches	True non-matches		
Predicted matches	TP = 18	FP = 4	P' = 22	PPV = 0.82
Predicted non-matches	FN = 2	TN = 76	N' = 78	
	P = 20	N = 80	Total = 100	
	TPR = 0.90	FPR = 0.05		ACC = 0.94

Table 4.1 The number of matches correctly and incorrectly estimated by a feature matching algorithm, showing the number of true positives (TP), false positives (FP), false negatives (FN) and true negatives (TN). The columns sum up to the actual number of positives (P) and negatives (N), while the rows sum up to the predicted number of positives (P') and negatives (N'). The formulas for the true positive rate (TPR), the false positive rate (FPR), the positive predictive value (PPV), and the accuracy (ACC) are given in the text.

first counting the number of true and false matches and match failures, using the following definitions (Fawcett 2006):

- TP: true positives, i.e., number of correct matches;
- FN: false negatives, matches that were not correctly detected;
- FP: false positives, proposed matches that are incorrect;
- TN: true negatives, non-matches that were correctly rejected.

Table 4.1 shows a sample *confusion matrix* (contingency table) containing such numbers.

We can convert these numbers into *unit rates* by defining the following quantities (Fawcett 2006):

- true positive rate (TPR),
$$\text{TPR} = \frac{\text{TP}}{\text{TP+FN}} = \frac{\text{TP}}{\text{P}}; \tag{4.14}$$
- false positive rate (FPR),
$$\text{FPR} = \frac{\text{FP}}{\text{FP+TN}} = \frac{\text{FP}}{\text{N}}; \tag{4.15}$$
- positive predictive value (PPV),
$$\text{PPV} = \frac{\text{TP}}{\text{TP+FP}} = \frac{\text{TP}}{\text{P'}}; \tag{4.16}$$
- accuracy (ACC),
$$\text{ACC} = \frac{\text{TP+TN}}{\text{P+N}}. \tag{4.17}$$

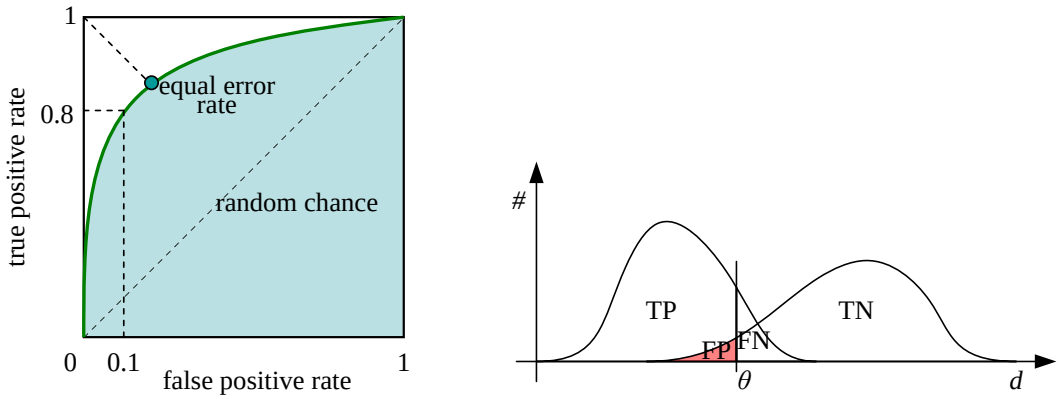

Figure 4.23 ROC curve and its related rates: (a) The ROC curve plots the true positive rate against the false positive rate for a particular combination of feature extraction and matching algorithms. Ideally, the true positive rate should be close to 1, while the false positive rate is close to 0. The area under the ROC curve (AUC) is often used as a single (scalar) measure of algorithm performance. Alternatively, the equal error rate is sometimes used. (b) The distribution of positives (matches) and negatives (non-matches) as a function of inter-feature distance d. As the threshold θ is increased, the number of true positives (TP) and false positives (FP) increases.

In the *information retrieval* (or document retrieval) literature (Baeza-Yates and Ribeiro-Neto 1999; Manning, Raghavan, and Schütze 2008), the term *precision* (how many returned documents are relevant) is used instead of PPV and *recall* (what fraction of relevant documents was found) is used instead of TPR.

Any particular matching strategy (at a particular threshold or parameter setting) can be rated by the TPR and FPR numbers; ideally, the true positive rate will be close to 1 and the false positive rate close to 0. As we vary the matching threshold, we obtain a family of such points, which are collectively known as the *receiver operating characteristic (ROC curve)* (Fawcett 2006) (Figure 4.23a). The closer this curve lies to the upper left corner, i.e., the larger the area under the curve (AUC), the better its performance. Figure 4.23b shows how we can plot the number of matches and non-matches as a function of inter-feature distance d. These curves can then be used to plot an ROC curve (Exercise 4.3). The ROC curve can also be used to calculate the *mean average precision*, which is the average precision (PPV) as you vary the threshold to select the best results, then the two top results, etc.

The problem with using a fixed threshold is that it is difficult to set; the useful range

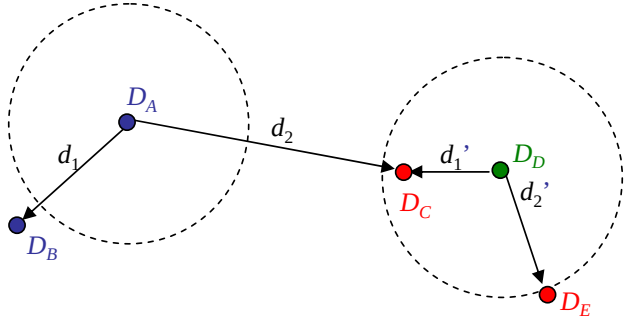

Figure 4.24 Fixed threshold, nearest neighbor, and nearest neighbor distance ratio matching. At a fixed distance threshold (dashed circles), descriptor D_A fails to match D_B and D_D incorrectly matches D_C and D_E. If we pick the nearest neighbor, D_A correctly matches D_B but D_D incorrectly matches D_C. Using nearest neighbor distance ratio (NNDR) matching, the small NNDR d_1/d_2 correctly matches D_A with D_B, and the large NNDR d_1'/d_2' correctly rejects matches for D_D.

of thresholds can vary a lot as we move to different parts of the feature space (Lowe 2004; Mikolajczyk and Schmid 2005). A better strategy in such cases is to simply match the *nearest neighbor* in feature space. Since some features may have no matches (e.g., they may be part of background clutter in object recognition or they may be occluded in the other image), a threshold is still used to reduce the number of false positives.

Ideally, this threshold itself will adapt to different regions of the feature space. If sufficient training data is available (Hua, Brown, and Winder 2007), it is sometimes possible to learn different thresholds for different features. Often, however, we are simply given a collection of images to match, e.g., when stitching images or constructing 3D models from unordered photo collections (Brown and Lowe 2007, 2003; Snavely, Seitz, and Szeliski 2006). In this case, a useful heuristic can be to compare the nearest neighbor distance to that of the second nearest neighbor, preferably taken from an image that is known not to match the target (e.g., a different object in the database) (Brown and Lowe 2002; Lowe 2004). We can define this *nearest neighbor distance ratio* (Mikolajczyk and Schmid 2005) as

$$\text{NNDR} = \frac{d_1}{d_2} = \frac{\|D_A - D_B\|}{\|D_A - D_C\|}, \tag{4.18}$$

where d_1 and d_2 are the nearest and second nearest neighbor distances, D_A is the target descriptor, and D_B and D_C are its closest two neighbors (Figure 4.24).

The effects of using these three different matching strategies for the feature descriptors evaluated by Mikolajczyk and Schmid (2005) are shown in Figure 4.25. As you can see, the nearest neighbor and NNDR strategies produce improved ROC curves.

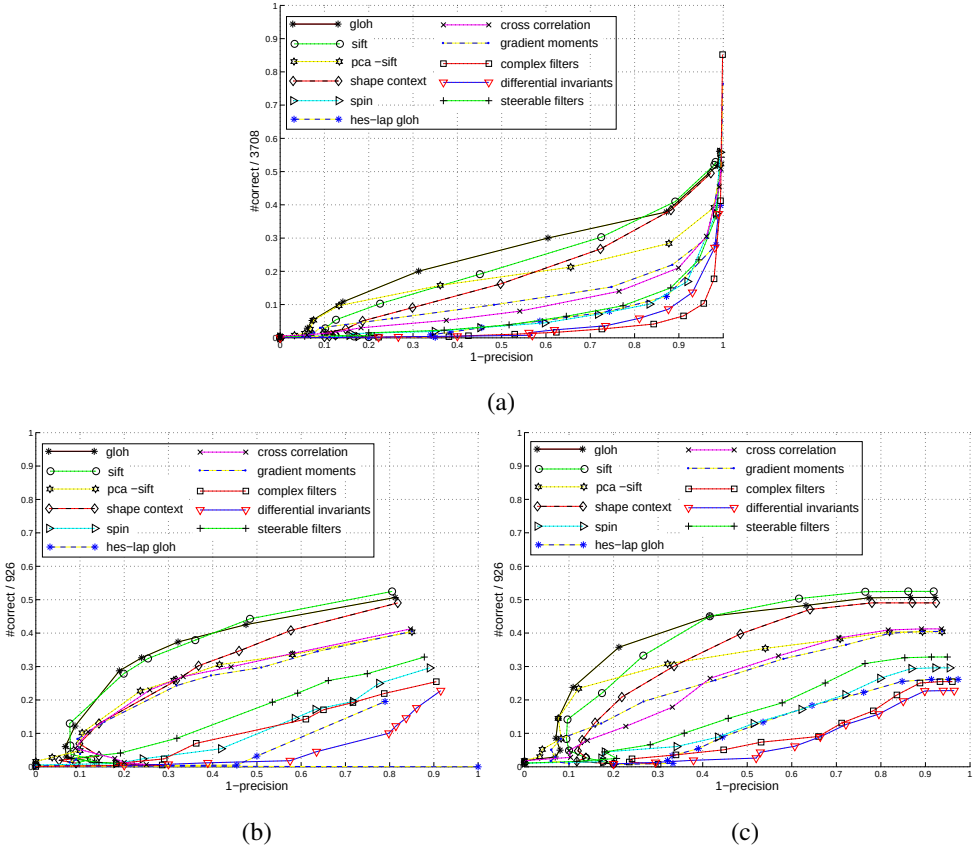

Figure 4.25 Performance of the feature descriptors evaluated by Mikolajczyk and Schmid (2005) © 2005 IEEE, shown for three matching strategies: (a) fixed threshold; (b) nearest neighbor; (c) nearest neighbor distance ratio (NNDR). Note how the ordering of the algorithms does not change that much, but the overall performance varies significantly between the different matching strategies.

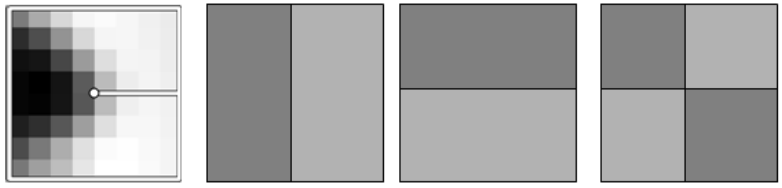

Figure 4.26 The three Haar wavelet coefficients used for hashing the MOPS descriptor devised by Brown, Szeliski, and Winder (2005) are computed by summing each 8×8 normalized patch over the light and dark gray regions and taking their difference.

Efficient matching

Once we have decided on a matching strategy, we still need to search efficiently for potential candidates. The simplest way to find all corresponding feature points is to compare all features against all other features in each pair of potentially matching images. Unfortunately, this is quadratic in the number of extracted features, which makes it impractical for most applications.

A better approach is to devise an *indexing structure*, such as a multi-dimensional search tree or a hash table, to rapidly search for features near a given feature. Such indexing structures can either be built for each image independently (which is useful if we want to only consider certain potential matches, e.g., searching for a particular object) or globally for all the images in a given database, which can potentially be faster, since it removes the need to iterate over each image. For extremely large databases (millions of images or more), even more efficient structures based on ideas from document retrieval (e.g., *vocabulary trees*, (Nistér and Stewénius 2006)) can be used (Section 14.3.2).

One of the simpler techniques to implement is multi-dimensional hashing, which maps descriptors into fixed size buckets based on some function applied to each descriptor vector. At matching time, each new feature is hashed into a bucket, and a search of nearby buckets is used to return potential candidates, which can then be sorted or graded to determine which are valid matches.

A simple example of hashing is the Haar wavelets used by Brown, Szeliski, and Winder (2005) in their MOPS paper. During the matching structure construction, each 8×8 scaled, oriented, and normalized MOPS patch is converted into a three-element index by performing sums over different quadrants of the patch (Figure 4.26). The resulting three values are normalized by their expected standard deviations and then mapped to the two (of $b = 10$) nearest 1D bins. The three-dimensional indices formed by concatenating the three quantized values are used to index the $2^3 = 8$ bins where the feature is stored (added). At query time, only the primary (closest) indices are used, so only a single three-dimensional bin needs to

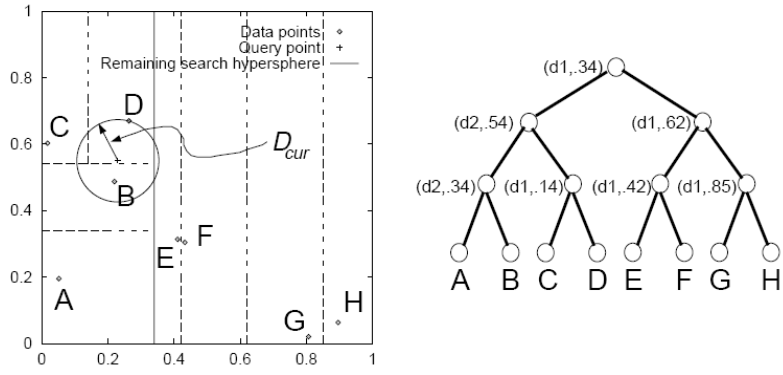

(a) (b)

Figure 4.27 K-d tree and best bin first (BBF) search (Beis and Lowe 1999) © 1999 IEEE: (a) The spatial arrangement of the axis-aligned cutting planes is shown using dashed lines. Individual data points are shown as small diamonds. (b) The same subdivision can be represented as a tree, where each interior node represents an axis-aligned cutting plane (e.g., the top node cuts along dimension d1 at value .34) and each leaf node is a data point. During a BBF search, a query point (denoted by "+") first looks in its containing bin (D) and then in its nearest adjacent bin (B), rather than its closest neighbor in the tree (C).

be examined. The coefficients in the bin can then be used to select k approximate nearest neighbors for further processing (such as computing the NNDR).

A more complex, but more widely applicable, version of hashing is called *locality sensitive hashing*, which uses unions of independently computed hashing functions to index the features (Gionis, Indyk, and Motwani 1999; Shakhnarovich, Darrell, and Indyk 2006). Shakhnarovich, Viola, and Darrell (2003) extend this technique to be more sensitive to the distribution of points in parameter space, which they call *parameter-sensitive hashing*. Even more recent work converts high-dimensional descriptor vectors into binary codes that can be compared using Hamming distances (Torralba, Weiss, and Fergus 2008; Weiss, Torralba, and Fergus 2008) or that can accommodate arbitrary kernel functions (Kulis and Grauman 2009; Raginsky and Lazebnik 2009).

Another widely used class of indexing structures are multi-dimensional search trees. The best known of these are *k-d trees*, also often written as kd-trees, which divide the multi-dimensional feature space along alternating axis-aligned hyperplanes, choosing the threshold along each axis so as to maximize some criterion, such as the search tree balance (Samet 1989). Figure 4.27 shows an example of a two-dimensional k-d tree. Here, eight different data points A–H are shown as small diamonds arranged on a two-dimensional plane. The k-d tree

recursively splits this plane along axis-aligned (horizontal or vertical) cutting planes. Each split can be denoted using the dimension number and split value (Figure 4.27b). The splits are arranged so as to try to balance the tree, i.e., to keep its maximum depth as small as possible. At query time, a classic k-d tree search first locates the query point (+) in its appropriate bin (D), and then searches nearby leaves in the tree (C, B, ...) until it can guarantee that the nearest neighbor has been found. The best bin first (BBF) search (Beis and Lowe 1999) searches bins in order of their spatial proximity to the query point and is therefore usually more efficient.

Many additional data structures have been developed over the years for solving nearest neighbor problems (Arya, Mount, Netanyahu *et al.* 1998; Liang, Liu, Xu *et al.* 2001; Hjaltason and Samet 2003). For example, Nene and Nayar (1997) developed a technique they call *slicing* that uses a series of 1D binary searches on the point list sorted along different dimensions to efficiently cull down a list of candidate points that lie within a hypercube of the query point. Grauman and Darrell (2005) reweight the matches at different levels of an indexing tree, which allows their technique to be less sensitive to discretization errors in the tree construction. Nistér and Stewénius (2006) use a *metric tree*, which compares feature descriptors to a small number of prototypes at each level in a hierarchy. The resulting quantized *visual words* can then be used with classical information retrieval (document relevance) techniques to quickly winnow down a set of potential candidates from a database of millions of images (Section 14.3.2). Muja and Lowe (2009) compare a number of these approaches, introduce a new one of their own (priority search on hierarchical k-means trees), and conclude that multiple randomized k-d trees often provide the best performance. Despite all of this promising work, the rapid computation of image feature correspondences remains a challenging open research problem.

Feature match verification and densification

Once we have some hypothetical (putative) matches, we can often use geometric alignment (Section 6.1) to verify which matches are *inliers* and which ones are *outliers*. For example, if we expect the whole image to be translated or rotated in the matching view, we can fit a global geometric transform and keep only those feature matches that are sufficiently close to this estimated transformation. The process of selecting a small set of seed matches and then verifying a larger set is often called *random sampling* or RANSAC (Section 6.1.4). Once an initial set of correspondences has been established, some systems look for additional matches, e.g., by looking for additional correspondences along epipolar lines (Section 11.1) or in the vicinity of estimated locations based on the global transform. These topics are discussed further in Sections 6.1, 11.2, and 14.3.1.

4.1.4 Feature tracking

An alternative to independently finding features in all candidate images and then matching them is to find a set of likely feature locations in a first image and to then *search* for their corresponding locations in subsequent images. This kind of *detect then track* approach is more widely used for video tracking applications, where the expected amount of motion and appearance deformation between adjacent frames is expected to be small.

The process of selecting good features to track is closely related to selecting good features for more general recognition applications. In practice, regions containing high gradients in both directions, i.e., which have high eigenvalues in the auto-correlation matrix (4.8), provide stable locations at which to find correspondences (Shi and Tomasi 1994).

In subsequent frames, searching for locations where the corresponding patch has low squared difference (4.1) often works well enough. However, if the images are undergoing brightness change, explicitly compensating for such variations (8.9) or using *normalized cross-correlation* (8.11) may be preferable. If the search range is large, it is also often more efficient to use a *hierarchical* search strategy, which uses matches in lower-resolution images to provide better initial guesses and hence speed up the search (Section 8.1.1). Alternatives to this strategy involve learning what the appearance of the patch being tracked should be and then searching for it in the vicinity of its predicted position (Avidan 2001; Jurie and Dhome 2002; Williams, Blake, and Cipolla 2003). These topics are all covered in more detail in Section 8.1.3.

If features are being tracked over longer image sequences, their appearance can undergo larger changes. You then have to decide whether to continue matching against the originally detected patch (feature) or to re-sample each subsequent frame at the matching location. The former strategy is prone to failure as the original patch can undergo appearance changes such as foreshortening. The latter runs the risk of the feature drifting from its original location to some other location in the image (Shi and Tomasi 1994). (Mathematically, small misregistration errors compound to create a *Markov Random Walk*, which leads to larger drift over time.)

A preferable solution is to compare the original patch to later image locations using an *affine* motion model (Section 8.2). Shi and Tomasi (1994) first compare patches in neighboring frames using a translational model and then use the location estimates produced by this step to initialize an affine registration between the patch in the current frame and the base frame where a feature was first detected (Figure 4.28). In their system, features are only detected infrequently, i.e., only in regions where tracking has failed. In the usual case, an area around the current *predicted* location of the feature is searched with an incremental registration algorithm (Section 8.1.3). The resulting tracker is often called the Kanade–Lucas–Tomasi (KLT) tracker.

Figure 4.28 Feature tracking using an affine motion model (Shi and Tomasi 1994) © 1994 IEEE, Top row: image patch around the tracked feature location. Bottom row: image patch after warping back toward the first frame using an affine deformation. Even though the speed sign gets larger from frame to frame, the affine transformation maintains a good resemblance between the original and subsequent tracked frames.

Since their original work on feature tracking, Shi and Tomasi's approach has generated a string of interesting follow-on papers and applications. Beardsley, Torr, and Zisserman (1996) use extended feature tracking combined with structure from motion (Chapter 7) to incrementally build up sparse 3D models from video sequences. Kang, Szeliski, and Shum (1997) tie together the corners of adjacent (regularly gridded) patches to provide some additional stability to the tracking, at the cost of poorer handling of occlusions. Tommasini, Fusiello, Trucco *et al.* (1998) provide a better spurious match rejection criterion for the basic Shi and Tomasi algorithm, Collins and Liu (2003) provide improved mechanisms for feature selection and dealing with larger appearance changes over time, and Shafique and Shah (2005) develop algorithms for feature matching (data association) for videos with large numbers of moving objects or points. Yilmaz, Javed, and Shah (2006) and Lepetit and Fua (2005) survey the larger field of object tracking, which includes not only feature-based techniques but also alternative techniques based on contour and region (Section 5.1).

One of the newest developments in feature tracking is the use of learning algorithms to build special-purpose recognizers to rapidly search for matching features anywhere in an image (Lepetit, Pilet, and Fua 2006; Hinterstoisser, Benhimane, Navab *et al.* 2008; Rogez, Rihan, Ramalingam *et al.* 2008; Özuysal, Calonder, Lepetit *et al.* 2010).[2] By taking the time to train classifiers on sample patches and their affine deformations, extremely fast and reliable feature detectors can be constructed, which enables much faster motions to be supported (Figure 4.29). Coupling such features to deformable models (Pilet, Lepetit, and Fua 2008) or structure-from-motion algorithms (Klein and Murray 2008) can result in even higher stability.

[2] See also my previous comment on earlier work in learning-based tracking (Avidan 2001; Jurie and Dhome 2002; Williams, Blake, and Cipolla 2003).

Figure 4.29 Real-time head tracking using the fast trained classifiers of Lepetit, Pilet, and Fua (2004) © 2004 IEEE.

4.1.5 *Application*: Performance-driven animation

One of the most compelling applications of fast feature tracking is *performance-driven animation*, i.e., the interactive deformation of a 3D graphics model based on tracking a user's motions (Williams 1990; Litwinowicz and Williams 1994; Lepetit, Pilet, and Fua 2004).

Buck, Finkelstein, Jacobs *et al.* (2000) present a system that tracks a user's facial expressions and head motions and then uses them to morph among a series of hand-drawn sketches. An animator first extracts the eye and mouth regions of each sketch and draws control lines over each image (Figure 4.30a). At run time, a face-tracking system (Toyama 1998) determines the current location of these features (Figure 4.30b). The animation system decides which input images to morph based on nearest neighbor feature appearance matching and triangular barycentric interpolation. It also computes the global location and orientation of the head from the tracked features. The resulting morphed eye and mouth regions are then composited back into the overall head model to yield a frame of hand-drawn animation (Figure 4.30d).

In more recent work, Barnes, Jacobs, Sanders *et al.* (2008) watch users animate paper cutouts on a desk and then turn the resulting motions and drawings into seamless 2D animations.

(a) (b) (c) (d)

Figure 4.30 Performance-driven, hand-drawn animation (Buck, Finkelstein, Jacobs *et al.* 2000) © 2000 ACM: (a) eye and mouth portions of hand-drawn sketch with their overlaid control lines; (b) an input video frame with the tracked features overlaid; (c) a different input video frame along with its (d) corresponding hand-drawn animation.

4.2 Edges

While interest points are useful for finding image locations that can be accurately matched in 2D, edge points are far more plentiful and often carry important semantic associations. For example, the boundaries of objects, which also correspond to occlusion events in 3D, are usually delineated by visible contours. Other kinds of edges correspond to shadow boundaries or crease edges, where surface orientation changes rapidly. Isolated edge points can also be grouped into longer *curves* or *contours*, as well as *straight line segments* (Section 4.3). It is interesting that even young children have no difficulty in recognizing familiar objects or animals from such simple line drawings.

4.2.1 Edge detection

Given an image, how can we find the salient edges? Consider the color images in Figure 4.31. If someone asked you to point out the most "salient" or "strongest" edges or the object boundaries (Martin, Fowlkes, and Malik 2004; Arbeláez, Maire, Fowlkes *et al.* 2010), which ones would you trace? How closely do your perceptions match the edge images shown in Figure 4.31?

Qualitatively, edges occur at boundaries between regions of different color, intensity, or texture. Unfortunately, segmenting an image into coherent regions is a difficult task, which we address in Chapter 5. Often, it is preferable to detect edges using only purely local information.

Under such conditions, a reasonable approach is to define an edge as a location of *rapid*

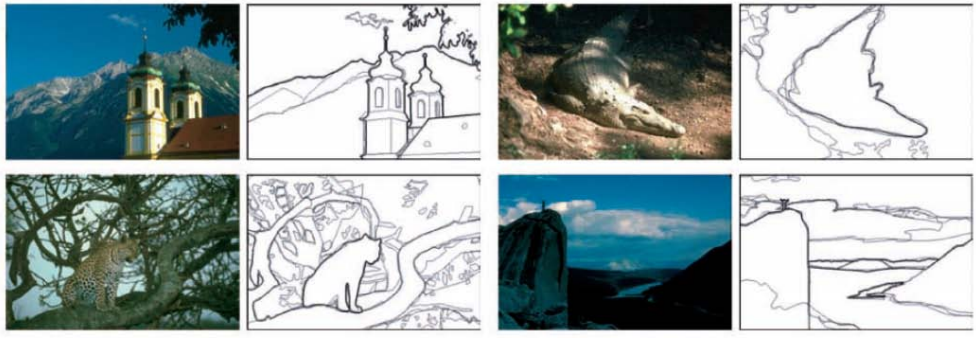

Figure 4.31 Human boundary detection (Martin, Fowlkes, and Malik 2004) © 2004 IEEE. The darkness of the edges corresponds to how many human subjects marked an object boundary at that location.

intensity variation.[3] Think of an image as a height field. On such a surface, edges occur at locations of *steep slopes*, or equivalently, in regions of closely packed contour lines (on a topographic map).

A mathematical way to define the slope and direction of a surface is through its gradient,

$$\boldsymbol{J}(\boldsymbol{x}) = \nabla I(\boldsymbol{x}) = (\frac{\partial I}{\partial x}, \frac{\partial I}{\partial y})(\boldsymbol{x}). \tag{4.19}$$

The local gradient vector $\boldsymbol{J}$ points in the direction of *steepest ascent* in the intensity function. Its magnitude is an indication of the slope or strength of the variation, while its orientation points in a direction *perpendicular* to the local contour.

Unfortunately, taking image derivatives accentuates high frequencies and hence amplifies noise, since the proportion of noise to signal is larger at high frequencies. It is therefore prudent to smooth the image with a low-pass filter prior to computing the gradient. Because we would like the response of our edge detector to be independent of orientation, a circularly symmetric smoothing filter is desirable. As we saw in Section 3.2, the Gaussian is the only separable circularly symmetric filter and so it is used in most edge detection algorithms. Canny (1986) discusses alternative filters and a number of researcher review alternative edge detection algorithms and compare their performance (Davis 1975; Nalwa and Binford 1986; Nalwa 1987; Deriche 1987; Freeman and Adelson 1991; Nalwa 1993; Heath, Sarkar, Sanocki *et al.* 1998; Crane 1997; Ritter and Wilson 2000; Bowyer, Kranenburg, and Dougherty 2001; Arbeláez, Maire, Fowlkes *et al.* 2010).

Because differentiation is a linear operation, it commutes with other linear filtering oper-

[3] We defer the topic of edge detection in color images.

ations. The gradient of the smoothed image can therefore be written as

$$\boldsymbol{J}_\sigma(\boldsymbol{x}) = \nabla[G_\sigma(\boldsymbol{x}) * I(\boldsymbol{x})] = [\nabla G_\sigma](\boldsymbol{x}) * I(\boldsymbol{x}), \tag{4.20}$$

i.e., we can convolve the image with the horizontal and vertical derivatives of the Gaussian kernel function,

$$\nabla G_\sigma(\boldsymbol{x}) = (\frac{\partial G_\sigma}{\partial x}, \frac{\partial G_\sigma}{\partial y})(\boldsymbol{x}) = [-x \ -y]\frac{1}{\sigma^3}\exp\left(-\frac{x^2+y^2}{2\sigma^2}\right) \tag{4.21}$$

(The parameter σ indicates the width of the Gaussian.) This is the same computation that is performed by Freeman and Adelson's (1991) first-order steerable filter, which we already covered in Section 3.2.3.

For many applications, however, we wish to thin such a continuous gradient image to only return isolated edges, i.e., as single pixels at discrete locations along the edge contours. This can be achieved by looking for *maxima* in the edge strength (gradient magnitude) in a direction *perpendicular* to the edge orientation, i.e., along the gradient direction.

Finding this maximum corresponds to taking a directional derivative of the strength field in the direction of the gradient and then looking for zero crossings. The desired directional derivative is equivalent to the dot product between a second gradient operator and the results of the first,

$$S_\sigma(\boldsymbol{x}) = \nabla \cdot \boldsymbol{J}_\sigma(\boldsymbol{x}) = [\nabla^2 G_\sigma](\boldsymbol{x}) * I(\boldsymbol{x})]. \tag{4.22}$$

The gradient operator dot product with the gradient is called the *Laplacian*. The convolution kernel

$$\nabla^2 G_\sigma(\boldsymbol{x}) = \frac{1}{\sigma^3}\left(2 - \frac{x^2+y^2}{2\sigma^2}\right)\exp\left(-\frac{x^2+y^2}{2\sigma^2}\right) \tag{4.23}$$

is therefore called the *Laplacian of Gaussian* (LoG) kernel (Marr and Hildreth 1980). This kernel can be split into two separable parts,

$$\nabla^2 G_\sigma(\boldsymbol{x}) = \frac{1}{\sigma^3}\left(1 - \frac{x^2}{2\sigma^2}\right)G_\sigma(x)G_\sigma(y) + \frac{1}{\sigma^3}\left(1 - \frac{y^2}{2\sigma^2}\right)G_\sigma(y)G_\sigma(x) \tag{4.24}$$

(Wiejak, Buxton, and Buxton 1985), which allows for a much more efficient implementation using separable filtering (Section 3.2.1).

In practice, it is quite common to replace the Laplacian of Gaussian convolution with a Difference of Gaussian (DoG) computation, since the kernel shapes are qualitatively similar (Figure 3.35). This is especially convenient if a "Laplacian pyramid" (Section 3.5) has already been computed.[4]

[4] Recall that Burt and Adelson's (1983a) "Laplacian pyramid" actually computed differences of Gaussian-filtered levels.

In fact, it is not strictly necessary to take differences between adjacent levels when computing the edge field. Think about what a zero crossing in a "generalized" difference of Gaussians image represents. The finer (smaller kernel) Gaussian is a noise-reduced version of the original image. The coarser (larger kernel) Gaussian is an estimate of the average intensity over a larger region. Thus, whenever the DoG image changes sign, this corresponds to the (slightly blurred) image going from relatively darker to relatively lighter, as compared to the average intensity in that neighborhood.

Once we have computed the sign function $S(\boldsymbol{x})$, we must find its *zero crossings* and convert these into edge elements (*edgels*). An easy way to detect and represent zero crossings is to look for adjacent pixel locations $\boldsymbol{x}_i$ and $\boldsymbol{x}_j$ where the sign changes value, i.e., $[S(\boldsymbol{x}_i) > 0] \neq [S(\boldsymbol{x}_j) > 0]$.

The sub-pixel location of this crossing can be obtained by computing the "x-intercept" of the "line" connecting $S(\boldsymbol{x}_i)$ and $S(\boldsymbol{x}_j)$,

$$\boldsymbol{x}_z = \frac{\boldsymbol{x}_i S(\boldsymbol{x}_j) - \boldsymbol{x}_j S(\boldsymbol{x}_i)}{S(\boldsymbol{x}_j) - S(\boldsymbol{x}_i)}. \tag{4.25}$$

The orientation and strength of such edgels can be obtained by linearly interpolating the gradient values computed on the original pixel grid.

An alternative edgel representation can be obtained by linking adjacent edgels on the dual grid to form edgels that live *inside* each square formed by four adjacent pixels in the original pixel grid.[5] The (potential) advantage of this representation is that the edgels now live on a grid offset by half a pixel from the original pixel grid and are thus easier to store and access. As before, the orientations and strengths of the edges can be computed by interpolating the gradient field or estimating these values from the difference of Gaussian image (see Exercise 4.7).

In applications where the accuracy of the edge orientation is more important, higher-order steerable filters can be used (Freeman and Adelson 1991) (see Section 3.2.3). Such filters are more selective for more elongated edges and also have the possibility of better modeling curve intersections because they can represent multiple orientations at the same pixel (Figure 3.16). Their disadvantage is that they are more expensive to compute and the directional derivative of the edge strength does not have a simple closed form solution.[6]

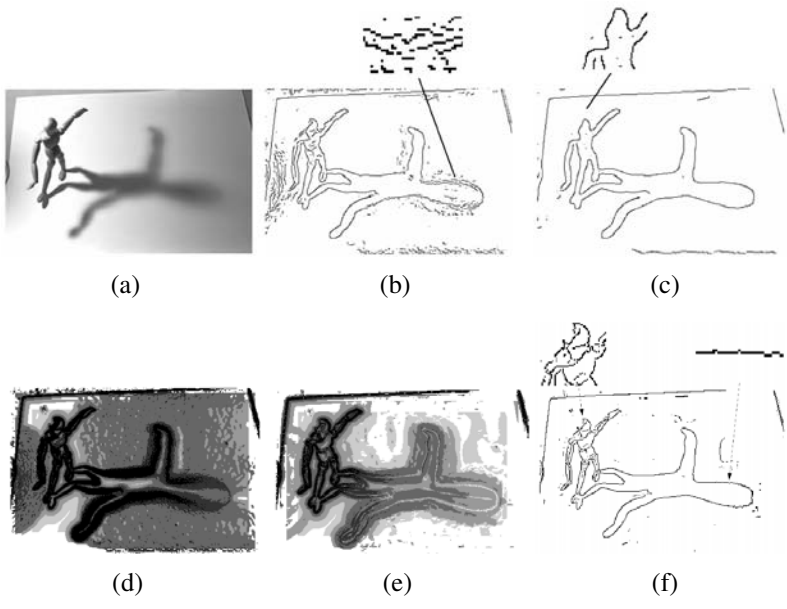

Figure 4.32 Scale selection for edge detection (Elder and Zucker 1998) © 1998 IEEE: (a) original image; (b–c) Canny/Deriche edge detector tuned to the finer (mannequin) and coarser (shadow) scales; (d) minimum reliable scale for gradient estimation; (e) minimum reliable scale for second derivative estimation; (f) final detected edges.

Scale selection and blur estimation

As we mentioned before, the derivative, Laplacian, and Difference of Gaussian filters (4.20–4.23) all require the selection of a spatial scale parameter σ. If we are only interested in detecting sharp edges, the width of the filter can be determined from image noise characteristics (Canny 1986; Elder and Zucker 1998). However, if we want to detect edges that occur at different resolutions (Figures 4.32b–c), a *scale-space* approach that detects and then selects edges at different scales may be necessary (Witkin 1983; Lindeberg 1994, 1998a; Nielsen, Florack, and Deriche 1997).

Elder and Zucker (1998) present a principled approach to solving this problem. Given a known image noise level, their technique computes, for every pixel, the minimum scale at which an edge can be reliably detected (Figure 4.32d). Their approach first computes

[5] This algorithm is a 2D version of the 3D *marching cubes* isosurface extraction algorithm (Lorensen and Cline 1987).

[6] In fact, the edge orientation can have a 180° ambiguity for "bar edges", which makes the computation of zero crossings in the derivative more tricky.

gradients densely over an image by selecting among gradient estimates computed at different scales, based on their gradient magnitudes. It then performs a similar estimate of minimum scale for directed second derivatives and uses zero crossings of this latter quantity to robustly select edges (Figures 4.32e–f). As an optional final step, the blur width of each edge can be computed from the distance between extrema in the second derivative response minus the width of the Gaussian filter.

Color edge detection

While most edge detection techniques have been developed for grayscale images, color images can provide additional information. For example, noticeable edges between *iso-luminant* colors (colors that have the same luminance) are useful cues but fail to be detected by grayscale edge operators.

One simple approach is to combine the outputs of grayscale detectors run on each color band separately.[7] However, some care must be taken. For example, if we simply sum up the gradients in each of the color bands, the signed gradients may actually cancel each other! (Consider, for example a pure red-to-green edge.) We could also detect edges independently in each band and then take the union of these, but this might lead to thickened or doubled edges that are hard to link.

A better approach is to compute the *oriented energy* in each band (Morrone and Burr 1988; Perona and Malik 1990a), e.g., using a second-order steerable filter (Section 3.2.3) (Freeman and Adelson 1991), and then sum up the orientation-weighted energies and find their joint best orientation. Unfortunately, the directional derivative of this energy may not have a closed form solution (as in the case of signed first-order steerable filters), so a simple zero crossing-based strategy cannot be used. However, the technique described by Elder and Zucker (1998) can be used to compute these zero crossings numerically instead.

An alternative approach is to estimate local color statistics in regions around each pixel (Ruzon and Tomasi 2001; Martin, Fowlkes, and Malik 2004). This has the advantage that more sophisticated techniques (e.g., 3D color histograms) can be used to compare regional statistics and that additional measures, such as texture, can also be considered. Figure 4.33 shows the output of such detectors.

Of course, many other approaches have been developed for detecting color edges, dating back to early work by Nevatia (1977). Ruzon and Tomasi (2001) and Gevers, van de Weijer, and Stokman (2006) provide good reviews of these approaches, which include ideas such as fusing outputs from multiple channels, using multidimensional gradients, and vector-based

[7] Instead of using the raw RGB space, a more perceptually uniform color space such as L*a*b* (see Section 2.3.2) can be used instead. When trying to match human performance (Martin, Fowlkes, and Malik 2004), this makes sense. However, in terms of the physics of the underlying image formation and sensing, it may be a questionable strategy.

methods.

Combining edge feature cues

If the goal of edge detection is to match human *boundary detection* performance (Bowyer, Kranenburg, and Dougherty 2001; Martin, Fowlkes, and Malik 2004; Arbeláez, Maire, Fowlkes *et al.* 2010), as opposed to simply finding stable features for matching, even better detectors can be constructed by combining multiple low-level cues such as brightness, color, and texture.

Martin, Fowlkes, and Malik (2004) describe a system that combines brightness, color, and texture edges to produce state-of-the-art performance on a database of hand-segmented natural color images (Martin, Fowlkes, Tal *et al.* 2001). First, they construct and train[8] separate oriented half-disc detectors for measuring significant differences in brightness (luminance), color (a* and b* channels, summed responses), and texture (un-normalized filter bank responses from the work of Malik, Belongie, Leung *et al.* (2001)). Some of the responses are then sharpened using a soft non-maximal suppression technique. Finally, the outputs of the three detectors are combined using a variety of machine-learning techniques, from which logistic regression is found to have the best tradeoff between speed, space and accuracy . The resulting system (see Figure 4.33 for some examples) is shown to outperform previously developed techniques. Maire, Arbelaez, Fowlkes *et al.* (2008) improve on these results by combining the detector based on local appearance with a *spectral* (segmentation-based) detector (Belongie and Malik 1998). In more recent work, Arbeláez, Maire, Fowlkes *et al.* (2010) build a hierarchical segmentation on top of this edge detector using a variant of the watershed algorithm.

4.2.2 Edge linking

While isolated edges can be useful for a variety of applications, such as line detection (Section 4.3) and sparse stereo matching (Section 11.2), they become even more useful when linked into continuous contours.

If the edges have been detected using zero crossings of some function, linking them up is straightforward, since adjacent edgels share common endpoints. Linking the edgels into chains involves picking up an unlinked edgel and following its neighbors in both directions. Either a sorted list of edgels (sorted first by x coordinates and then by y coordinates, for example) or a 2D array can be used to accelerate the neighbor finding. If edges were not detected using zero crossings, finding the continuation of an edgel can be tricky. In this case, comparing the orientation (and, optionally, phase) of adjacent edgels can be used for

[8] The training uses 200 labeled images and testing is performed on a different set of 100 images.

Figure 4.33 Combined brightness, color, texture boundary detector (Martin, Fowlkes, and Malik 2004) © 2004 IEEE. Successive rows show the outputs of the brightness gradient (BG), color gradient (CG), texture gradient (TG), and combined (BG+CG+TG) detectors. The final row shows human-labeled boundaries derived from a database of hand-segmented images (Martin, Fowlkes, Tal *et al.* 2001).

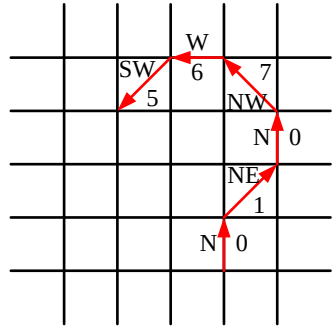

Figure 4.34 Chain code representation of a grid-aligned linked edge chain. The code is represented as a series of direction codes, e.g, 0 1 0 7 6 5, which can further be compressed using predictive and run-length coding.

disambiguation. Ideas from connected component computation can also sometimes be used to make the edge linking process even faster (see Exercise 4.8).

Once the edgels have been linked into chains, we can apply an optional thresholding with hysteresis to remove low-strength contour segments (Canny 1986). The basic idea of hysteresis is to set two different thresholds and allow a curve being tracked above the higher threshold to dip in strength down to the lower threshold.

Linked edgel lists can be encoded more compactly using a variety of alternative representations. A *chain code* encodes a list of connected points lying on an $\mathcal{N}_8$ grid using a three-bit code corresponding to the eight cardinal directions (N, NE, E, SE, S, SW, W, NW) between a point and its successor (Figure 4.34). While this representation is more compact than the original edgel list (especially if predictive variable-length coding is used), it is not very suitable for further processing.

A more useful representation is the *arc length parameterization* of a contour, $\boldsymbol{x}(s)$, where s denotes the arc length along a curve. Consider the linked set of edgels shown in Figure 4.35a. We start at one point (the dot at $(1.0, 0.5)$ in Figure 4.35a) and plot it at coordinate $s = 0$ (Figure 4.35b). The next point at $(2.0, 0.5)$ gets plotted at $s = 1$, and the next point at $(2.5, 1.0)$ gets plotted at $s = 1.7071$, i.e., we increment s by the length of each edge segment. The resulting plot can be resampled on a regular (say, integral) s grid before further processing.

The advantage of the arc-length parameterization is that it makes matching and processing (e.g., smoothing) operations much easier. Consider the two curves describing similar shapes shown in Figure 4.36. To compare the curves, we first subtract the average values $\boldsymbol{x}_0 = \int_s \boldsymbol{x}(s)$ from each descriptor. Next, we rescale each descriptor so that s goes from 0 to 1 instead of 0 to S, i.e., we divide $\boldsymbol{x}(s)$ by S. Finally, we take the Fourier transform of each

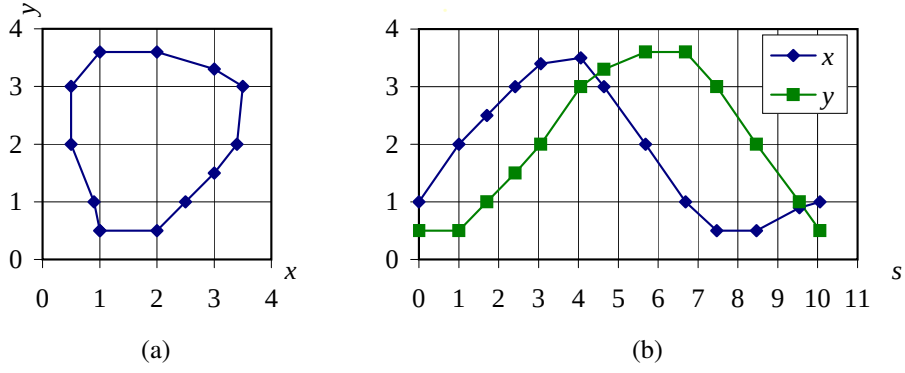

Figure 4.35 Arc-length parameterization of a contour: (a) discrete points along the contour are first transcribed as (b) (x, y) pairs along the arc length s. This curve can then be regularly re-sampled or converted into alternative (e.g., Fourier) representations.

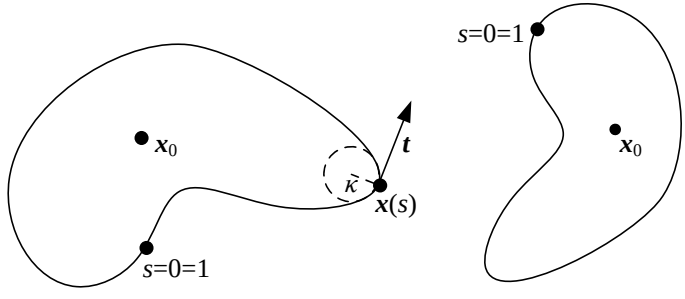

Figure 4.36 Matching two contours using their arc-length parameterization. If both curves are normalized to unit length, $s \in [0, 1]$ and centered around their centroid $\boldsymbol{x}_0$, they will have the same descriptor up to an overall "temporal" shift (due to different starting points for $s = 0$) and a phase (x-y) shift (due to rotation).

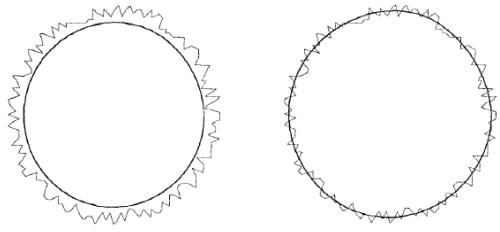

(a) (b)

Figure 4.37 Curve smoothing with a Gaussian kernel (Lowe 1988) © 1998 IEEE: (a) without a shrinkage correction term; (b) with a shrinkage correction term.

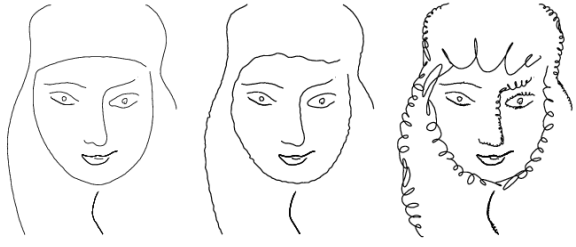

Figure 4.38 Changing the character of a curve without affecting its sweep (Finkelstein and Salesin 1994) © 1994 ACM: higher frequency wavelets can be replaced with exemplars from a style library to effect different local appearances.

normalized descriptor, treating each $\boldsymbol{x} = (x, y)$ value as a complex number. If the original curves are the same (up to an unknown scale and rotation), the resulting Fourier transforms should differ only by a scale change in magnitude plus a constant complex phase shift, due to rotation, and a linear phase shift in the domain, due to different starting points for s (see Exercise 4.9).

Arc-length parameterization can also be used to smooth curves in order to remove digitization noise. However, if we just apply a regular smoothing filter, the curve tends to shrink on itself (Figure 4.37a). Lowe (1989) and Taubin (1995) describe techniques that compensate for this shrinkage by adding an offset term based on second derivative estimates or a larger smoothing kernel (Figure 4.37b). An alternative approach, based on selectively modifying different frequencies in a wavelet decomposition, is presented by Finkelstein and Salesin (1994). In addition to controlling shrinkage without affecting its "sweep", wavelets allow the "character" of a curve to be interactively modified, as shown in Figure 4.38.

The evolution of curves as they are smoothed and simplified is related to "grassfire" (dis-

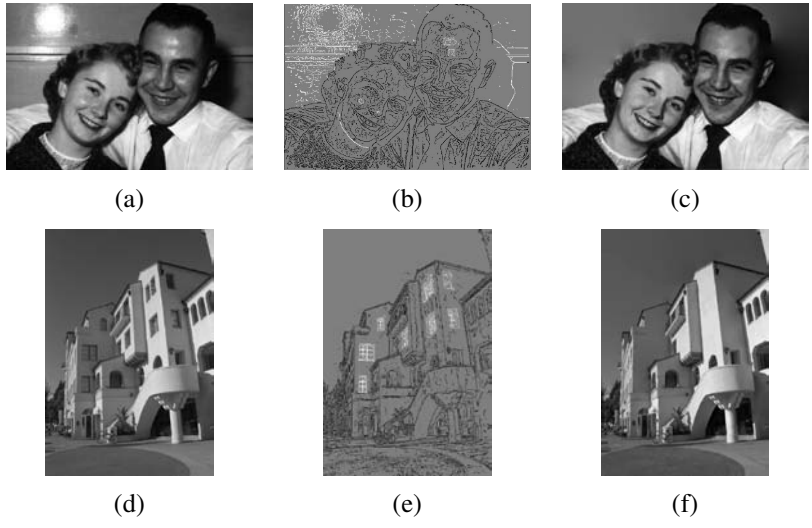

Figure 4.39 Image editing in the contour domain (Elder and Goldberg 2001) © 2001 IEEE: (a) and (d) original images; (b) and (e) extracted edges (edges to be deleted are marked in white); (c) and (f) reconstructed edited images.

tance) transforms and region skeletons (Section 3.3.3) (Tek and Kimia 2003), and can be used to recognize objects based on their contour shape (Sebastian and Kimia 2005). More local descriptors of curve shape such as *shape contexts* (Belongie, Malik, and Puzicha 2002) can also be used for recognition and are potentially more robust to missing parts due to occlusions.

The field of contour detection and linking continues to evolve rapidly and now includes techniques for global contour grouping, boundary completion, and junction detection (Maire, Arbelaez, Fowlkes *et al.* 2008), as well as grouping contours into likely regions (Arbeláez, Maire, Fowlkes *et al.* 2010) and wide-baseline correspondence (Meltzer and Soatto 2008).

4.2.3 *Application*: Edge editing and enhancement

While edges can serve as components for object recognition or features for matching, they can also be used directly for image editing.

In fact, if the edge magnitude and blur estimate are kept along with each edge, a visually similar image can be reconstructed from this information (Elder 1999). Based on this principle, Elder and Goldberg (2001) propose a system for "image editing in the contour domain". Their system allows users to selectively remove edges corresponding to unwanted features such as specularities, shadows, or distracting visual elements. After reconstructing the image from the remaining edges, the undesirable visual features have been removed (Figure 4.39).

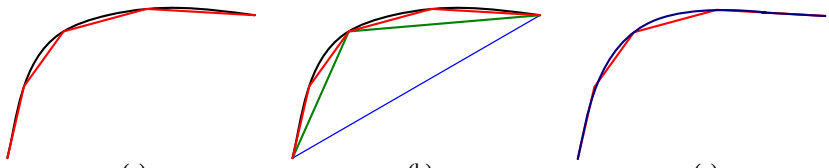

Figure 4.40 Approximating a curve (shown in black) as a polyline or B-spline: (a) original curve and a polyline approximation shown in red; (b) successive approximation by recursively finding points furthest away from the current approximation; (c) smooth interpolating spline, shown in dark blue, fit to the polyline vertices.

Another potential application is to enhance perceptually salient edges while simplifying the underlying image to produce a cartoon-like or "pen-and-ink" stylized image (DeCarlo and Santella 2002). This application is discussed in more detail in Section 10.5.2.

4.3 Lines

While edges and general curves are suitable for describing the contours of natural objects, the man-made world is full of straight lines. Detecting and matching these lines can be useful in a variety of applications, including architectural modeling, pose estimation in urban environments, and the analysis of printed document layouts.

In this section, we present some techniques for extracting *piecewise linear* descriptions from the curves computed in the previous section. We begin with some algorithms for approximating a curve as a piecewise-linear polyline. We then describe the *Hough transform*, which can be used to group edgels into line segments even across gaps and occlusions. Finally, we describe how 3D lines with common *vanishing points* can be grouped together. These vanishing points can be used to calibrate a camera and to determine its orientation relative to a rectahedral scene, as described in Section 6.3.2.

4.3.1 Successive approximation

As we saw in Section 4.2.2, describing a curve as a series of 2D locations $\boldsymbol{x}_i = \boldsymbol{x}(s_i)$ provides a general representation suitable for matching and further processing. In many applications, however, it is preferable to approximate such a curve with a simpler representation, e.g., as a piecewise-linear polyline or as a B-spline curve (Farin 1996), as shown in Figure 4.40.

Many techniques have been developed over the years to perform this approximation, which is also known as *line simplification*. One of the oldest, and simplest, is the one proposed

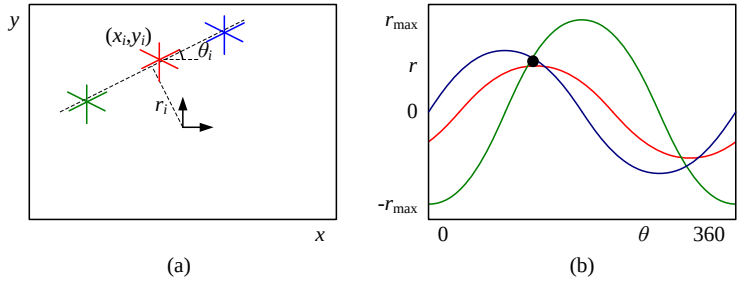

Figure 4.41 Original Hough transform: (a) each point votes for a complete family of potential lines $r_i(\theta) = x_i \cos\theta + y_i \sin\theta$; (b) each pencil of lines sweeps out a sinusoid in (r, θ); their intersection provides the desired line equation.

by Ramer (1972) and Douglas and Peucker (1973), who recursively subdivide the curve at the point furthest away from the line joining the two endpoints (or the current coarse polyline approximation), as shown in Figure 4.40. Hershberger and Snoeyink (1992) provide a more efficient implementation and also cite some of the other related work in this area.

Once the line simplification has been computed, it can be used to approximate the original curve. If a smoother representation or visualization is desired, either approximating or interpolating splines or curves can be used (Sections 3.5.1 and 5.1.1) (Szeliski and Ito 1986; Bartels, Beatty, and Barsky 1987; Farin 1996), as shown in Figure 4.40c.

4.3.2 Hough transforms

While curve approximation with polylines can often lead to successful line extraction, lines in the real world are sometimes broken up into disconnected components or made up of many collinear line segments. In many cases, it is desirable to group such collinear segments into extended lines. At a further processing stage (described in Section 4.3.3), we can then group such lines into collections with common vanishing points.

The Hough transform, named after its original inventor (Hough 1962), is a well-known technique for having edges "vote" for plausible line locations (Duda and Hart 1972; Ballard 1981; Illingworth and Kittler 1988). In its original formulation (Figure 4.41), each edge point votes for *all* possible lines passing through it, and lines corresponding to high *accumulator* or *bin* values are examined for potential line fits.[9] Unless the points on a line are truly punctate, a better approach (in my experience) is to use the local orientation information at each edgel to vote for a *single* accumulator cell (Figure 4.42), as described below. A hybrid strategy,

[9] The Hough transform can also be *generalized* to look for other geometric features such as circles (Ballard 1981), but we do not cover such extensions in this book.

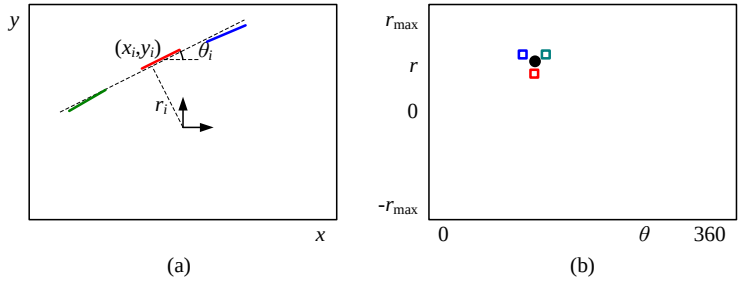

Figure 4.42 Oriented Hough transform: (a) an edgel re-parameterized in polar (r, θ) coordinates, with $\hat{\boldsymbol{n}}_i = (\cos\theta_i, \sin\theta_i)$ and $r_i = \hat{\boldsymbol{n}}_i \cdot \boldsymbol{x}_i$; (b) (r, θ) accumulator array, showing the votes for the three edgels marked in red, green, and blue.

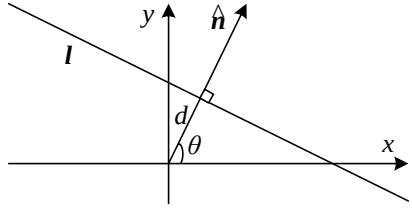

Figure 4.43 2D line equation expressed in terms of the normal $\hat{\boldsymbol{n}}$ and distance to the origin d.

where each edgel votes for a number of possible orientation or location pairs centered around the estimate orientation, may be desirable in some cases.

Before we can vote for line hypotheses, we must first choose a suitable representation. Figure 4.43 (copied from Figure 2.2a) shows the normal-distance $(\hat{\boldsymbol{n}}, d)$ parameterization for a line. Since lines are made up of edge segments, we adopt the convention that the line normal $\hat{\boldsymbol{n}}$ points in the same direction (i.e., has the same sign) as the image gradient $\boldsymbol{J}(\boldsymbol{x}) = \nabla I(\boldsymbol{x})$ (4.19). To obtain a minimal two-parameter representation for lines, we convert the normal vector into an angle

$$\theta = \tan^{-1} n_y / n_x, \tag{4.26}$$

as shown in Figure 4.43. The range of possible (θ, d) values is $[-180°, 180°] \times [-\sqrt{2}, \sqrt{2}]$, assuming that we are using normalized pixel coordinates (2.61) that lie in $[-1, 1]$. The number of bins to use along each axis depends on the accuracy of the position and orientation estimate available at each edgel and the expected line density, and is best set experimentally with some test runs on sample imagery.

Given the line parameterization, the Hough transform proceeds as shown in Algorithm 4.2.

procedure *Hough*$(\{(x, y, \theta)\})$:

1. Clear the accumulator array.
2. For each detected edgel at location (x, y) and orientation $\theta = \tan^{-1} n_y/n_x$, compute the value of
$$d = x\, n_x + y\, n_y$$
and increment the accumulator corresponding to (θ, d).
3. Find the peaks in the accumulator corresponding to lines.
4. Optionally re-fit the lines to the constituent edgels.

Algorithm 4.2 Outline of a Hough transform algorithm based on oriented edge segments.

Note that the original formulation of the Hough transform, which assumed no knowledge of the edgel orientation θ, has an additional loop inside Step 2 that iterates over all possible values of θ and increments a whole series of accumulators.

There are a lot of details in getting the Hough transform to work well, but these are best worked out by writing an implementation and testing it out on sample data. Exercise 4.12 describes some of these steps in more detail, including using edge segment lengths or strengths during the voting process, keeping a list of constituent edgels in the accumulator array for easier post-processing, and optionally combining edges of different "polarity" into the same line segments.

An alternative to the 2D polar (θ, d) representation for lines is to use the full 3D $\boldsymbol{m} = (\hat{\boldsymbol{n}}, d)$ line equation, projected onto the unit sphere. While the sphere can be parameterized using spherical coordinates (2.8),

$$\hat{\boldsymbol{m}} = (\cos\theta\cos\phi, \sin\theta\cos\phi, \sin\phi), \tag{4.27}$$

this does not uniformly sample the sphere and still requires the use of trigonometry.

An alternative representation can be obtained by using a *cube map*, i.e., projecting $\boldsymbol{m}$ onto the face of a unit cube (Figure 4.44a). To compute the cube map coordinate of a 3D vector $\boldsymbol{m}$, first find the largest (absolute value) component of $\boldsymbol{m}$, i.e., $m = \pm\max(|n_x|, |n_y|, |d|)$, and use this to select one of the six cube faces. Divide the remaining two coordinates by m and use these as indices into the cube face. While this avoids the use of trigonometry, it does require some decision logic.

One advantage of using the cube map, first pointed out by Tuytelaars, Van Gool, and Proesmans (1997), is that all of the lines passing through a point correspond to line segments

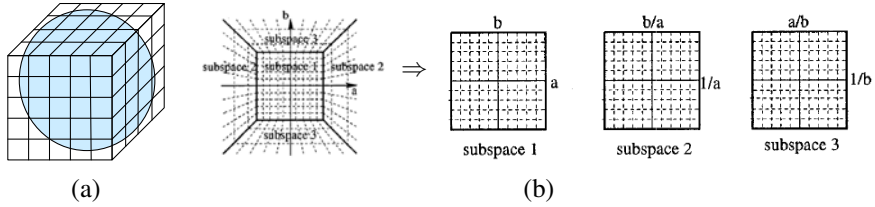

Figure 4.44 Cube map representation for line equations and vanishing points: (a) a cube map surrounding the unit sphere; (b) projecting the half-cube onto three subspaces (Tuytelaars, Van Gool, and Proesmans 1997) © 1997 IEEE.

on the cube faces, which is useful if the original (full voting) variant of the Hough transform is being used. In their work, they represent the line equation as $ax + b + y = 0$, which does not treat the x and y axes symmetrically. Note that if we restrict $d \geq 0$ by ignoring the polarity of the edge orientation (gradient sign), we can use a half-cube instead, which can be represented using only three cube faces, as shown in Figure 4.44b (Tuytelaars, Van Gool, and Proesmans 1997).

RANSAC-based line detection. Another alternative to the Hough transform is the RANdom SAmple Consensus (RANSAC) algorithm described in more detail in Section 6.1.4. In brief, RANSAC randomly chooses pairs of edgels to form a line hypothesis and then tests how many other edgels fall onto this line. (If the edge orientations are accurate enough, a single edgel can produce this hypothesis.) Lines with sufficiently large numbers of *inliers* (matching edgels) are then selected as the desired line segments.

An advantage of RANSAC is that no accumulator array is needed and so the algorithm can be more space efficient and potentially less prone to the choice of bin size. The disadvantage is that many more hypotheses may need to be generated and tested than those obtained by finding peaks in the accumulator array.

In general, there is no clear consensus on which line estimation technique performs best. It is therefore a good idea to think carefully about the problem at hand and to implement several approaches (successive approximation, Hough, and RANSAC) to determine the one that works best for your application.

4.3.3 Vanishing points

In many scenes, structurally important lines have the same vanishing point because they are parallel in 3D. Examples of such lines are horizontal and vertical building edges, zebra crossings, railway tracks, the edges of furniture such as tables and dressers, and of course, the ubiquitous calibration pattern (Figure 4.45). Finding the vanishing points common to such

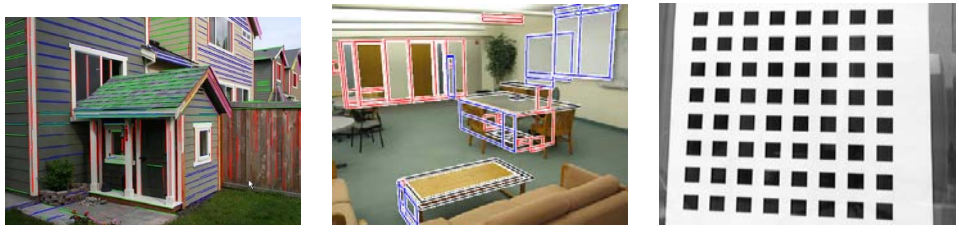

(a) (b) (c)

Figure 4.45 Real-world vanishing points: (a) architecture (Sinha, Steedly, Szeliski *et al.* 2008), (b) furniture (Mičušík, Wildenauer, and Košecká 2008) © 2008 IEEE, and (c) calibration patterns (Zhang 2000).

line sets can help refine their position in the image and, in certain cases, help determine the intrinsic and extrinsic orientation of the camera (Section 6.3.2).

Over the years, a large number of techniques have been developed for finding vanishing points, including (Quan and Mohr 1989; Collins and Weiss 1990; Brillaut-O'Mahoney 1991; McLean and Kotturi 1995; Becker and Bove 1995; Shufelt 1999; Tuytelaars, Van Gool, and Proesmans 1997; Schaffalitzky and Zisserman 2000; Antone and Teller 2002; Rother 2002; Košecká and Zhang 2005; Pflugfelder 2008; Tardif 2009)—see some of the more recent papers for additional references. In this section, we present a simple Hough technique based on having line pairs vote for potential vanishing point locations, followed by a robust least squares fitting stage. For alternative approaches, please see some of the more recent papers listed above.

The first stage in my vanishing point detection algorithm uses a Hough transform to accumulate votes for likely vanishing point candidates. As with line fitting, one possible approach is to have each line vote for *all* possible vanishing point directions, either using a cube map (Tuytelaars, Van Gool, and Proesmans 1997; Antone and Teller 2002) or a Gaussian sphere (Collins and Weiss 1990), optionally using knowledge about the uncertainty in the vanishing point location to perform a weighted vote (Collins and Weiss 1990; Brillaut-O'Mahoney 1991; Shufelt 1999). My preferred approach is to use pairs of detected line segments to form candidate vanishing point locations. Let $\hat{\boldsymbol{m}}_i$ and $\hat{\boldsymbol{m}}_j$ be the (unit norm) line equations for a pair of line segments and l_i and l_j be their corresponding segment lengths. The location of the corresponding vanishing point hypothesis can be computed as

$$\boldsymbol{v}_{ij} = \hat{\boldsymbol{m}}_i \times \hat{\boldsymbol{m}}_j \tag{4.28}$$

and the corresponding weight set to

$$w_{ij} = \|\boldsymbol{v}_{ij}\| l_i l_j. \tag{4.29}$$

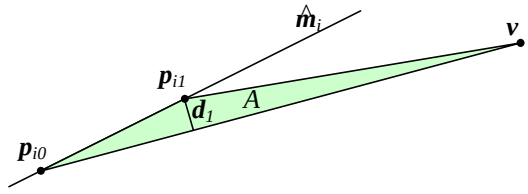

Figure 4.46 Triple product of the line segments endpoints $\boldsymbol{p}_{i0}$ and $\boldsymbol{p}_{i1}$ and the vanishing point $\boldsymbol{v}$. The area A is proportional to the perpendicular distance d_1 and the distance between the other endpoint $\boldsymbol{p}_{i0}$ and the vanishing point.

This has the desirable effect of downweighting (near-)collinear line segments and short line segments. The Hough space itself can either be represented using spherical coordinates (4.27) or as a cube map (Figure 4.44a).

Once the Hough accumulator space has been populated, peaks can be detected in a manner similar to that previously discussed for line detection. Given a set of candidate line segments that voted for a vanishing point, which can optionally be kept as a list at each Hough accumulator cell, I then use a robust least squares fit to estimate a more accurate location for each vanishing point.

Consider the relationship between the two line segment endpoints $\{\boldsymbol{p}_{i0}, \boldsymbol{p}_{i1}\}$ and the vanishing point $\boldsymbol{v}$, as shown in Figure 4.46. The area A of the triangle given by these three points, which is the magnitude of their triple product

$$A_i = |(\boldsymbol{p}_{i0} \times \boldsymbol{p}_{i1}) \cdot \boldsymbol{v}|, \tag{4.30}$$

is proportional to the perpendicular distance d_1 between each endpoint and the line through $\boldsymbol{v}$ and the other endpoint, as well as the distance between $\boldsymbol{p}_{i0}$ and $\boldsymbol{v}$. Assuming that the accuracy of a fitted line segment is proportional to its endpoint accuracy (Exercise 4.13), this therefore serves as an optimal metric for how well a vanishing point fits a set of extracted lines (Leibowitz (2001, Section 3.6.1) and Pflugfelder (2008, Section 2.1.1.3)). A robustified least squares estimate (Appendix B.3) for the vanishing point can therefore be written as

$$\mathcal{E} = \sum_i \rho(A_i) = \boldsymbol{v}^T \left(\sum_i w_i(A_i) \boldsymbol{m}_i \boldsymbol{m}_i^T \right) \boldsymbol{v} = \boldsymbol{v}^T \boldsymbol{M} \boldsymbol{v}, \tag{4.31}$$

where $\boldsymbol{m}_i = \boldsymbol{p}_{i0} \times \boldsymbol{p}_{i1}$ is the segment line equation weighted by its length l_i, and $w_i = \rho'(A_i)/A_i$ is the *influence* of each robustified (reweighted) measurement on the final error (Appendix B.3). Notice how this metric is closely related to the original formula for the pairwise weighted Hough transform accumulation step. The final desired value for $\boldsymbol{v}$ is computed as the least eigenvector of $\boldsymbol{M}$.

While the technique described above proceeds in two discrete stages, better results may be obtained by alternating between assigning lines to vanishing points and refitting the vanishing point locations (Antone and Teller 2002; Košecká and Zhang 2005; Pflugfelder 2008). The results of detecting individual vanishing points can also be made more robust by simultaneously searching for pairs or triplets of mutually orthogonal vanishing points (Shufelt 1999; Antone and Teller 2002; Rother 2002; Sinha, Steedly, Szeliski *et al.* 2008). Some results of such vanishing point detection algorithms can be seen in Figure 4.45.

4.3.4 *Application*: Rectangle detection

Once sets of mutually orthogonal vanishing points have been detected, it now becomes possible to search for 3D rectangular structures in the image (Figure 4.47). Over the last decade, a variety of techniques have been developed to find such rectangles, primarily focused on architectural scenes (Košecká and Zhang 2005; Han and Zhu 2005; Shaw and Barnes 2006; Mičušìk, Wildenauer, and Košecká 2008; Schindler, Krishnamurthy, Lublinerman *et al.* 2008).

After detecting orthogonal vanishing directions, Košecká and Zhang (2005) refine the fitted line equations, search for corners near line intersections, and then verify rectangle hypotheses by rectifying the corresponding patches and looking for a preponderance of horizontal and vertical edges (Figures 4.47a–b). In follow-on work, Mičušìk, Wildenauer, and Košecká (2008) use a Markov random field (MRF) to disambiguate between potentially overlapping rectangle hypotheses. They also use a plane sweep algorithm to match rectangles between different views (Figures 4.47d–f).

A different approach is proposed by Han and Zhu (2005), who use a grammar of potential rectangle shapes and nesting structures (between rectangles and vanishing points) to infer the most likely assignment of line segments to rectangles (Figure 4.47c).

4.4 Additional reading

One of the seminal papers on feature detection, description, and matching is by Lowe (2004). Comprehensive surveys and evaluations of such techniques have been made by Schmid, Mohr, and Bauckhage (2000); Mikolajczyk and Schmid (2005); Mikolajczyk, Tuytelaars, Schmid *et al.* (2005); Tuytelaars and Mikolajczyk (2007) while Shi and Tomasi (1994) and Triggs (2004) also provide nice reviews.

In the area of feature detectors (Mikolajczyk, Tuytelaars, Schmid *et al.* 2005), in addition to such classic approaches as Förstner–Harris (Förstner 1986; Harris and Stephens 1988) and difference of Gaussians (Lindeberg 1993, 1998b; Lowe 2004), maximally stable extremal regions (MSERs) are widely used for applications that require affine invariance (Matas, Chum,

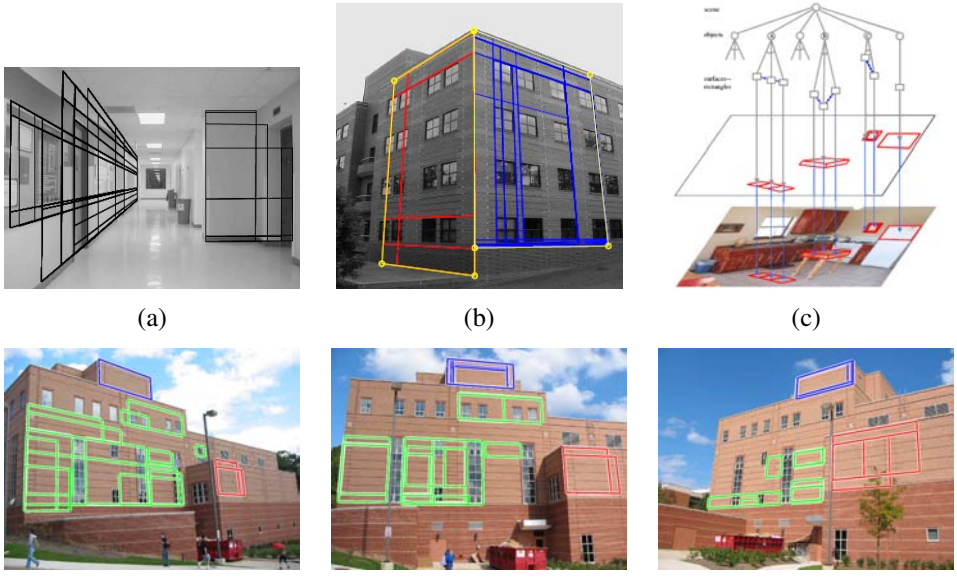

Figure 4.47 Rectangle detection: (a) indoor corridor and (b) building exterior with grouped facades (Košecká and Zhang 2005) © 2005 Elsevier; (c) grammar-based recognition (Han and Zhu 2005) © 2005 IEEE; (d–f) rectangle matching using a plane sweep algorithm (Mičušik, Wildenauer, and Košecká 2008) © 2008 IEEE.

Urban *et al.* 2004; Nistér and Stewénius 2008). More recent interest point detectors are discussed by Xiao and Shah (2003); Koethe (2003); Carneiro and Jepson (2005); Kenney, Zuliani, and Manjunath (2005); Bay, Tuytelaars, and Van Gool (2006); Platel, Balmachnova, Florack *et al.* (2006); Rosten and Drummond (2006), as well as techniques based on line matching (Zoghlami, Faugeras, and Deriche 1997; Bartoli, Coquerelle, and Sturm 2004) and region detection (Kadir, Zisserman, and Brady 2004; Matas, Chum, Urban *et al.* 2004; Tuytelaars and Van Gool 2004; Corso and Hager 2005).

A variety of local feature descriptors (and matching heuristics) are surveyed and compared by Mikolajczyk and Schmid (2005). More recent publications in this area include those by van de Weijer and Schmid (2006); Abdel-Hakim and Farag (2006); Winder and Brown (2007); Hua, Brown, and Winder (2007). Techniques for efficiently matching features include k-d trees (Beis and Lowe 1999; Lowe 2004; Muja and Lowe 2009), pyramid matching kernels (Grauman and Darrell 2005), metric (vocabulary) trees (Nistér and Stewénius 2006), and a variety of multi-dimensional hashing techniques (Shakhnarovich, Viola, and Darrell 2003; Torralba, Weiss, and Fergus 2008; Weiss, Torralba, and Fergus 2008; Kulis and

Grauman 2009; Raginsky and Lazebnik 2009).

The classic reference on feature detection and tracking is (Shi and Tomasi 1994). More recent work in this field has focused on learning better matching functions for specific features (Avidan 2001; Jurie and Dhome 2002; Williams, Blake, and Cipolla 2003; Lepetit and Fua 2005; Lepetit, Pilet, and Fua 2006; Hinterstoisser, Benhimane, Navab *et al.* 2008; Rogez, Rihan, Ramalingam *et al.* 2008; Özuysal, Calonder, Lepetit *et al.* 2010).

A highly cited and widely used edge detector is the one developed by Canny (1986). Alternative edge detectors as well as experimental comparisons can be found in publications by Nalwa and Binford (1986); Nalwa (1987); Deriche (1987); Freeman and Adelson (1991); Nalwa (1993); Heath, Sarkar, Sanocki *et al.* (1998); Crane (1997); Ritter and Wilson (2000); Bowyer, Kranenburg, and Dougherty (2001); Arbeláez, Maire, Fowlkes *et al.* (2010). The topic of scale selection in edge detection is nicely treated by Elder and Zucker (1998), while approaches to color and texture edge detection can be found in (Ruzon and Tomasi 2001; Martin, Fowlkes, and Malik 2004; Gevers, van de Weijer, and Stokman 2006). Edge detectors have also recently been combined with region segmentation techniques to further improve the detection of semantically salient boundaries (Maire, Arbelaez, Fowlkes *et al.* 2008; Arbeláez, Maire, Fowlkes *et al.* 2010). Edges linked into contours can be smoothed and manipulated for artistic effect (Lowe 1989; Finkelstein and Salesin 1994; Taubin 1995) and used for recognition (Belongie, Malik, and Puzicha 2002; Tek and Kimia 2003; Sebastian and Kimia 2005).

An early, well-regarded paper on straight line extraction in images was written by Burns, Hanson, and Riseman (1986). More recent techniques often combine line detection with vanishing point detection (Quan and Mohr 1989; Collins and Weiss 1990; Brillaut-O'Mahoney 1991; McLean and Kotturi 1995; Becker and Bove 1995; Shufelt 1999; Tuytelaars, Van Gool, and Proesmans 1997; Schaffalitzky and Zisserman 2000; Antone and Teller 2002; Rother 2002; Košecká and Zhang 2005; Pflugfelder 2008; Sinha, Steedly, Szeliski *et al.* 2008; Tardif 2009).

4.5 Exercises

Ex 4.1: Interest point detector Implement one or more keypoint detectors and compare their performance (with your own or with a classmate's detector).

Possible detectors:

- Laplacian or Difference of Gaussian;
- Förstner–Harris Hessian (try different formula variants given in (4.9–4.11));

- oriented/steerable filter, looking for either second-order high second response or two edges in a window (Koethe 2003), as discussed in Section 4.1.1.

Other detectors are described by Mikolajczyk, Tuytelaars, Schmid *et al.* (2005); Tuytelaars and Mikolajczyk (2007). Additional optional steps could include:

1. Compute the detections on a sub-octave pyramid and find 3D maxima.
2. Find local orientation estimates using steerable filter responses or a gradient histogramming method.
3. Implement non-maximal suppression, such as the adaptive technique of Brown, Szeliski, and Winder (2005).
4. Vary the window shape and size (pre-filter and aggregation).

To test for repeatability, download the code from http://www.robots.ox.ac.uk/~vgg/research/affine/ (Mikolajczyk, Tuytelaars, Schmid *et al.* 2005; Tuytelaars and Mikolajczyk 2007) or simply rotate or shear your own test images. (Pick a domain you may want to use later, e.g., for outdoor stitching.)

Be sure to measure and report the stability of your scale and orientation estimates.

Ex 4.2: Interest point descriptor Implement one or more descriptors (steered to local scale and orientation) and compare their performance (with your own or with a classmate's detector).

Some possible descriptors include

- contrast-normalized patches (Brown, Szeliski, and Winder 2005);
- SIFT (Lowe 2004);
- GLOH (Mikolajczyk and Schmid 2005);
- DAISY (Winder and Brown 2007; Tola, Lepetit, and Fua 2010).

Other detectors are described by Mikolajczyk and Schmid (2005).

Ex 4.3: ROC curve computation Given a pair of curves (histograms) plotting the number of matching and non-matching features as a function of Euclidean distance d as shown in Figure 4.23b, derive an algorithm for plotting a ROC curve (Figure 4.23a). In particular, let $t(d)$ be the distribution of true matches and $f(d)$ be the distribution of (false) non-matches. Write down the equations for the ROC, i.e., TPR(FPR), and the AUC.

(Hint: Plot the cumulative distributions $T(d) = \int t(d)$ and $F(d) = \int f(d)$ and see if these help you derive the TPR and FPR at a given threshold θ.)

Ex 4.4: Feature matcher After extracting features from a collection of overlapping or distorted images,[10] match them up by their descriptors either using nearest neighbor matching or a more efficient matching strategy such as a k-d tree.

See whether you can improve the accuracy of your matches using techniques such as the nearest neighbor distance ratio.

Ex 4.5: Feature tracker Instead of finding feature points independently in multiple images and then matching them, find features in the first image of a video or image sequence and then re-locate the corresponding points in the next frames using either search and gradient descent (Shi and Tomasi 1994) or learned feature detectors (Lepetit, Pilet, and Fua 2006; Fossati, Dimitrijevic, Lepetit *et al.* 2007). When the number of tracked points drops below a threshold or new regions in the image become visible, find additional points to track.

(Optional) Winnow out incorrect matches by estimating a homography (6.19–6.23) or fundamental matrix (Section 7.2.1).

(Optional) Refine the accuracy of your matches using the iterative registration algorithm described in Section 8.2 and Exercise 8.2.

Ex 4.6: Facial feature tracker Apply your feature tracker to tracking points on a person's face, either manually initialized to interesting locations such as eye corners or automatically initialized at interest points.

(Optional) Match features between two people and use these features to perform image morphing (Exercise 3.25).

Ex 4.7: Edge detector Implement an edge detector of your choice. Compare its performance to that of your classmates' detectors or code downloaded from the Internet.

A simple but well-performing sub-pixel edge detector can be created as follows:

1. Blur the input image a little,

$$B_\sigma(\boldsymbol{x}) = G_\sigma(\boldsymbol{x}) * I(\boldsymbol{x}).$$

2. Construct a Gaussian pyramid (Exercise 3.19),

$$P = \text{Pyramid}\{B_\sigma(\boldsymbol{x})\}$$

3. Subtract an interpolated coarser-level pyramid image from the original resolution blurred image,

$$S(\boldsymbol{x}) = B_\sigma(\boldsymbol{x}) - P.\text{InterpolatedLevel}(L).$$

[10] http://www.robots.ox.ac.uk/~vgg/research/affine/.

```
struct SEdgel {
    float e[2][2];      // edgel endpoints (zero crossing)
    float x, y;         // sub-pixel edge position (midpoint)
    float n_x, n_y;     // orientation, as normal vector
    float theta;        // orientation, as angle (degrees)
    float length;       // length of edgel
    float strength;     // strength of edgel (gradient magnitude)
};

struct SLine : public SEdgel {
    float line_length;  // length of line (est. from ellipsoid)
    float sigma;        // estimated std. dev. of edgel noise
    float r;            // line equation: x * n_y - y * n_x = r
};
```

Figure 4.48 A potential C++ structure for edgel and line elements.

4. For each quad of pixels, $\{(i,j),(i+1,j),(i,j+1),(i+1,j+1)\}$, count the number of zero crossings along the four edges.

5. When there are exactly two zero crossings, compute their locations using (4.25) and store these edgel endpoints along with the midpoint in the edgel structure (Figure 4.48).

6. For each edgel, compute the local gradient by taking the horizontal and vertical differences between the values of S along the zero crossing edges.

7. Store the magnitude of this gradient as the edge strength and either its orientation or that of the segment joining the edgel endpoints as the edge orientation.

8. Add the edgel to a list of edgels or store it in a 2D array of edgels (addressed by pixel coordinates).

Figure 4.48 shows a possible representation for each computed edgel.

Ex 4.8: Edge linking and thresholding Link up the edges computed in the previous exercise into chains and optionally perform thresholding with hysteresis.

The steps may include:

1. Store the edgels either in a 2D array (say, an integer image with indices into the edgel list) or pre-sort the edgel list first by (integer) x coordinates and then y coordinates, for faster neighbor finding.

2. Pick up an edgel from the list of unlinked edgels and find its neighbors in both directions until no neighbor is found or a closed contour is obtained. Flag edgels as linked as you visit them and push them onto your list of linked edgels.

3. Alternatively, generalize a previously developed connected component algorithm (Exercise 3.14) to perform the linking in just two raster passes.

4. (Optional) Perform hysteresis-based thresholding (Canny 1986). Use two thresholds "hi" and "lo" for the edge strength. A candidate edgel is considered an edge if either its strength is above the "hi" threshold or its strength is above the "lo" threshold and it is (recursively) connected to a previously detected edge.

5. (Optional) Link together contours that have small gaps but whose endpoints have similar orientations.

6. (Optional) Find junctions between adjacent contours, e.g., using some of the ideas (or references) from Maire, Arbelaez, Fowlkes *et al.* (2008).

Ex 4.9: Contour matching Convert a closed contour (linked edgel list) into its arc-length parameterization and use this to match object outlines.

The steps may include:

1. Walk along the contour and create a list of (x_i, y_i, s_i) triplets, using the arc-length formula
$$s_{i+1} = s_i + \|\boldsymbol{x}_{i+1} - \boldsymbol{x}_i\|. \tag{4.32}$$

2. Resample this list onto a regular set of (x_j, y_j, j) samples using linear interpolation of each segment.

3. Compute the average values of x and y, i.e., $\overline{x}$ and $\overline{y}$ and subtract them from your sampled curve points.

4. Resample the original (x_i, y_i, s_i) piecewise-linear function onto a length-independent set of samples, say $j \in [0, 1023]$. (Using a length which is a power of two makes subsequent Fourier transforms more convenient.)

5. Compute the Fourier transform of the curve, treating each (x, y) pair as a complex number.

6. To compare two curves, fit a linear equation to the phase difference between the two curves. (Careful: phase wraps around at $360°$. Also, you may wish to weight samples by their Fourier spectrum magnitude—see Section 8.1.2.)

7. (Optional) Prove that the constant phase component corresponds to the temporal shift in s, while the linear component corresponds to rotation.

Of course, feel free to try any other curve descriptor and matching technique from the computer vision literature (Tek and Kimia 2003; Sebastian and Kimia 2005).

Ex 4.10: Jigsaw puzzle solver—challenging Write a program to automatically solve a jigsaw puzzle from a set of scanned puzzle pieces. Your software may include the following components:

1. Scan the pieces (either face up or face down) on a flatbed scanner with a distinctively colored background.
2. (Optional) Scan in the box top to use as a low-resolution reference image.
3. Use color-based thresholding to isolate the pieces.
4. Extract the contour of each piece using edge finding and linking.
5. (Optional) Re-represent each contour using an arc-length or some other re-parameterization. Break up the contours into meaningful matchable pieces. (Is this hard?)
6. (Optional) Associate color values with each contour to help in the matching.
7. (Optional) Match pieces to the reference image using some rotationally invariant feature descriptors.
8. Solve a global optimization or (backtracking) search problem to snap pieces together and place them in the correct location relative to the reference image.
9. Test your algorithm on a succession of more difficult puzzles and compare your results with those of others.

Ex 4.11: Successive approximation line detector Implement a line simplification algorithm (Section 4.3.1) (Ramer 1972; Douglas and Peucker 1973) to convert a hand-drawn curve (or linked edge image) into a small set of polylines.

(Optional) Re-render this curve using either an approximating or interpolating spline or Bezier curve (Szeliski and Ito 1986; Bartels, Beatty, and Barsky 1987; Farin 1996).

Ex 4.12: Hough transform line detector Implement a Hough transform for finding lines in images:

1. Create an accumulator array of the appropriate user-specified size and clear it. The user can specify the spacing in degrees between orientation bins and in pixels between distance bins. The array can be allocated as integer (for simple counts), floating point (for weighted counts), or as an array of vectors for keeping back pointers to the constituent edges.

2. For each detected edgel at location (x, y) and orientation $\theta = \tan^{-1} n_y/n_x$, compute the value of
$$d = xn_x + yn_y \tag{4.33}$$
and increment the accumulator corresponding to (θ, d).

   (Optional) Weight the vote of each edge by its length (see Exercise 4.7) or the strength of its gradient.

3. (Optional) Smooth the scalar accumulator array by adding in values from its immediate neighbors. This can help counteract the *discretization* effect of voting for only a single bin—see Exercise 3.7.

4. Find the largest peaks (local maxima) in the accumulator corresponding to lines.

5. (Optional) For each peak, re-fit the lines to the constituent edgels, using *total least squares* (Appendix A.2). Use the original edgel lengths or strength weights to weight the least squares fit, as well as the agreement between the hypothesized line orientation and the edgel orientation. Determine whether these heuristics help increase the accuracy of the fit.

6. After fitting each peak, zero-out or eliminate that peak and its adjacent bins in the array, and move on to the next largest peak.

Test out your Hough transform on a variety of images taken indoors and outdoors, as well as checkerboard calibration patterns.

For checkerboard patterns, you can modify your Hough transform by collapsing *antipodal* bins $(\theta \pm 180°, -d)$ with (θ, d) to find lines that do not care about polarity changes. Can you think of examples in real-world images where this might be desirable as well?

Ex 4.13: Line fitting uncertainty Estimate the uncertainty (covariance) in your line fit using uncertainty analysis.

1. After determining which edgels belong to the line segment (using either successive approximation or Hough transform), re-fit the line segment using total least squares (Van Huffel and Vandewalle 1991; Van Huffel and Lemmerling 2002), i.e., find the mean or centroid of the edgels and then use eigenvalue analysis to find the dominant orientation.

2. Compute the perpendicular errors (deviations) to the line and robustly estimate the variance of the fitting noise using an estimator such as MAD (Appendix B.3).

3. (Optional) re-fit the line parameters by throwing away outliers or using a robust norm or influence function.

4. Estimate the error in the perpendicular location of the line segment and its orientation.

Ex 4.14: Vanishing points Compute the vanishing points in an image using one of the techniques described in Section 4.3.3 and optionally refine the original line equations associated with each vanishing point. Your results can be used later to track a target (Exercise 6.5) or reconstruct architecture (Section 12.6.1).

Ex 4.15: Vanishing point uncertainty Perform an uncertainty analysis on your estimated vanishing points. You will need to decide how to represent your vanishing point, e.g., homogeneous coordinates on a sphere, to handle vanishing points near infinity.

See the discussion of Bingham distributions by Collins and Weiss (1990) for some ideas.

Chapter 5

Segmentation

5.1 Active contours 270
5.1.1 Snakes 270
5.1.2 Dynamic snakes and CONDENSATION 276
5.1.3 Scissors 280
5.1.4 Level Sets 281
5.1.5 *Application*: Contour tracking and rotoscoping 282
5.2 Split and merge 284
5.2.1 Watershed 284
5.2.2 Region splitting (divisive clustering) 286
5.2.3 Region merging (agglomerative clustering) 286
5.2.4 Graph-based segmentation 286
5.2.5 Probabilistic aggregation 288
5.3 Mean shift and mode finding 289
5.3.1 K-means and mixtures of Gaussians 289
5.3.2 Mean shift 292
5.4 Normalized cuts 296
5.5 Graph cuts and energy-based methods 300
5.5.1 *Application*: Medical image segmentation 304
5.6 Additional reading 305
5.7 Exercises 306

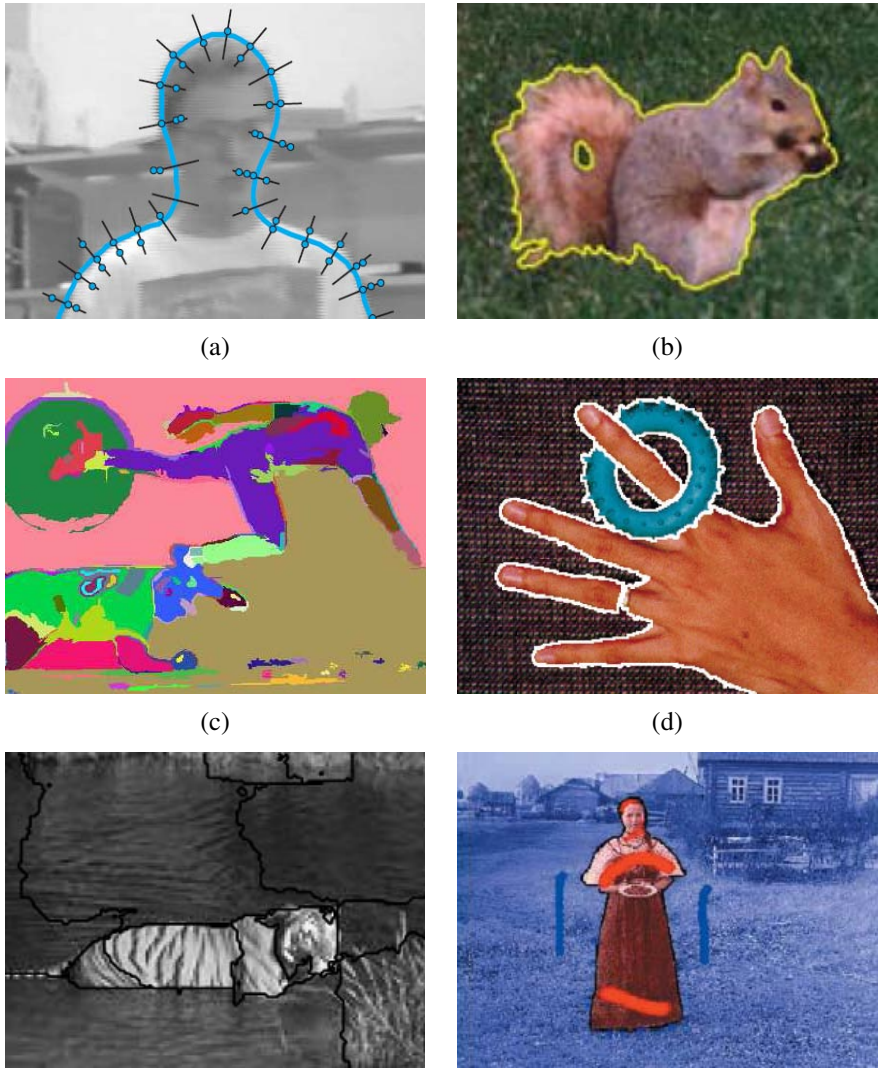

Figure 5.1 Some popular image segmentation techniques: (a) active contours (Isard and Blake 1998) © 1998 Springer; (b) level sets (Cremers, Rousson, and Deriche 2007) © 2007 Springer; (c) graph-based merging (Felzenszwalb and Huttenlocher 2004b) © 2004 Springer; (d) mean shift (Comaniciu and Meer 2002) © 2002 IEEE; (e) texture and intervening contour-based normalized cuts (Malik, Belongie, Leung *et al.* 2001) © 2001 Springer; (f) binary MRF solved using graph cuts (Boykov and Funka-Lea 2006) © 2006 Springer.

Image segmentation is the task of finding groups of pixels that "go together". In statistics, this problem is known as *cluster analysis* and is a widely studied area with hundreds of different algorithms (Jain and Dubes 1988; Kaufman and Rousseeuw 1990; Jain, Duin, and Mao 2000; Jain, Topchy, Law *et al.* 2004).

In computer vision, image segmentation is one of the oldest and most widely studied problems (Brice and Fennema 1970; Pavlidis 1977; Riseman and Arbib 1977; Ohlander, Price, and Reddy 1978; Rosenfeld and Davis 1979; Haralick and Shapiro 1985). Early techniques tend to use region splitting or merging (Brice and Fennema 1970; Horowitz and Pavlidis 1976; Ohlander, Price, and Reddy 1978; Pavlidis and Liow 1990), which correspond to *divisive* and *agglomerative* algorithms in the clustering literature (Jain, Topchy, Law *et al.* 2004). More recent algorithms often optimize some global criterion, such as intra-region consistency and inter-region boundary lengths or dissimilarity (Leclerc 1989; Mumford and Shah 1989; Shi and Malik 2000; Comaniciu and Meer 2002; Felzenszwalb and Huttenlocher 2004b; Cremers, Rousson, and Deriche 2007).

We have already seen examples of image segmentation in Sections 3.3.2 and 3.7.2. In this chapter, we review some additional techniques that have been developed for image segmentation. These include algorithms based on active contours (Section 5.1) and level sets (Section 5.1.4), region splitting and merging (Section 5.2), *mean shift* (mode finding) (Section 5.3), *normalized cuts* (splitting based on pixel similarity metrics) (Section 5.4), and binary Markov random fields solved using graph cuts (Section 5.5). Figure 5.1 shows some examples of these techniques applied to different images.

Since the literature on image segmentation is so vast, a good way to get a handle on some of the better performing algorithms is to look at experimental comparisons on human-labeled databases (Arbeláez, Maire, Fowlkes *et al.* 2010). The best known of these is the Berkeley Segmentation Dataset and Benchmark[1] (Martin, Fowlkes, Tal *et al.* 2001), which consists of 1000 images from a Corel image dataset that were hand-labeled by 30 human subjects. Many of the more recent image segmentation algorithms report comparative results on this database. For example, Unnikrishnan, Pantofaru, and Hebert (2007) propose new metrics for comparing such algorithms. Estrada and Jepson (2009) compare four well-known segmentation algorithms on the Berkeley data set and conclude that while their own SE-MinCut algorithm (Estrada, Jepson, and Chennubhotla 2004) algorithm outperforms the others by a small margin, there still exists a wide gap between automated and human segmentation performance.[2] A new database of foreground and background segmentations, used by Alpert, Galun, Basri *et al.* (2007), is also available.[3]

[1] http://www.eecs.berkeley.edu/Research/Projects/CS/vision/grouping/segbench/

[2] An interesting observation about their ROC plots is that automated techniques cluster tightly along similar curves, but human performance is all over the map.

[3] http://www.wisdom.weizmann.ac.il/~vision/Seg_Evaluation_DB/index.html

5.1 Active contours

While lines, vanishing points, and rectangles are commonplace in the man-made world, curves corresponding to object boundaries are even more common, especially in the natural environment. In this section, we describe three related approaches to locating such boundary curves in images.

The first, originally called *snakes* by its inventors (Kass, Witkin, and Terzopoulos 1988) (Section 5.1.1), is an energy-minimizing, two-dimensional spline curve that evolves (moves) towards image features such as strong edges. The second, *intelligent scissors* (Mortensen and Barrett 1995) (Section 5.1.3), allow the user to sketch in real time a curve that clings to object boundaries. Finally, *level set* techniques (Section 5.1.4) evolve the curve as the zero-set of a *characteristic function*, which allows them to easily change topology and incorporate region-based statistics.

All three of these are examples of *active contours* (Blake and Isard 1998; Mortensen 1999), since these boundary detectors iteratively move towards their final solution under the combination of image and optional user-guidance forces.

5.1.1 Snakes

Snakes are a two-dimensional generalization of the 1D energy-minimizing splines first introduced in Section 3.7.1,

$$\mathcal{E}_{\text{int}} = \int \alpha(s)\|\boldsymbol{f}_s(s)\|^2 + \beta(s)\|\boldsymbol{f}_{ss}(s)\|^2\, ds, \tag{5.1}$$

where s is the arc-length along the curve $\boldsymbol{f}(s) = (x(s), y(s))$ and $\alpha(s)$ and $\beta(s)$ are first- and second-order continuity weighting functions analogous to the $s(x, y)$ and $c(x, y)$ terms introduced in (3.100–3.101). We can discretize this energy by sampling the initial curve position evenly along its length (Figure 4.35) to obtain

$$\begin{aligned} E_{\text{int}} &= \sum_i \alpha(i)\|f(i+1) - f(i)\|^2/h^2 \\ &\quad + \beta(i)\|f(i+1) - 2f(i) + f(i-1)\|^2/h^4, \end{aligned} \tag{5.2}$$

where h is the step size, which can be neglected if we resample the curve along its arc-length after each iteration.

In addition to this *internal* spline energy, a snake simultaneously minimizes external image-based and constraint-based potentials. The image-based potentials are the sum of several terms

$$\mathcal{E}_{\text{image}} = w_{\text{line}}\mathcal{E}_{\text{line}} + w_{\text{edge}}\mathcal{E}_{\text{edge}} + w_{\text{term}}\mathcal{E}_{\text{term}}, \tag{5.3}$$

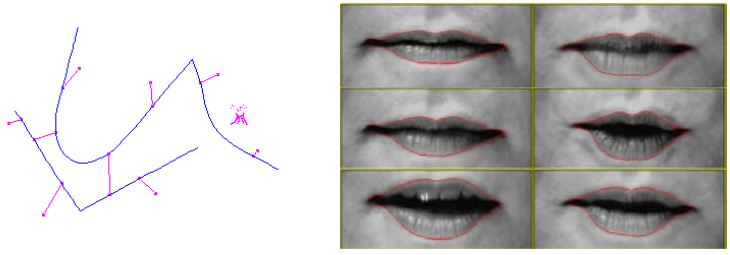

(a) (b)

Figure 5.2 Snakes (Kass, Witkin, and Terzopoulos 1988) © 1988 Springer: (a) the "snake pit" for interactively controlling shape; (b) lip tracking.

where the *line* term attracts the snake to dark ridges, the *edge* term attracts it to strong gradients (edges), and the *term* term attracts it to line terminations. In practice, most systems only use the edge term, which can either be directly proportional to the image gradients,

$$E_{\text{edge}} = \sum_i -\|\nabla I(\boldsymbol{f}(i))\|^2, \tag{5.4}$$

or to a smoothed version of the image Laplacian,

$$E_{\text{edge}} = \sum_i -|(G_\sigma * \nabla^2 I)(\boldsymbol{f}(i))|^2. \tag{5.5}$$

People also sometimes extract edges and then use a distance map to the edges as an alternative to these two originally proposed potentials.

In interactive applications, a variety of user-placed constraints can also be added, e.g., attractive (spring) forces towards anchor points $\boldsymbol{d}(i)$,

$$E_{\text{spring}} = k_i\|\boldsymbol{f}(i) - \boldsymbol{d}(i)\|^2, \tag{5.6}$$

as well as repulsive $1/r$ ("volcano") forces (Figure 5.2a). As the snakes evolve by minimizing their energy, they often "wiggle" and "slither", which accounts for their popular name. Figure 5.2b shows snakes being used to track a person's lips.

Because regular snakes have a tendency to shrink (Exercise 5.1), it is usually better to initialize them by drawing the snake outside the object of interest to be tracked. Alternatively, an expansion *ballooning* force can be added to the dynamics (Cohen and Cohen 1993), essentially moving each point outwards along its normal.

To efficiently solve the sparse linear system arising from snake energy minimization, a sparse direct solver (Appendix A.4) can be used, since the linear system is essentially pentadiagonal.[4] Snake evolution is usually implemented as an alternation between this linear sys-

[4] A closed snake has a Toeplitz matrix form, which can still be factored and solved in $O(N)$ time.

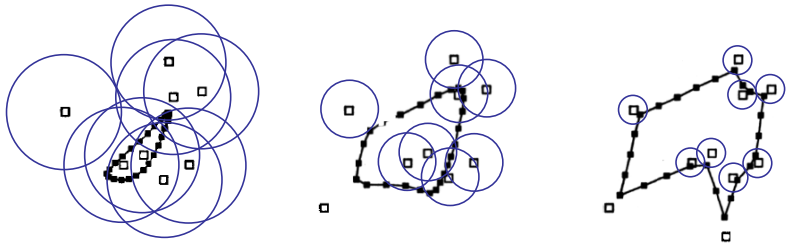

Figure 5.3 Elastic net: The open squares indicate the cities and the closed squares linked by straight line segments are the tour points. The blue circles indicate the approximate extent of the attraction force of each city, which is reduced over time. Under the Bayesian interpretation of the elastic net, the blue circles correspond to one standard deviation of the circular Gaussian that generates each city from some unknown tour point.

tem solution and the linearization of non-linear constraints such as edge energy. A more direct way to find a global energy minimum is to use dynamic programming (Amini, Weymouth, and Jain 1990; Williams and Shah 1992), but this is not often used in practice, since it has been superseded by even more efficient or interactive algorithms such as intelligent scissors (Section 5.1.3) and GrabCut (Section 5.5).

Elastic nets and slippery springs

An interesting variant on snakes, first proposed by Durbin and Willshaw (1987) and later re-formulated in an energy-minimizing framework by Durbin, Szeliski, and Yuille (1989), is the *elastic net* formulation of the Traveling Salesman Problem (TSP). Recall that in a TSP, the salesman must visit each city once while minimizing the total distance traversed. A snake that is constrained to pass through each city could solve this problem (without any optimality guarantees) but it is impossible to tell ahead of time which snake control point should be associated with each city.

Instead of having a fixed constraint between snake nodes and cities, as in (5.6), a city is assumed to pass near *some* point along the tour (Figure 5.3). In a probabilistic interpretation, each city is generated as a *mixture* of Gaussians centered at each tour point,

$$p(\boldsymbol{d}(j)) = \sum_i p_{ij} \quad \text{with} \quad p_{ij} = e^{-d_{ij}^2/(2\sigma^2)} \tag{5.7}$$

where σ is the standard deviation of the Gaussian and

$$d_{ij} = \|\boldsymbol{f}(i) - \boldsymbol{d}(j)\| \tag{5.8}$$

is the Euclidean distance between a tour point $\boldsymbol{f}(i)$ and a city location $\boldsymbol{d}(j)$. The corresponding data fitting energy (negative log likelihood) is

$$E_{\text{slippery}} = -\sum_j \log p(\boldsymbol{d}(j)) = -\sum_j \log \left[\sum e^{-\|\boldsymbol{f}(i)-\boldsymbol{d}(j)\|^2/2\sigma^2} \right]. \tag{5.9}$$

This energy derives its name from the fact that, unlike a regular spring, which couples a given snake point to a given constraint (5.6), this alternative energy defines a *slippery spring* that allows the association between constraints (cities) and curve (tour) points to evolve over time (Szeliski 1989). Note that this is a soft variant of the popular *iterated closest point* data constraint that is often used in fitting or aligning surfaces to data points or to each other (Section 12.2.1) (Besl and McKay 1992; Zhang 1994).

To compute a good solution to the TSP, the slippery spring data association energy is combined with a regular first-order internal smoothness energy (5.3) to define the cost of a tour. The tour $\boldsymbol{f}(s)$ is initialized as a small circle around the mean of the city points and σ is progressively lowered (Figure 5.3). For large σ values, the tour tries to stay near the centroid of the points but as σ decreases each city pulls more and more strongly on its closest tour points (Durbin, Szeliski, and Yuille 1989). In the limit as $\sigma \to 0$, each city is guaranteed to capture at least one tour point and the tours between subsequent cites become straight lines.

Splines and shape priors

While snakes can be very good at capturing the fine and irregular detail in many real-world contours, they sometimes exhibit too many degrees of freedom, making it more likely that they can get trapped in local minima during their evolution.

One solution to this problem is to control the snake with fewer degrees of freedom through the use of B-spline approximations (Menet, Saint-Marc, and Medioni 1990b,a; Cipolla and Blake 1990). The resulting *B-snake* can be written as

$$\boldsymbol{f}(s) = \sum_k B_k(s)\boldsymbol{x}_k \tag{5.10}$$

or in discrete form as

$$\boldsymbol{F} = \boldsymbol{B}\boldsymbol{X} \tag{5.11}$$

with

$$\boldsymbol{F} = \begin{bmatrix} \boldsymbol{f}^T(0) \\ \vdots \\ \boldsymbol{f}^T(N) \end{bmatrix}, \quad \boldsymbol{B} = \begin{bmatrix} B_0(s_0) & \dots & B_K(s_0) \\ \vdots & \ddots & \vdots \\ B_0(s_N) & \dots & B_K(s_N) \end{bmatrix}, \quad \text{and} \quad \boldsymbol{X} = \begin{bmatrix} \boldsymbol{x}^T(0) \\ \vdots \\ \boldsymbol{x}^T(K) \end{bmatrix}. \tag{5.12}$$

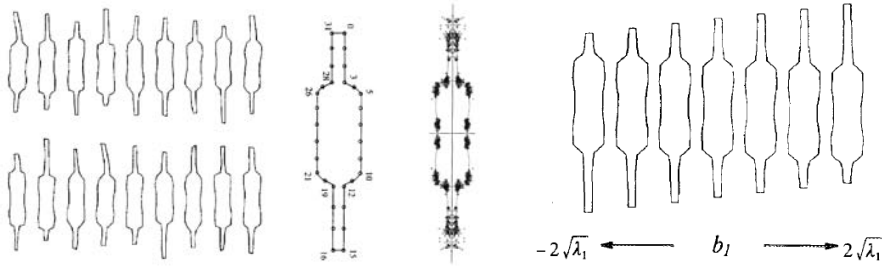

(a) (b) (c) (d)

Figure 5.4 Point distribution model for a set of resistors (Cootes, Cooper, Taylor *et al.* 1995) © 1995 Elsevier: (a) set of input resistor shapes; (b) assignment of control points to the boundary; (c) distribution (scatter plot) of point locations; (d) first (largest) mode of variation in the ensemble shapes.

If the object being tracked or recognized has large variations in location, scale, or orientation, these can be modeled as an additional transformation on the control points, e.g., $\boldsymbol{x}'_k = s\boldsymbol{R}\boldsymbol{x}_k + \boldsymbol{t}$ (2.18), which can be estimated at the same time as the values of the control points. Alternatively, separate *detection* and *alignment* stages can be run to first localize and orient the objects of interest (Cootes, Cooper, Taylor *et al.* 1995).

In a B-snake, because the snake is controlled by fewer degrees of freedom, there is less need for the internal smoothness forces used with the original snakes, although these can still be derived and implemented using finite element analysis, i.e., taking derivatives and integrals of the B-spline basis functions (Terzopoulos 1983; Bathe 2007).

In practice, it is more common to estimate a set of *shape priors* on the typical distribution of the control points $\{\boldsymbol{x}_k\}$ (Cootes, Cooper, Taylor *et al.* 1995). Consider the set of resistor shapes shown in Figure 5.4a. If we describe each contour with the set of control points shown in Figure 5.4b, we can plot the distribution of each point in a scatter plot, as shown in Figure 5.4c.

One potential way of describing this distribution would be by the location $\bar{\boldsymbol{x}}_k$ and 2D covariance $\boldsymbol{C}_k$ of each individual point $\boldsymbol{x}_k$. These could then be turned into a quadratic penalty (prior energy) on the point location,

$$E_{\text{loc}}(\boldsymbol{x}_k) = \frac{1}{2}(\boldsymbol{x}_k - \bar{\boldsymbol{x}}_k)^T \boldsymbol{C}_k^{-1}(\boldsymbol{x}_k - \bar{\boldsymbol{x}}_k). \tag{5.13}$$

In practice, however, the variation in point locations is usually highly correlated.

A preferable approach is to estimate the joint covariance of all the points simultaneously. First, concatenate all of the point locations $\{\boldsymbol{x}_k\}$ into a single vector $\boldsymbol{x}$, e.g., by interleaving the x and y locations of each point. The distribution of these vectors across all training

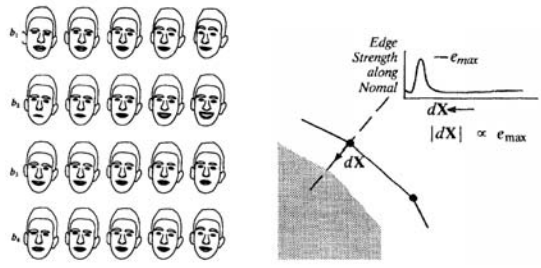

(a) (b)

Figure 5.5 Active Shape Model (ASM): (a) the effect of varying the first four shape parameters for a set of faces (Cootes, Taylor, Lanitis *et al.* 1993) © 1993 IEEE; (b) searching for the strongest gradient along the normal to each control point (Cootes, Cooper, Taylor *et al.* 1995) © 1995 Elsevier.

examples (Figure 5.4a) can be described with a mean $\bar{\boldsymbol{x}}$ and a covariance

$$\boldsymbol{C} = \frac{1}{P}\sum_p (\boldsymbol{x}_p - \bar{\boldsymbol{x}})(\boldsymbol{x}_p - \bar{\boldsymbol{x}})^T, \tag{5.14}$$

where $\boldsymbol{x}_p$ are the P training examples. Using *eigenvalue analysis* (Appendix A.1.2), which is also known as *Principal Component Analysis* (PCA) (Appendix B.1.1), the covariance matrix can be written as,

$$\boldsymbol{C} = \boldsymbol{\Phi}\ \mathrm{diag}(\lambda_0 \ldots \lambda_{K-1})\ \boldsymbol{\Phi}^T. \tag{5.15}$$

In most cases, the likely appearance of the points can be modeled using only a few eigenvectors with the largest eigenvalues. The resulting *point distribution model* (Cootes, Taylor, Lanitis *et al.* 1993; Cootes, Cooper, Taylor *et al.* 1995) can be written as

$$\boldsymbol{x} = \bar{\boldsymbol{x}} + \hat{\boldsymbol{\Phi}}\,\boldsymbol{b}, \tag{5.16}$$

where $\boldsymbol{b}$ is an $M \ll K$ element *shape parameter* vector and $\hat{\boldsymbol{\Phi}}$ are the first m columns of $\boldsymbol{\Phi}$. To constrain the shape parameters to reasonable values, we can use a quadratic penalty of the form

$$E_{\mathrm{shape}} = \frac{1}{2}\boldsymbol{b}^T\ \mathrm{diag}(\lambda_0 \ldots \lambda_{M-1})\ \boldsymbol{b} = \sum_m b_m^2/2\lambda_m. \tag{5.17}$$

Alternatively, the range of allowable b_m values can be limited to some range, e.g., $|b_m| \leq 3\sqrt{\lambda_m}$ (Cootes, Cooper, Taylor *et al.* 1995). Alternative approaches for deriving a set of shape vectors are reviewed by Isard and Blake (1998).

Varying the individual shape parameters b_m over the range $-2\sqrt{\lambda_m} \leq 2\sqrt{\lambda_m}$ can give a good indication of the expected variation in appearance, as shown in Figure 5.4d. Another example, this time related to face contours, is shown in Figure 5.5a.

In order to align a point distribution model with an image, each control point searches in a direction normal to the contour to find the most likely corresponding image edge point (Figure 5.5b). These individual measurements can be combined with priors on the shape parameters (and, if desired, position, scale, and orientation parameters) to estimate a new set of parameters. The resulting *Active Shape Model* (ASM) can be iteratively minimized to fit images to non-rigidly deforming objects such as medical images or body parts such as hands (Cootes, Cooper, Taylor *et al.* 1995). The ASM can also be combined with a PCA analysis of the underlying gray-level distribution to create an *Active Appearance Model* (AAM) (Cootes, Edwards, and Taylor 2001), which we discuss in more detail in Section 14.2.2.

5.1.2 Dynamic snakes and CONDENSATION

In many applications of active contours, the object of interest is being tracked from frame to frame as it deforms and evolves. In this case, it makes sense to use estimates from the previous frame to predict and constrain the new estimates.

One way to do this is to use Kalman filtering, which results in a formulation called *Kalman snakes* (Terzopoulos and Szeliski 1992; Blake, Curwen, and Zisserman 1993). The Kalman filter is based on a linear dynamic model of shape parameter evolution,

$$\boldsymbol{x}_t = \boldsymbol{A}\boldsymbol{x}_{t-1} + \boldsymbol{w}_t, \tag{5.18}$$

where $\boldsymbol{x}_t$ and $\boldsymbol{x}_{t-1}$ are the current and previous state variables, $\boldsymbol{A}$ is the linear *transition matrix*, and $\boldsymbol{w}$ is a noise (perturbation) vector, which is often modeled as a Gaussian (Gelb 1974). The matrices $\boldsymbol{A}$ and the noise covariance can be learned ahead of time by observing typical sequences of the object being tracked (Blake and Isard 1998).

The qualitative behavior of the Kalman filter can be seen in Figure 5.6a. The linear dynamic model causes a deterministic change (drift) in the previous estimate, while the process noise (perturbation) causes a stochastic diffusion that increases the system entropy (lack of certainty). New measurements from the current frame restore some of the certainty (peakedness) in the updated estimate.

In many situations, however, such as when tracking in clutter, a better estimate for the contour can be obtained if we remove the assumptions that the distribution are Gaussian, which is what the Kalman filter requires. In this case, a general multi-modal distribution is propagated, as shown in Figure 5.6b. In order to model such multi-modal distributions, Isard and Blake (1998) introduced the use of *particle filtering* to the computer vision community.[5]

[5] Alternatives to modeling multi-modal distributions include *mixtures of Gaussians* (Bishop 2006) and *multiple*

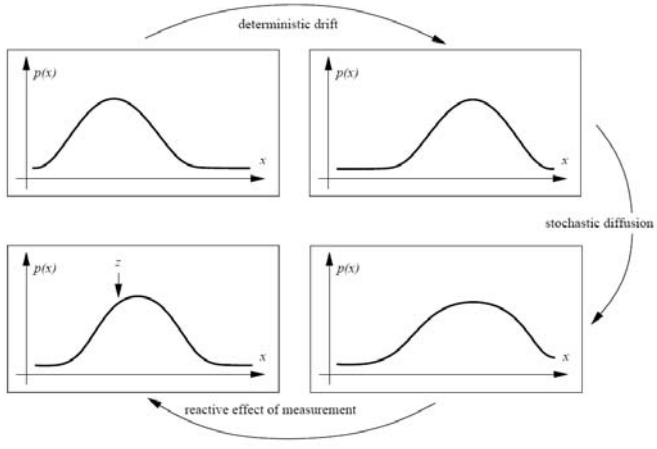

(a)

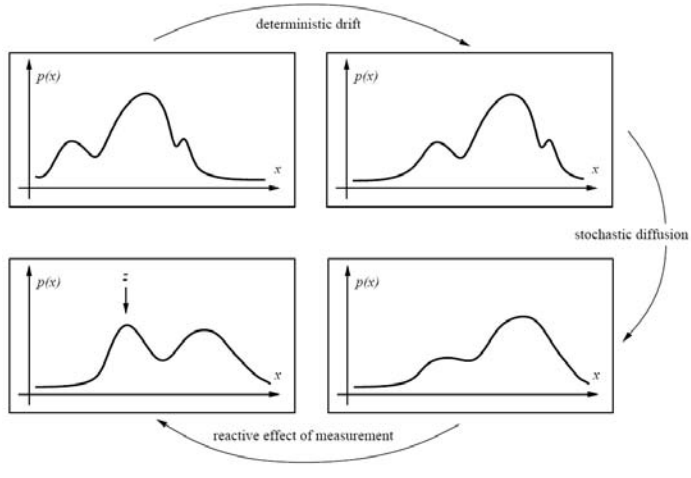

(b)

Figure 5.6 Probability density propagation (Isard and Blake 1998) © 1998 Springer. At the beginning of each estimation step, the probability density is updated according to the linear dynamic model (deterministic drift) and its certainty is reduced due to process noise (stochastic diffusion). New measurements introduce additional information that helps refine the current estimate. (a) The Kalman filter models the distributions as uni-modal, i.e., using a mean and covariance. (b) Some applications require more general multi-modal distributions.

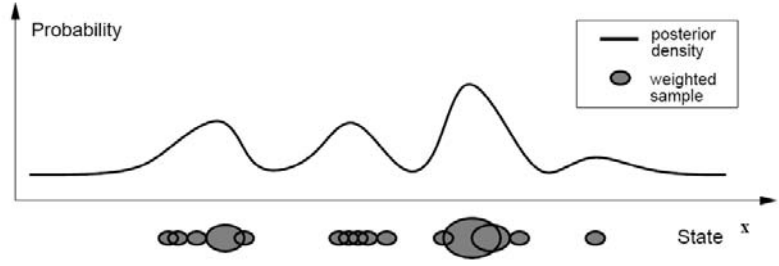

(a)

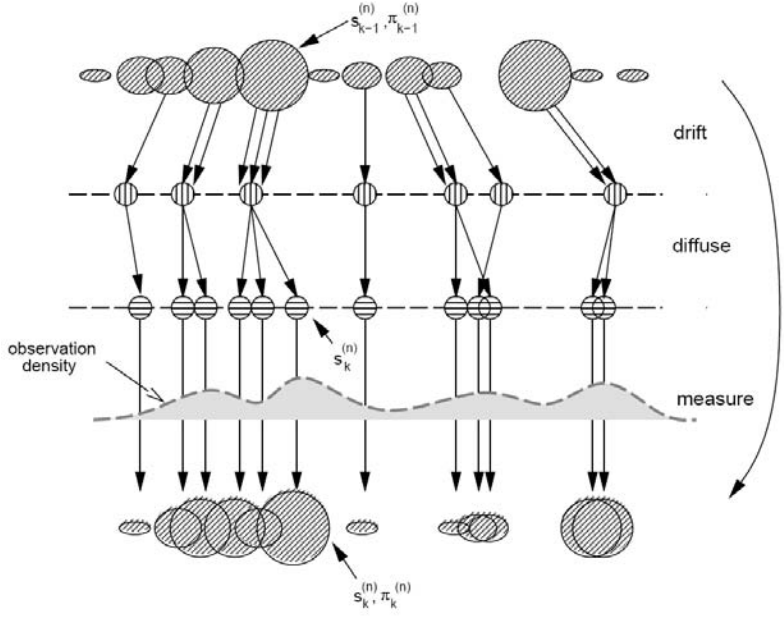

(b)

Figure 5.7 Factored sampling using particle filter in the CONDENSATION algorithm (Isard and Blake 1998) © 1998 Springer: (a) each density distribution is represented using a superposition of weighted *particles*; (b) the drift-diffusion-measurement cycle implemented using random sampling, perturbation, and re-weighting stages.

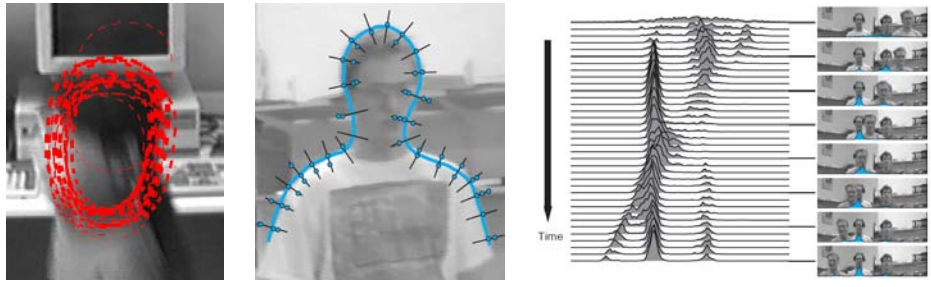

(a) (b) (c)

Figure 5.8 Head tracking using CONDENSATION (Isard and Blake 1998) © 1998 Springer: (a) sample set representation of head estimate distribution; (b) multiple measurements at each control vertex location; (c) multi-hypothesis tracking over time.

Particle filtering techniques represent a probability distribution using a collection of weighted point samples (Figure 5.7a) (Andrieu, de Freitas, Doucet *et al.* 2003; Bishop 2006; Koller and Friedman 2009). To update the locations of the samples according to the linear dynamics (deterministic drift), the centers of the samples are updated according to (5.18) and multiple samples are generated for each point (Figure 5.7b). These are then perturbed to account for the stochastic diffusion, i.e., their locations are moved by random vectors taken from the distribution of $\boldsymbol{w}$.[6] Finally, the weights of these samples are multiplied by the measurement probability density, i.e., we take each sample and measure its likelihood given the current (new) measurements. Because the point samples represent and propagate conditional estimates of the multi-modal density, Isard and Blake (1998) dubbed their algorithm CONditional DENSity propagATION or CONDENSATION.

Figure 5.8a shows what a factored sample of a head tracker might look like, drawing a red B-spline contour for each of (a subset of) the particles being tracked. Figure 5.8b shows why the measurement density itself is often multi-modal: the locations of the edges perpendicular to the spline curve can have multiple local maxima due to background clutter. Finally, Figure 5.8c shows the temporal evolution of the conditional density (x coordinate of the head and shoulder tracker centroid) as it tracks several people over time.

hypothesis tracking (Bar-Shalom and Fortmann 1988; Cham and Rehg 1999).

[6] Note that because of the structure of these steps, non-linear dynamics and non-Gaussian noise can be used.

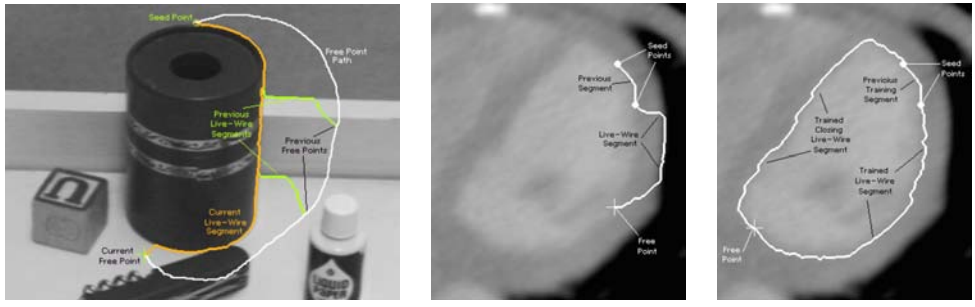

(a) (b) (c)

Figure 5.9 Intelligent scissors: (a) as the mouse traces the white path, the scissors follow the orange path along the object boundary (the green curves show intermediate positions) (Mortensen and Barrett 1995) © 1995 ACM; (b) regular scissors can sometimes jump to a stronger (incorrect) boundary; (c) after training to the previous segment, similar edge profiles are preferred (Mortensen and Barrett 1998) © 1995 Elsevier.

5.1.3 Scissors

Active contours allow a user to roughly specify a boundary of interest and have the system evolve the contour towards a more accurate location as well as track it over time. The results of this curve evolution, however, may be unpredictable and may require additional user-based hints to achieve the desired result.

An alternative approach is to have the system optimize the contour in real time as the user is drawing (Mortensen 1999). The *intelligent scissors* system developed by Mortensen and Barrett (1995) does just that. As the user draws a rough outline (the white curve in Figure 5.9a), the system computes and draws a better curve that clings to high-contrast edges (the orange curve).

To compute the optimal curve path (*live-wire*), the image is first pre-processed to associate low costs with edges (links between neighboring horizontal, vertical, and diagonal, i.e., $\mathcal{N}_8$ neighbors) that are likely to be boundary elements. Their system uses a combination of zero-crossing, gradient magnitudes, and gradient orientations to compute these costs.

Next, as the user traces a rough curve, the system continuously recomputes the lowest-cost path between the starting *seed point* and the current mouse location using Dijkstra's algorithm, a breadth-first dynamic programming algorithm that terminates at the current target location.

In order to keep the system from jumping around unpredictably, the system will "freeze" the curve to date (reset the seed point) after a period of inactivity. To prevent the live wire from jumping onto adjacent higher-contrast contours, the system also "learns" the intensity

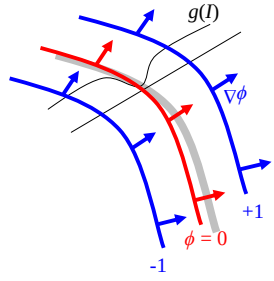

Figure 5.10 Level set evolution for a geodesic active contour. The embedding function ϕ is updated based on the curvature of the underlying surface modulated by the edge/speed function $g(I)$, as well as the gradient of $g(I)$, thereby attracting it to strong edges.

profile under the current optimized curve, and uses this to preferentially keep the wire moving along the same (or a similar looking) boundary (Figure 5.9b–c).

Several extensions have been proposed to the basic algorithm, which works remarkably well even in its original form. Mortensen and Barrett (1999) use *tobogganing*, which is a simple form of watershed region segmentation, to pre-segment the image into regions whose boundaries become candidates for optimized curve paths. The resulting region boundaries are turned into a much smaller graph, where nodes are located wherever three or four regions meet. The Dijkstra algorithm is then run on this reduced graph, resulting in much faster (and often more stable) performance. Another extension to intelligent scissors is to use a probabilistic framework that takes into account the current trajectory of the boundary, resulting in a system called JetStream (Pérez, Blake, and Gangnet 2001).

Instead of re-computing an optimal curve at each time instant, a simpler system can be developed by simply "snapping" the current mouse position to the nearest likely boundary point (Gleicher 1995). Applications of these boundary extraction techniques to image cutting and pasting are presented in Section 10.4.

5.1.4 Level Sets

A limitation of active contours based on parametric curves of the form $\boldsymbol{f}(s)$, e.g., snakes, B-snakes, and CONDENSATION, is that it is challenging to change the topology of the curve as it evolves. (McInerney and Terzopoulos (1999, 2000) describe one approach to doing this.) Furthermore, if the shape changes dramatically, curve reparameterization may also be required.

An alternative representation for such closed contours is to use a *level set*, where the *zero-crossing(s)* of a *characteristic* (or signed distance (Section 3.3.3)) function define the curve.

Level sets evolve to fit and track objects of interest by modifying the underlying *embedding function* (another name for this 2D function) $\phi(x, y)$ instead of the curve $\boldsymbol{f}(s)$ (Malladi, Sethian, and Vemuri 1995; Sethian 1999; Sapiro 2001; Osher and Paragios 2003). To reduce the amount of computation required, only a small strip (frontier) around the locations of the current zero-crossing needs to updated at each step, which results in what are called *fast marching methods* (Sethian 1999).

An example of an evolution equation is the *geodesic active contour* proposed by Caselles, Kimmel, and Sapiro (1997) and Yezzi, Kichenassamy, Kumar *et al.* (1997),

$$\begin{aligned} \frac{d\phi}{dt} &= |\nabla\phi| \mathrm{div}\left(g(I)\frac{\nabla\phi}{|\nabla\phi|}\right) \\ &= g(I)|\nabla\phi| \mathrm{div}\left(\frac{\nabla\phi}{|\nabla\phi|}\right) + \nabla g(I) \cdot \nabla\phi, \end{aligned} \tag{5.19}$$

where $g(I)$ is a generalized version of the snake edge potential (5.5). To get an intuitive sense of the curve's behavior, assume that the embedding function ϕ is a signed distance function away from the curve (Figure 5.10), in which case $|\phi| = 1$. The first term in Equation (5.19) moves the curve in the direction of its curvature, i.e., it acts to straighten the curve, under the influence of the modulation function $g(I)$. The second term moves the curve down the gradient of $g(I)$, encouraging the curve to migrate towards minima of $g(I)$.

While this level-set formulation can readily change topology, it is still susceptible to local minima, since it is based on local measurements such as image gradients. An alternative approach is to re-cast the problem in a segmentation framework, where the energy measures the consistency of the image statistics (e.g., color, texture, motion) inside and outside the segmented regions (Cremers, Rousson, and Deriche 2007; Rousson and Paragios 2008; Houhou, Thiran, and Bresson 2008). These approaches build on earlier energy-based segmentation frameworks introduced by Leclerc (1989), Mumford and Shah (1989), and Chan and Vese (1992), which are discussed in more detail in Section 5.5. Examples of such level-set segmentations are shown in Figure 5.11, which shows the evolution of the level sets from a series of distributed circles towards the final binary segmentation.

For more information on level sets and their applications, please see the collection of papers edited by Osher and Paragios (2003) as well as the series of Workshops on Variational and Level Set Methods in Computer Vision (Paragios, Faugeras, Chan *et al.* 2005) and Special Issues on Scale Space and Variational Methods in Computer Vision (Paragios and Sgallari 2009).

5.1.5 *Application*: Contour tracking and rotoscoping

Active contours can be used in a wide variety of object-tracking applications (Blake and Isard 1998; Yilmaz, Javed, and Shah 2006). For example, they can be used to track facial features

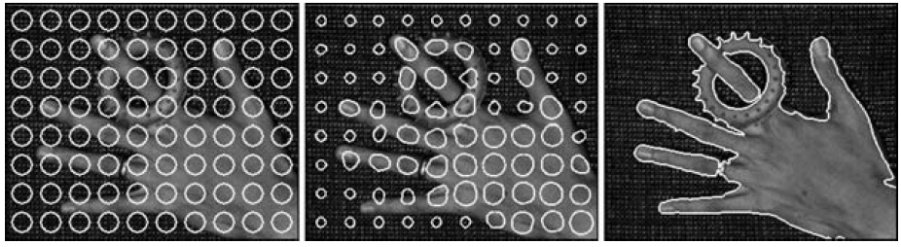

(a)

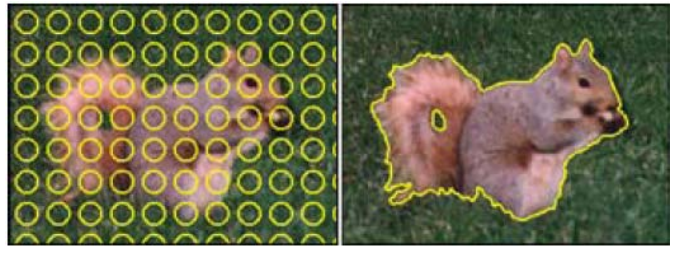

(b)

Figure 5.11 Level set segmentation (Cremers, Rousson, and Deriche 2007) © 2007 Springer: (a) grayscale image segmentation and (b) color image segmentation. Uni-variate and multi-variate Gaussians are used to model the foreground and background pixel distributions. The initial circles evolve towards an accurate segmentation of foreground and background, adapting their topology as they evolve.

for performance-driven animation (Terzopoulos and Waters 1990; Lee, Terzopoulos, and Waters 1995; Parke and Waters 1996; Bregler, Covell, and Slaney 1997) (Figure 5.2b). They can also be used to track heads and people, as shown in Figure 5.8, as well as moving vehicles (Paragios and Deriche 2000). Additional applications include medical image segmentation, where contours can be tracked from slice to slice in computerized tomography (3D medical imagery) (Cootes and Taylor 2001) or over time, as in ultrasound scans.

An interesting application that is closer to computer animation and visual effects is *rotoscoping*, which uses the tracked contours to deform a set of hand-drawn animations (or to modify or replace the original video frames).[7] Agarwala, Hertzmann, Seitz *et al.* (2004) present a system based on tracking hand-drawn B-spline contours drawn at selected keyframes, using a combination of geometric and appearance-based criteria (Figure 5.12). They also provide an excellent review of previous rotoscoping and image-based, contour-tracking systems.

[7] The term comes from a device (a rotoscope) that projected frames of a live-action film underneath an acetate so that artists could draw animations directly over the actors' shapes.

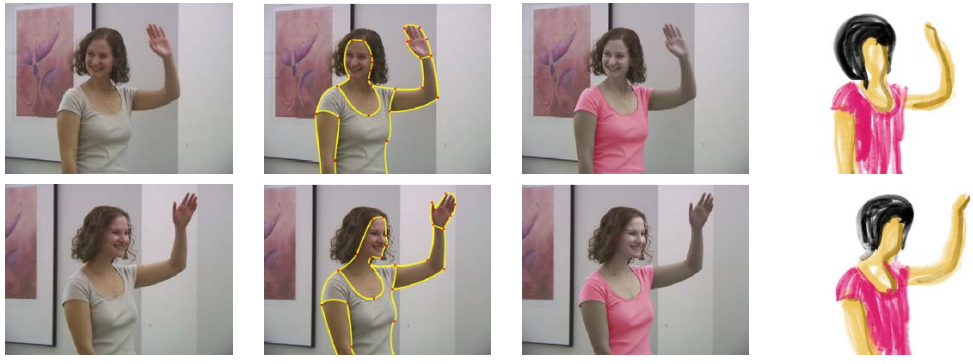

(a) (b) (c) (d)

Figure 5.12 Keyframe-based rotoscoping (Agarwala, Hertzmann, Seitz *et al.* 2004) © 2004 ACM: (a) original frames; (b) rotoscoped contours; (c) re-colored blouse; (d) rotoscoped hand-drawn animation.

Additional applications of rotoscoping (object contour detection and segmentation), such as cutting and pasting objects from one photograph into another, are presented in Section 10.4.

5.2 Split and merge

As mentioned in the introduction to this chapter, the simplest possible technique for segmenting a grayscale image is to select a threshold and then compute connected components (Section 3.3.2). Unfortunately, a single threshold is rarely sufficient for the whole image because of lighting and intra-object statistical variations.

In this section, we describe a number of algorithms that proceed either by recursively splitting the whole image into pieces based on region statistics or, conversely, merging pixels and regions together in a hierarchical fashion. It is also possible to combine both splitting and merging by starting with a medium-grain segmentation (in a quadtree representation) and then allowing both merging and splitting operations (Horowitz and Pavlidis 1976; Pavlidis and Liow 1990).

5.2.1 Watershed

A technique related to thresholding, since it operates on a grayscale image, is *watershed* computation (Vincent and Soille 1991). This technique segments an image into several *catchment basins*, which are the regions of an image (interpreted as a height field or landscape) where

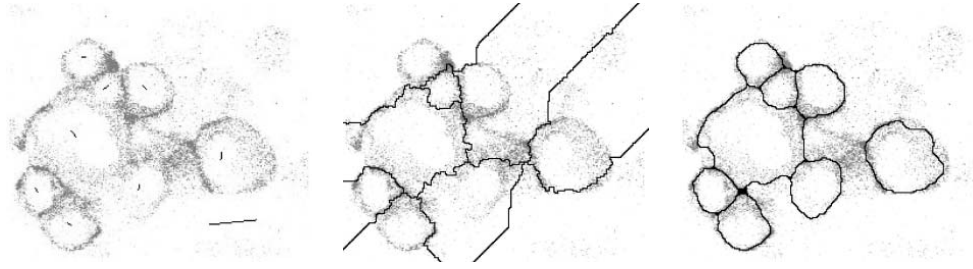

(a) (b) (c)

Figure 5.13 Locally constrained watershed segmentation (Beare 2006) © 2006 IEEE: (a) original confocal microscopy image with marked seeds (line segments); (b) standard watershed segmentation; (c) locally constrained watershed segmentation.

rain would flow into the same lake. An efficient way to compute such regions is to start flooding the landscape at all of the local minima and to label ridges wherever differently evolving components meet. The whole algorithm can be implemented using a priority queue of pixels and breadth-first search (Vincent and Soille 1991).[8]

Since images rarely have dark regions separated by lighter ridges, watershed segmentation is usually applied to a smoothed version of the gradient magnitude image, which also makes it usable with color images. As an alternative, the maximum oriented energy in a steerable filter (3.28–3.29) (Freeman and Adelson 1991) can be used as the basis of the *oriented watershed transform* developed by Arbeláez, Maire, Fowlkes *et al.* (2010). Such techniques end up finding smooth regions separated by visible (higher gradient) boundaries. Since such boundaries are what active contours usually follow, active contour algorithms (Mortensen and Barrett 1999; Li, Sun, Tang *et al.* 2004) often precompute such a segmentation using either the watershed or the related *tobogganing* technique (Section 5.1.3).

Unfortunately, watershed segmentation associates a unique region with each local minimum, which can lead to over-segmentation. Watershed segmentation is therefore often used as part of an interactive system, where the user first marks seed locations (with a click or a short stroke) that correspond to the centers of different desired components. Figure 5.13 shows the results of running the watershed algorithm with some manually placed markers on a confocal microscopy image. It also shows the result for an improved version of watershed that uses local morphology to smooth out and optimize the boundaries separating the regions (Beare 2006).

[8] A related algorithm can be used to compute maximally stable extremal regions (MSERs) efficiently (Section 4.1.1) (Nistér and Stewénius 2008).

5.2.2 Region splitting (divisive clustering)

Splitting the image into successively finer regions is one of the oldest techniques in computer vision. Ohlander, Price, and Reddy (1978) present such a technique, which first computes a histogram for the whole image and then finds a threshold that best separates the large peaks in the histogram. This process is repeated until regions are either fairly uniform or below a certain size.

More recent splitting algorithms often optimize some metric of intra-region similarity and inter-region dissimilarity. These are covered in Sections 5.4 and 5.5.

5.2.3 Region merging (agglomerative clustering)

Region merging techniques also date back to the beginnings of computer vision. Brice and Fennema (1970) use a dual grid for representing boundaries between pixels and merge regions based on their relative boundary lengths and the strength of the visible edges at these boundaries.

In data clustering, algorithms can link clusters together based on the distance between their closest points (single-link clustering), their farthest points (complete-link clustering), or something in between (Jain, Topchy, Law *et al.* 2004). Kamvar, Klein, and Manning (2002) provide a probabilistic interpretation of these algorithms and show how additional models can be incorporated within this framework.

A very simple version of pixel-based merging combines adjacent regions whose average color difference is below a threshold or whose regions are too small. Segmenting the image into such *superpixels* (Mori, Ren, Efros *et al.* 2004), which are not semantically meaningful, can be a useful pre-processing stage to make higher-level algorithms such as stereo matching (Zitnick, Kang, Uyttendaele *et al.* 2004; Taguchi, Wilburn, and Zitnick 2008), optic flow (Zitnick, Jojic, and Kang 2005; Brox, Bregler, and Malik 2009), and recognition (Mori, Ren, Efros *et al.* 2004; Mori 2005; Gu, Lim, Arbelaez *et al.* 2009; Lim, Arbeláez, Gu *et al.* 2009) both faster and more robust.

5.2.4 Graph-based segmentation

While many merging algorithms simply apply a fixed rule that groups pixels and regions together, Felzenszwalb and Huttenlocher (2004b) present a merging algorithm that uses *relative dissimilarities* between regions to determine which ones should be merged; it produces an algorithm that provably optimizes a global grouping metric. They start with a pixel-to-pixel dissimilarity measure $w(e)$ that measures, for example, intensity differences between $\mathcal{N}_8$ neighbors. (Alternatively, they can use the *joint feature space* distances (5.42) introduced by Comaniciu and Meer (2002), which we discuss in Section 5.3.2.)

(a) (b) (c)

Figure 5.14 Graph-based merging segmentation (Felzenszwalb and Huttenlocher 2004b) © 2004 Springer: (a) input grayscale image that is successfully segmented into three regions even though the variation inside the smaller rectangle is larger than the variation across the middle edge; (b) input grayscale image; (c) resulting segmentation using an $\mathcal{N}_8$ pixel neighborhood.

For any region R, its *internal difference* is defined as the largest edge weight in the region's minimum spanning tree,

$$Int(R) = \min_{e \in MST(R)} w(e). \tag{5.20}$$

For any two adjacent regions with at least one edge connecting their vertices, the difference between these regions is defined as the minimum weight edge connecting the two regions,

$$Dif(R_1, R_2) = \min_{e=(v_1,v_2)|v_1 \in R_1, v_2 \in R_2} w(e). \tag{5.21}$$

Their algorithm merges any two adjacent regions whose difference is smaller than the minimum internal difference of these two regions,

$$MInt(R_1, R_2) = \min(Int(R_1) + \tau(R_1), Int(R_2) + \tau(R_2)), \tag{5.22}$$

where $\tau(R)$ is a heuristic region penalty that Felzenszwalb and Huttenlocher (2004b) set to $k/|R|$, but which can be set to any application-specific measure of region goodness.

By merging regions in decreasing order of the edges separating them (which can be efficiently evaluated using a variant of Kruskal's minimum spanning tree algorithm), they provably produce segmentations that are neither too fine (there exist regions that could have been merged) nor too coarse (there are regions that could be split without being mergeable). For fixed-size pixel neighborhoods, the running time for this algorithm is $O(N \log N)$, where N is the number of image pixels, which makes it one of the fastest segmentation algorithms (Paris and Durand 2007). Figure 5.14 shows two examples of images segmented using their technique.

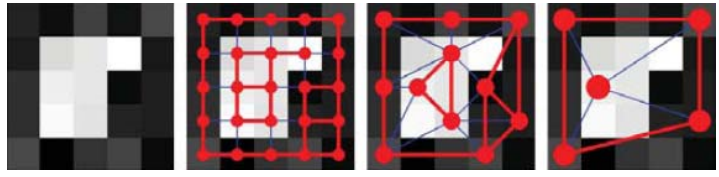

(a) (b) (c) (d)

Figure 5.15 Coarse to fine node aggregation in segmentation by weighted aggregation (SWA) (Sharon, Galun, Sharon *et al.* 2006) © 2006 Macmillan Publishers Ltd [Nature]: (a) original gray-level pixel grid; (b) inter-pixel couplings, where thicker lines indicate stronger couplings; (c) after one level of coarsening, where each original pixel is strongly coupled to one of the coarse-level nodes; (d) after two levels of coarsening.

5.2.5 Probabilistic aggregation

Alpert, Galun, Basri *et al.* (2007) develop a probabilistic merging algorithm based on two cues, namely gray-level similarity and texture similarity. The gray-level similarity between regions R_i and R_j is based on the *minimal external difference* from other neighboring regions,

$$\sigma^+_{local} = \min(\Delta^+_i, \Delta^+_j), \tag{5.23}$$

where $\Delta^+_i = \min_k |\Delta_{ik}|$ and Δ_{ik} is the difference in average intensities between regions R_i and R_k. This is compared to the *average intensity difference*,

$$\sigma^-_{local} = \frac{\Delta^-_i + \Delta^-_j}{2}, \tag{5.24}$$

where $\Delta^-_i = \sum_k(\tau_{ik}\Delta_{ik}) / \sum_k(\tau_{ik})$ and τ_{ik} is the boundary length between regions R_i and R_k. The texture similarity is defined using relative differences between histogram bins of simple oriented Sobel filter responses. The pairwise statistics σ^+_{local} and σ^-_{local} are used to compute the likelihoods p_{ij} that two regions should be merged. (See the paper by Alpert, Galun, Basri *et al.* (2007) for more details.)

Merging proceeds in a hierarchical fashion inspired by algebraic multigrid techniques (Brandt 1986; Briggs, Henson, and McCormick 2000) and previously used by Alpert, Galun, Basri *et al.* (2007) in their segmentation by weighted aggregation (SWA) algorithm (Sharon, Galun, Sharon *et al.* 2006), which we discuss in Section 5.4. A subset of the nodes $C \subset V$ that are (collectively) *strongly coupled* to all of the original nodes (regions) are used to define the problem at a coarser scale (Figure 5.15), where strong coupling is defined as

$$\frac{\sum_{j \in C} p_{ij}}{\sum_{j \in V} p_{ij}} > \phi, \tag{5.25}$$

with ϕ usually set to 0.2. The intensity and texture similarity statistics for the coarser nodes are recursively computed using weighted averaging, where the relative strengths (couplings) between coarse- and fine-level nodes are based on their merge probabilities p_{ij}. This allows the algorithm to run in essentially $O(N)$ time, using the same kind of hierarchical aggregation operations that are used in pyramid-based filtering or preconditioning algorithms. After a segmentation has been identified at a coarser level, the exact memberships of each pixel are computed by propagating coarse-level assignments to their finer-level "children" (Sharon, Galun, Sharon *et al.* 2006; Alpert, Galun, Basri *et al.* 2007). Figure 5.22 shows the segmentations produced by this algorithm compared to other popular segmentation algorithms.

5.3 Mean shift and mode finding

Mean-shift and mode finding techniques, such as k-means and mixtures of Gaussians, model the feature vectors associated with each pixel (e.g., color and position) as samples from an unknown probability density function and then try to find clusters (modes) in this distribution.

Consider the color image shown in Figure 5.16a. How would you segment this image based on color alone? Figure 5.16b shows the distribution of pixels in L*u*v* space, which is equivalent to what a vision algorithm that ignores spatial location would see. To make the visualization simpler, let us only consider the L*u* coordinates, as shown in Figure 5.16c. How many obvious (elongated) clusters do you see? How would you go about finding these clusters?

The k-means and mixtures of Gaussians techniques use a *parametric* model of the density function to answer this question, i.e., they assume the density is the superposition of a small number of simpler distributions (e.g., Gaussians) whose locations (centers) and shape (covariance) can be estimated. Mean shift, on the other hand, smoothes the distribution and finds its peaks as well as the regions of feature space that correspond to each peak. Since a complete density is being modeled, this approach is called *non-parametric* (Bishop 2006). Let us look at these techniques in more detail.

5.3.1 K-means and mixtures of Gaussians

While k-means implicitly models the probability density as a superposition of spherically symmetric distributions, it does not require any probabilistic reasoning or modeling (Bishop 2006). Instead, the algorithm is given the number of clusters k it is supposed to find; it then iteratively updates the cluster center location based on the samples that are closest to each center. The algorithm can be initialized by randomly sampling k centers from the input feature vectors. Techniques have also been developed for splitting or merging cluster centers

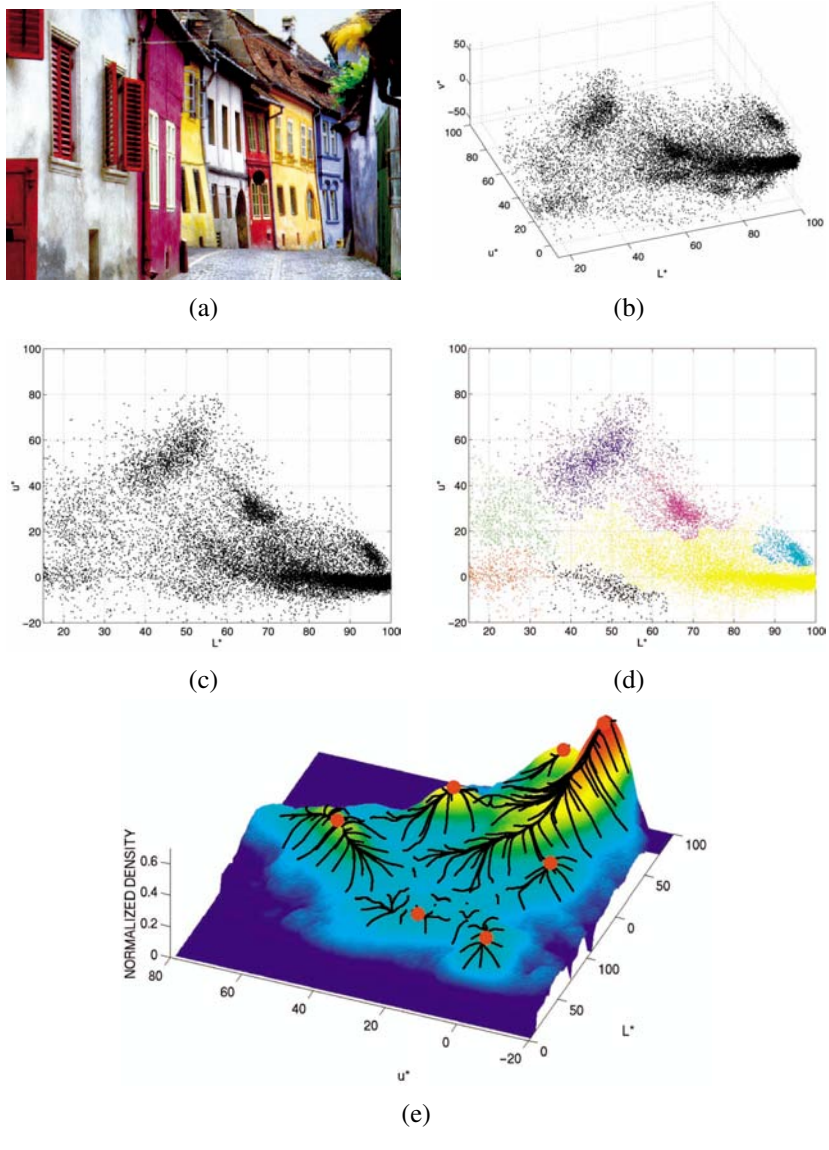

Figure 5.16 Mean-shift image segmentation (Comaniciu and Meer 2002) © 2002 IEEE: (a) input color image; (b) pixels plotted in L*u*v* space; (c) L*u* space distribution; (d) clustered results after 159 mean-shift procedures; (e) corresponding trajectories with peaks marked as red dots.

based on their statistics, and for accelerating the process of finding the nearest mean center (Bishop 2006).

In mixtures of Gaussians, each cluster center is augmented by a covariance matrix whose values are re-estimated from the corresponding samples. Instead of using nearest neighbors to associate input samples with cluster centers, a *Mahalanobis distance* (Appendix B.1.1) is used:

$$d(\boldsymbol{x}_i, \boldsymbol{\mu}_k; \boldsymbol{\Sigma}_k) = \|\boldsymbol{x}_i - \boldsymbol{\mu}_k\|_{\boldsymbol{\Sigma}_k^{-1}} = (\boldsymbol{x}_i - \boldsymbol{\mu}_k)^T \boldsymbol{\Sigma}_k^{-1} (\boldsymbol{x}_i - \boldsymbol{\mu}_k) \tag{5.26}$$

where $\boldsymbol{x}_i$ are the input samples, $\boldsymbol{\mu}_k$ are the cluster centers, and $\boldsymbol{\Sigma}_k$ are their covariance estimates. Samples can be associated with the nearest cluster center (a *hard assignment* of membership) or can be *softly assigned* to several nearby clusters.

This latter, more commonly used, approach corresponds to iteratively re-estimating the parameters for a mixture of Gaussians density function,

$$p(\boldsymbol{x}|\{\pi_k, \boldsymbol{\mu}_k, \boldsymbol{\Sigma}_k\}) = \sum_k \pi_k \mathcal{N}(\boldsymbol{x}|\boldsymbol{\mu}_k, \boldsymbol{\Sigma}_k), \tag{5.27}$$

where π_k are the *mixing coefficients*, $\boldsymbol{\mu}_k$ and $\boldsymbol{\Sigma}_k$ are the Gaussian means and covariances, and

$$\mathcal{N}(\boldsymbol{x}|\boldsymbol{\mu}_k, \boldsymbol{\Sigma}_k) = \frac{1}{|\boldsymbol{\Sigma}_k|} e^{-d(\boldsymbol{x}, \boldsymbol{\mu}_k; \boldsymbol{\Sigma}_k)} \tag{5.28}$$

is the *normal* (Gaussian) distribution (Bishop 2006).

To iteratively compute (a local) maximum likely estimate for the unknown mixture parameters $\{\pi_k, \boldsymbol{\mu}_k, \boldsymbol{\Sigma}_k\}$, the *expectation maximization* (EM) algorithm (Dempster, Laird, and Rubin 1977) proceeds in two alternating stages:

1. The *expectation* stage (E step) estimates the *responsibilities*

$$z_{ik} = \frac{1}{Z_i} \pi_k \mathcal{N}(\boldsymbol{x}|\boldsymbol{\mu}_k, \boldsymbol{\Sigma}_k) \quad \text{with} \quad \sum_k z_{ik} = 1, \tag{5.29}$$

   which are the estimates of how likely a sample $\boldsymbol{x}_i$ was generated from the kth Gaussian cluster.

2. The *maximization* stage (M step) updates the parameter values

$$\boldsymbol{\mu}_k = \frac{1}{N_k} \sum_i z_{ik} \boldsymbol{x}_i, \tag{5.30}$$

$$\boldsymbol{\Sigma}_k = \frac{1}{N_k} \sum_i z_{ik} (\boldsymbol{x}_i - \boldsymbol{\mu}_k)(\boldsymbol{x}_i - \boldsymbol{\mu}_k)^T, \tag{5.31}$$

$$\pi_k = \frac{N_k}{N}, \tag{5.32}$$

where

$$N_k = \sum_i z_{ik}. \tag{5.33}$$

is an estimate of the number of sample points assigned to each cluster.

Bishop (2006) has a wonderful exposition of both mixture of Gaussians estimation and the more general topic of expectation maximization.

In the context of image segmentation, Ma, Derksen, Hong *et al.* (2007) present a nice review of segmentation using mixtures of Gaussians and develop their own extension based on Minimum Description Length (MDL) coding, which they show produces good results on the Berkeley segmentation database.

5.3.2 Mean shift

While k-means and mixtures of Gaussians use a parametric form to model the probability density function being segmented, mean shift implicitly models this distribution using a smooth continuous *non-parametric model*. The key to mean shift is a technique for efficiently finding peaks in this high-dimensional data distribution without ever computing the complete function explicitly (Fukunaga and Hostetler 1975; Cheng 1995; Comaniciu and Meer 2002).

Consider once again the data points shown in Figure 5.16c, which can be thought of as having been drawn from some probability density function. If we could compute this density function, as visualized in Figure 5.16e, we could find its major peaks (*modes*) and identify regions of the input space that climb to the same peak as being part of the same region. This is the inverse of the *watershed* algorithm described in Section 5.2.1, which climbs downhill to find *basins of attraction*.

The first question, then, is how to estimate the density function given a sparse set of samples. One of the simplest approaches is to just smooth the data, e.g., by convolving it with a fixed kernel of width h,

$$f(\boldsymbol{x}) = \sum_i K(\boldsymbol{x} - \boldsymbol{x}_i) = \sum_i k\left(\frac{\|\boldsymbol{x} - \boldsymbol{x}_i\|^2}{h^2}\right), \tag{5.34}$$

where $\boldsymbol{x}_i$ are the input samples and $k(r)$ is the kernel function (or *Parzen window*).[9] This approach is known as *kernel density estimation* or the *Parzen window technique* (Duda, Hart, and Stork 2001, Section 4.3; Bishop 2006, Section 2.5.1). Once we have computed $f(\boldsymbol{x})$, as shown in Figures 5.16e and 5.17, we can find its local maxima using gradient ascent or some other optimization technique.

[9] In this simplified formula, a Euclidean metric is used. We discuss a little later (5.42) how to generalize this to non-uniform (scaled or oriented) metrics. Note also that this distribution may not be *proper*, i.e., integrate to 1. Since we are looking for maxima in the density, this does not matter.

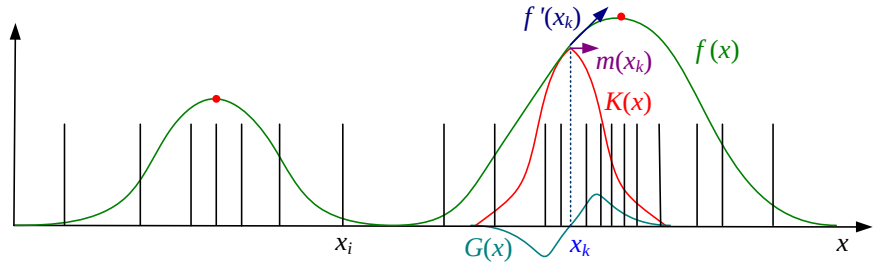

Figure 5.17 One-dimensional visualization of the kernel density estimate, its derivative, and a mean shift. The kernel density estimate $f(x)$ is obtained by convolving the sparse set of input samples x_i with the kernel function $K(x)$. The derivative of this function, $f'(x)$, can be obtained by convolving the inputs with the derivative kernel $G(x)$. Estimating the local displacement vectors around a current estimate x_k results in the mean-shift vector $m(x_k)$, which, in a multi-dimensional setting, point in the same direction as the function gradient $\nabla f(\boldsymbol{x}_k)$. The red dots indicate local maxima in $f(x)$ to which the mean shifts converge.

The problem with this "brute force" approach is that, for higher dimensions, it becomes computationally prohibitive to evaluate $f(\boldsymbol{x})$ over the complete search space.[10] Instead, mean shift uses a variant of what is known in the optimization literature as *multiple restart gradient descent*. Starting at some guess for a local maximum, $\boldsymbol{y}_k$, which can be a random input data point $\boldsymbol{x}_i$, mean shift computes the gradient of the density estimate $f(\boldsymbol{x})$ at $\boldsymbol{y}_k$ and takes an uphill step in that direction (Figure 5.17). The gradient of $f(\boldsymbol{x})$ is given by

$$\nabla f(\boldsymbol{x}) = \sum_i (\boldsymbol{x}_i - \boldsymbol{x}) G(\boldsymbol{x} - \boldsymbol{x}_i) = \sum_i (\boldsymbol{x}_i - \boldsymbol{x}) g\left(\frac{\|\boldsymbol{x} - \boldsymbol{x}_i\|^2}{h^2}\right), \tag{5.35}$$

where

$$g(r) = -k'(r), \tag{5.36}$$

and $k'(r)$ is the first derivative of $k(r)$. We can re-write the gradient of the density function as

$$\nabla f(\boldsymbol{x}) = \left[\sum_i G(\boldsymbol{x} - \boldsymbol{x}_i)\right] \boldsymbol{m}(\boldsymbol{x}), \tag{5.37}$$

where the vector

$$\boldsymbol{m}(\boldsymbol{x}) = \frac{\sum_i \boldsymbol{x}_i G(\boldsymbol{x} - \boldsymbol{x}_i)}{\sum_i G(\boldsymbol{x} - \boldsymbol{x}_i)} - \boldsymbol{x} \tag{5.38}$$

is called the *mean shift*, since it is the difference between the weighted mean of the neighbors $\boldsymbol{x}_i$ around $\boldsymbol{x}$ and the current value of $\boldsymbol{x}$.

[10] Even for one dimension, if the space is extremely sparse, it may be inefficient.

In the mean-shift procedure, the current estimate of the mode $\boldsymbol{y}_k$ at iteration k is replaced by its locally weighted mean,

$$\boldsymbol{y}_{k+1} = \boldsymbol{y}_k + \boldsymbol{m}(\boldsymbol{y}_k) = \frac{\sum_i \boldsymbol{x}_i G(\boldsymbol{y}_k - \boldsymbol{x}_i)}{\sum_i G(\boldsymbol{y}_k - \boldsymbol{x}_i)}. \tag{5.39}$$

Comaniciu and Meer (2002) prove that this algorithm converges to a local maximum of $f(\boldsymbol{x})$ under reasonably weak conditions on the kernel $k(r)$, i.e., that it is monotonically decreasing. This convergence is not guaranteed for regular gradient descent unless appropriate step size control is used.

The two kernels that Comaniciu and Meer (2002) studied are the Epanechnikov kernel,

$$k_E(r) = \max(0, 1 - r), \tag{5.40}$$

which is a radial generalization of a bilinear kernel, and the Gaussian (normal) kernel,

$$k_N(r) = \exp\left(-\frac{1}{2}r\right). \tag{5.41}$$

The corresponding derivative kernels $g(r)$ are a unit ball and another Gaussian, respectively. Using the Epanechnikov kernel converges in a finite number of steps, while the Gaussian kernel has a smoother trajectory (and produces better results), but converges very slowly near a mode (Exercise 5.5).

The simplest way to apply mean shift is to start a separate mean-shift mode estimate $\boldsymbol{y}$ at every input point $\boldsymbol{x}_i$ and to iterate for a fixed number of steps or until the mean-shift magnitude is below a threshold. A faster approach is to randomly subsample the input points $\boldsymbol{x}_i$ and to keep track of each point's temporal evolution. The remaining points can then be classified based on the nearest evolution path (Comaniciu and Meer 2002). Paris and Durand (2007) review a number of other more efficient implementations of mean shift, including their own approach, which is based on using an efficient low-resolution estimate of the complete multi-dimensional space of $f(\boldsymbol{x})$ along with its stationary points.

The color-based segmentation shown in Figure 5.16 only looks at pixel colors when determining the best clustering. It may therefore cluster together small isolated pixels that happen to have the same color, which may not correspond to a semantically meaningful segmentation of the image.

Better results can usually be obtained by clustering in the *joint domain* of color and location. In this approach, the spatial coordinates of the image $\boldsymbol{x}_s = (x, y)$, which are called the *spatial domain*, are concatenated with the color values $\boldsymbol{x}_r$, which are known as the *range domain*, and mean-shift clustering is applied in this five-dimensional space $\boldsymbol{x}_j$. Since location and color may have different scales, the kernels are adjusted accordingly, i.e., we use a kernel of the form

$$K(\boldsymbol{x}_j) = k\left(\frac{\|\boldsymbol{x}_r\|^2}{h_r^2}\right) k\left(\frac{\|\boldsymbol{x}_s\|^2}{h_s^2}\right), \tag{5.42}$$

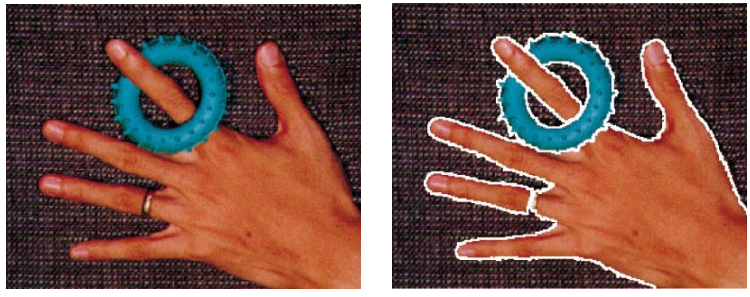

Figure 5.18 Mean-shift color image segmentation with parameters $(h_s, h_r, M) = (16, 19, 40)$ (Comaniciu and Meer 2002) © 2002 IEEE.

where separate parameters h_s and h_r are used to control the spatial and range bandwidths of the filter kernels. Figure 5.18 shows an example of mean-shift clustering in the joint domain, with parameters $(h_s, h_r, M) = (16, 19, 40)$, where spatial regions containing less than M pixels are eliminated.

The form of the joint domain filter kernel (5.42) is reminiscent of the bilateral filter kernel (3.34–3.37) discussed in Section 3.3.1. The difference between mean shift and bilateral filtering, however, is that in mean shift the spatial coordinates of each pixel are adjusted along with its color values, so that the pixel migrates more quickly towards other pixels with similar colors, and can therefore later be used for clustering and segmentation.

Determining the best bandwidth parameters h to use with mean shift remains something of an art, although a number of approaches have been explored. These include optimizing the bias–variance tradeoff, looking for parameter ranges where the number of clusters varies slowly, optimizing some external clustering criterion, or using top-down (application domain) knowledge (Comaniciu and Meer 2003). It is also possible to change the orientation of the kernel in joint parameter space for applications such as spatio-temporal (video) segmentations (Wang, Thiesson, Xu *et al.* 2004).

Mean shift has been applied to a number of different problems in computer vision, including face tracking, 2D shape extraction, and texture segmentation (Comaniciu and Meer 2002), and more recently in stereo matching (Chapter 11) (Wei and Quan 2004), non-photorealistic rendering (Section 10.5.2) (DeCarlo and Santella 2002), and video editing (Section 10.4.5) (Wang, Bhat, Colburn *et al.* 2005). Paris and Durand (2007) provide a nice review of such applications, as well as techniques for more efficiently solving the mean-shift equations and producing hierarchical segmentations.

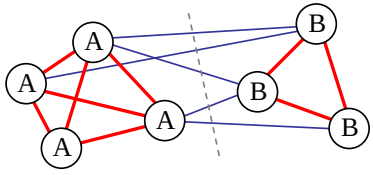

(a)

	A	B	sum
A	$assoc(A, A)$	$cut(A, B)$	$assoc(A, V)$
B	$cut(B, A)$	$assoc(B, B)$	$assoc(B, V)$
sum	$assoc(A, V)$	$assoc(B, v)$	

(b)

Figure 5.19 Sample weighted graph and its normalized cut: (a) a small sample graph and its smallest normalized cut; (b) tabular form of the associations and cuts for this graph. The $assoc$ and cut entries are computed as area sums of the associated weight matrix $\boldsymbol{W}$ (Figure 5.20). Normalizing the table entries by the row or column sums produces normalized associations and cuts $Nassoc$ and $Ncut$.

5.4 Normalized cuts

While bottom-up merging techniques aggregate regions into coherent wholes and mean-shift techniques try to find clusters of similar pixels using mode finding, the normalized cuts technique introduced by Shi and Malik (2000) examines the *affinities* (similarities) between nearby pixels and tries to separate groups that are connected by weak affinities.

Consider the simple graph shown in Figure 5.19a. The pixels in group A are all strongly connected with high affinities, shown as thick red lines, as are the pixels in group B. The connections between these two groups, shown as thinner blue lines, are much weaker. A *normalized cut* between the two groups, shown as a dashed line, separates them into two clusters.

The cut between two groups A and B is defined as the sum of all the weights being cut,

$$cut(A, B) = \sum_{i \in A, j \in B} w_{ij}, \tag{5.43}$$

where the weights between two pixels (or regions) i and j measure their similarity. Using a minimum cut as a segmentation criterion, however, does not result in reasonable clusters, since the smallest cuts usually involve isolating a single pixel.

A better measure of segmentation is the normalized cut, which is defined as

$$Ncut(A, B) = \frac{cut(A, B)}{assoc(A, V)} + \frac{cut(A, B)}{assoc(B, V)}, \tag{5.44}$$

where $assoc(A, A) = \sum_{i \in A, j \in A} w_{ij}$ is the *association* (sum of all the weights) within a cluster and $assoc(A, V) = assoc(A, A) + cut(A, B)$ is the sum of *all* the weights associated

with nodes in A. Figure 5.19b shows how the cuts and associations can be thought of as area sums in the weight matrix $\boldsymbol{W} = [w_{ij}]$, where the entries of the matrix have been arranged so that the nodes in A come first and the nodes in B come second. Figure 5.20 shows an actual weight matrix for which these area sums can be computed. Dividing each of these areas by the corresponding row sum (the rightmost column of Figure 5.19b) results in the normalized cut and association values. These normalized values better reflect the fitness of a particular segmentation, since they look for collections of edges that are weak relative to all of the edges both inside and emanating from a particular region.

Unfortunately, computing the optimal normalized cut is NP-complete. Instead, Shi and Malik (2000) suggest computing a real-valued assignment of nodes to groups. Let $\boldsymbol{x}$ be the *indicator vector* where $x_i = +1$ iff $i \in A$ and $x_i = -1$ iff $i \in B$. Let $\boldsymbol{d} = \boldsymbol{W}\boldsymbol{1}$ be the row sums of the symmetric matrix $\boldsymbol{W}$ and $\boldsymbol{D} = \mathrm{diag}(\boldsymbol{d})$ be the corresponding diagonal matrix. Shi and Malik (2000) show that minimizing the normalized cut over all possible indicator vectors $\boldsymbol{x}$ is equivalent to minimizing

$$\min_{\boldsymbol{y}} \frac{\boldsymbol{y}^T(\boldsymbol{D}-\boldsymbol{W})\boldsymbol{y}}{\boldsymbol{y}^T\boldsymbol{D}\boldsymbol{y}}, \tag{5.45}$$

where $\boldsymbol{y} = ((\boldsymbol{1}+\boldsymbol{x})-b(\boldsymbol{1}-\boldsymbol{x}))/2$ is a vector consisting of all 1s and $-b$s such that $\boldsymbol{y}\cdot\boldsymbol{d} = 0$. Minimizing this *Rayleigh quotient* is equivalent to solving the generalized eigenvalue system

$$(\boldsymbol{D}-\boldsymbol{W})\boldsymbol{y} = \lambda\boldsymbol{D}\boldsymbol{y}, \tag{5.46}$$

which can be turned into a regular eigenvalue problem

$$(\boldsymbol{I}-\boldsymbol{N})\boldsymbol{z} = \lambda\boldsymbol{z}, \tag{5.47}$$

where $\boldsymbol{N} = \boldsymbol{D}^{-1/2}\boldsymbol{W}\boldsymbol{D}^{-1/2}$ is the *normalized* affinity matrix (Weiss 1999) and $\boldsymbol{z} = \boldsymbol{D}^{1/2}\boldsymbol{y}$. Because these eigenvectors can be interpreted as the large modes of vibration in a spring-mass system, normalized cuts is an example of a *spectral method* for image segmentation.

Extending an idea originally proposed by Scott and Longuet-Higgins (1990), Weiss (1999) suggests normalizing the affinity matrix and then using the top k eigenvectors to reconstitute a $\boldsymbol{Q}$ matrix. Other papers have extended the basic normalized cuts framework by modifying the affinity matrix in different ways, finding better discrete solutions to the minimization problem, or applying multi-scale techniques (Meilă and Shi 2000, 2001; Ng, Jordan, and Weiss 2001; Yu and Shi 2003; Cour, Bénézit, and Shi 2005; Tolliver and Miller 2006).

Figure 5.20b shows the second smallest (real-valued) eigenvector corresponding to the weight matrix shown in Figure 5.20a. (Here, the rows have been permuted to separate the two groups of variables that belong to the different components of this eigenvector.) After this real-valued vector is computed, the variables corresponding to positive and negative

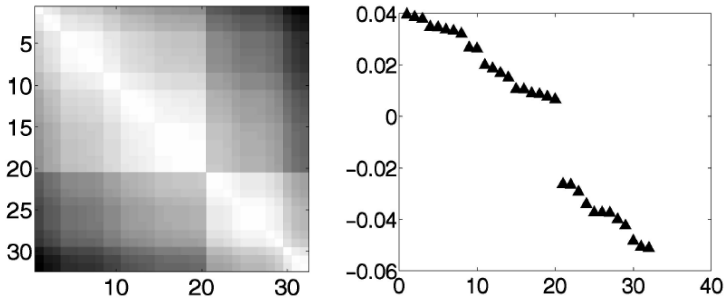

Figure 5.20 Sample weight table and its second smallest eigenvector (Shi and Malik 2000) © 2000 IEEE: (a) sample 32×32 weight matrix $\boldsymbol{W}$; (b) eigenvector corresponding to the second smallest eigenvalue of the generalized eigenvalue problem $(\boldsymbol{D} - \boldsymbol{W})\boldsymbol{y} = \lambda \boldsymbol{D}\boldsymbol{y}$.

eigenvector values are associated with the two cut components. This process can be further repeated to hierarchically subdivide an image, as shown in Figure 5.21.

The original algorithm proposed by Shi and Malik (2000) used spatial position and image feature differences to compute the pixel-wise affinities,

$$w_{ij} = \exp\left(-\frac{\|\boldsymbol{F}_i - \boldsymbol{F}_j\|^2}{\sigma_F^2} - \frac{\|\boldsymbol{x}_i - \boldsymbol{x}_j\|^2}{\sigma_s^2}\right), \tag{5.48}$$

for pixels within a radius $\|\boldsymbol{x}_i - \boldsymbol{x}_j\| < r$, where $\boldsymbol{F}$ is a feature vector that consists of intensities, colors, or oriented filter histograms. (Note how (5.48) is the negative exponential of the joint feature space distance (5.42).)

In subsequent work, Malik, Belongie, Leung *et al.* (2001) look for *intervening contours* between pixels i and j and define an intervening contour weight

$$w_{ij}^{IC} = 1 - \max_{\boldsymbol{x} \in l_{ij}} p_{con}(\boldsymbol{x}), \tag{5.49}$$

where l_{ij} is the image line joining pixels i and j and $p_{con}(\boldsymbol{x})$ is the probability of an intervening contour perpendicular to this line, which is defined as the negative exponential of the oriented energy in the perpendicular direction. They multiply these weights with a texton-based texture similarity metric and use an initial over-segmentation based purely on local pixel-wise features to re-estimate intervening contours and texture statistics in a region-based manner. Figure 5.22 shows the results of running this improved algorithm on a number of test images.

Because it requires the solution of large sparse eigenvalue problems, normalized cuts can be quite slow. Sharon, Galun, Sharon *et al.* (2006) present a way to accelerate the computation of the normalized cuts using an approach inspired by algebraic multigrid (Brandt

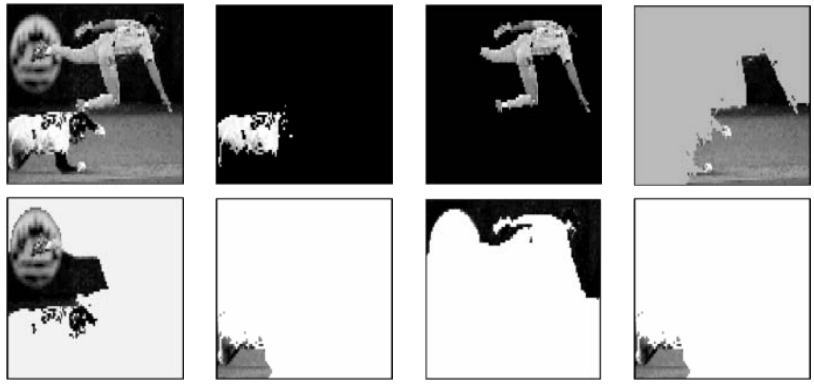

Figure 5.21 Normalized cuts segmentation (Shi and Malik 2000) © 2000 IEEE: The input image and the components returned by the normalized cuts algorithm.

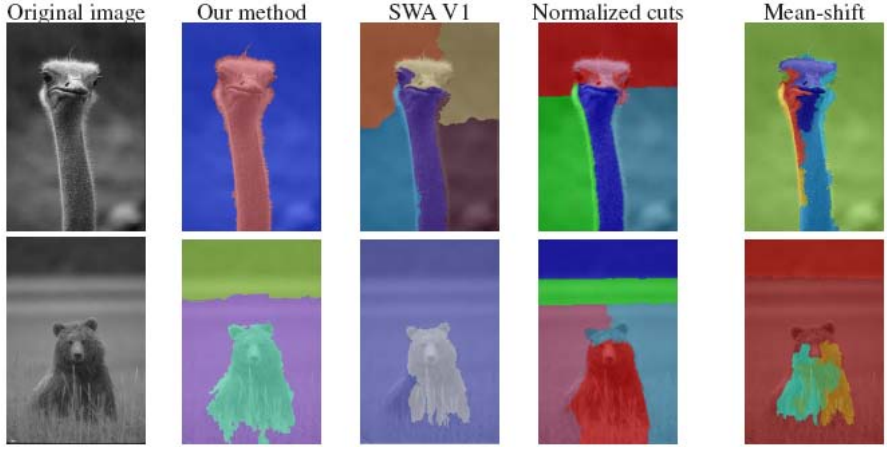

Figure 5.22 Comparative segmentation results (Alpert, Galun, Basri *et al.* 2007) © 2007 IEEE. "Our method" refers to the probabilistic bottom-up merging algorithm developed by Alpert *et al*.

1986; Briggs, Henson, and McCormick 2000). To coarsen the original problem, they select a smaller number of variables such that the remaining fine-level variables are *strongly coupled* to at least one coarse-level variable. Figure 5.15 shows this process schematically, while (5.25) gives the definition for strong coupling except that, in this case, the original weights w_{ij} in the normalized cut are used instead of merge probabilities p_{ij}.

Once a set of coarse variables has been selected, an inter-level interpolation matrix with elements similar to the left hand side of (5.25) is used to define a reduced version of the normalized cuts problem. In addition to computing the weight matrix using interpolation-based coarsening, additional region statistics are used to modulate the weights. After a normalized cut has been computed at the coarsest level of analysis, the membership values of finer-level nodes are computed by interpolating parent values and mapping values within $\epsilon = 0.1$ of 0 and 1 to pure Boolean values.

An example of the segmentation produced by weighted aggregation (SWA) is shown in Figure 5.22, along with the most recent probabilistic bottom-up merging algorithm by Alpert, Galun, Basri *et al.* (2007), which was described in Section 5.2. In even more recent work, Wang and Oliensis (2010) show how to estimate statistics over segmentations (e.g., mean region size) directly from the affinity graph. They use this to produce segmentations that are more *central* with respect to other possible segmentations.

5.5 Graph cuts and energy-based methods

A common theme in image segmentation algorithms is the desire to group pixels that have similar appearance (statistics) and to have the boundaries between pixels in different regions be of short length and across visible discontinuities. If we restrict the boundary measurements to be between immediate neighbors and compute region membership statistics by summing over pixels, we can formulate this as a classic pixel-based energy function using either a *variational formulation* (regularization, see Section 3.7.1) or as a binary Markov random field (Section 3.7.2).

Examples of the continuous approach include (Mumford and Shah 1989; Chan and Vese 1992; Zhu and Yuille 1996; Tabb and Ahuja 1997) along with the level set approaches discussed in Section 5.1.4. An early example of a discrete labeling problem that combines both region-based and boundary-based energy terms is the work of Leclerc (1989), who used minimum description length (MDL) coding to derive the energy function being minimized. Boykov and Funka-Lea (2006) present a wonderful survey of various energy-based techniques for binary object segmentation, some of which we discuss below.

As we saw in Section 3.7.2, the energy corresponding to a segmentation problem can be

written (c.f. Equations (3.100) and (3.108–3.113)) as

$$E(f) = \sum_{i,j} E_r(i,j) + E_b(i,j), \tag{5.50}$$

where the region term

$$E_r(i,j) = E_S(I(i,j); R(f(i,j))) \tag{5.51}$$

is the negative log likelihood that pixel intensity (or color) $I(i,j)$ is consistent with the statistics of region $R(f(i,j))$ and the boundary term

$$E_b(i,j) = s_x(i,j)\delta(f(i,j) - f(i+1,j)) + s_y(i,j)\delta(f(i,j) - f(i,j+1)) \tag{5.52}$$

measures the inconsistency between $\mathcal{N}_4$ neighbors modulated by local horizontal and vertical smoothness terms $s_x(i,j)$ and $s_y(i,j)$.

Region statistics can be something as simple as the mean gray level or color (Leclerc 1989), in which case

$$E_S(I; \mu_k) = \|I - \mu_k\|^2. \tag{5.53}$$

Alternatively, they can be more complex, such as region intensity histograms (Boykov and Jolly 2001) or color Gaussian mixture models (Rother, Kolmogorov, and Blake 2004). For smoothness (boundary) terms, it is common to make the strength of the smoothness $s_x(i,j)$ inversely proportional to the local edge strength (Boykov, Veksler, and Zabih 2001).

Originally, energy-based segmentation problems were optimized using iterative gradient descent techniques, which were slow and prone to getting trapped in local minima. Boykov and Jolly (2001) were the first to apply the binary MRF optimization algorithm developed by Greig, Porteous, and Seheult (1989) to binary object segmentation.

In this approach, the user first delineates pixels in the background and foreground regions using a few strokes of an image brush (Figure 3.61). These pixels then become the *seeds* that tie nodes in the *S–T graph* to the source and sink labels S and T (Figure 5.23a). Seed pixels can also be used to estimate foreground and background region statistics (intensity or color histograms).

The capacities of the other edges in the graph are derived from the region and boundary energy terms, i.e., pixels that are more compatible with the foreground or background region get stronger connections to the respective source or sink; adjacent pixels with greater smoothness also get stronger links. Once the minimum-cut/maximum-flow problem has been solved using a polynomial time algorithm (Goldberg and Tarjan 1988; Boykov and Kolmogorov 2004), pixels on either side of the computed cut are labeled according to the source or sink to which they remain connected (Figure 5.23b). While graph cuts is just one of several known techniques for MRF energy minimization (Appendix B.5.4), it is still the one most commonly used for solving binary MRF problems.

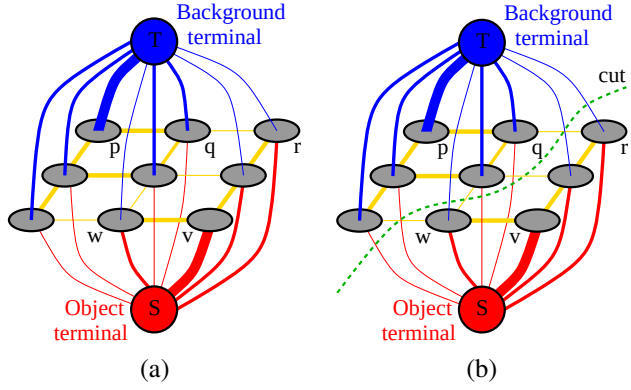

Figure 5.23 Graph cuts for region segmentation (Boykov and Jolly 2001) © 2001 IEEE: (a) the energy function is encoded as a maximum flow problem; (b) the minimum cut determines the region boundary.

Figure 5.24 GrabCut image segmentation (Rother, Kolmogorov, and Blake 2004) © 2004 ACM: (a) the user draws a bounding box in red; (b) the algorithm guesses color distributions for the object and background and performs a binary segmentation; (c) the process is repeated with better region statistics.

The basic binary segmentation algorithm of Boykov and Jolly (2001) has been extended in a number of directions. The *GrabCut* system of Rother, Kolmogorov, and Blake (2004) iteratively re-estimates the region statistics, which are modeled as a mixtures of Gaussians in color space. This allows their system to operate given minimal user input, such as a single bounding box (Figure 5.24a)—the background color model is initialized from a strip of pixels around the box outline. (The foreground color model is initialized from the interior pixels, but quickly converges to a better estimate of the object.) The user can also place additional strokes to refine the segmentation as the solution progresses. In more recent work, Cui, Yang, Wen *et al.* (2008) use color and edge models derived from previous segmentations of similar objects to improve the local models used in GrabCut.

Another major extension to the original binary segmentation formulation is the addition of

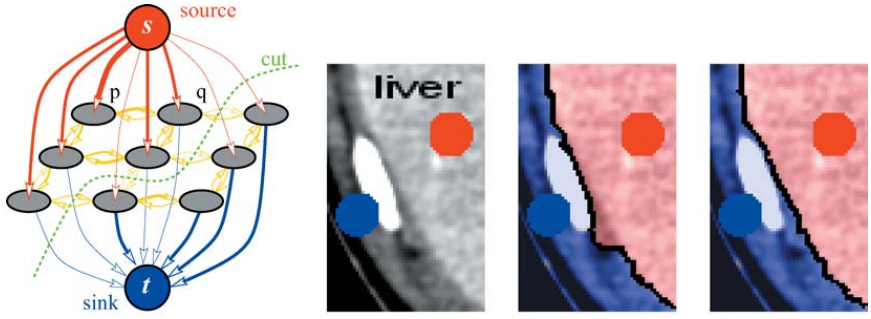

Figure 5.25 Segmentation with a directed graph cut (Boykov and Funka-Lea 2006) © 2006 Springer: (a) directed graph; (b) image with seed points; (c) the undirected graph incorrectly continues the boundary along the bright object; (d) the directed graph correctly segments the light gray region from its darker surround.

directed edges, which allows boundary regions to be oriented, e.g., to prefer light to dark transitions or *vice versa* (Kolmogorov and Boykov 2005). Figure 5.25 shows an example where the directed graph cut correctly segments the light gray liver from its dark gray surround. The same approach can be used to measure the *flux* exiting a region, i.e., the signed gradient projected normal to the region boundary. Combining oriented graphs with larger neighborhoods enables approximating continuous problems such as those traditionally solved using level sets in the globally optimal graph cut framework (Boykov and Kolmogorov 2003; Kolmogorov and Boykov 2005).

Even more recent developments in graph cut-based segmentation techniques include the addition of connectivity priors to force the foreground to be in a single piece (Vicente, Kolmogorov, and Rother 2008) and shape priors to use knowledge about an object's shape during the segmentation process (Lempitsky and Boykov 2007; Lempitsky, Blake, and Rother 2008).

While optimizing the binary MRF energy (5.50) requires the use of combinatorial optimization techniques, such as maximum flow, an approximate solution can be obtained by converting the binary energy terms into quadratic energy terms defined over a continuous $[0, 1]$ random field, which then becomes a classical membrane-based regularization problem (3.100–3.102). The resulting quadratic energy function can then be solved using standard linear system solvers (3.102–3.103), although if speed is an issue, you should use multigrid or one of its variants (Appendix A.5). Once the continuous solution has been computed, it can be thresholded at 0.5 to yield a binary segmentation.

The $[0, 1]$ continuous optimization problem can also be interpreted as computing the prob-

ability at each pixel that a *random walker* starting at that pixel ends up at one of the labeled seed pixels, which is also equivalent to computing the potential in a resistive grid where the resistors are equal to the edge weights (Grady 2006; Sinop and Grady 2007). K-way segmentations can also be computed by iterating through the seed labels, using a binary problem with one label set to 1 and all the others set to 0 to compute the relative membership probabilities for each pixel. In follow-on work, Grady and Ali (2008) use a precomputation of the eigenvectors of the linear system to make the solution with a novel set of seeds faster, which is related to the Laplacian matting problem presented in Section 10.4.3 (Levin, Acha, and Lischinski 2008). Couprie, Grady, Najman *et al.* (2009) relate the random walker to watersheds and other segmentation techniques. Singaraju, Grady, and Vidal (2008) add directed-edge constraints in order to support flux, which makes the energy piecewise quadratic and hence not solvable as a single linear system. The random walker algorithm can also be used to solve the Mumford–Shah segmentation problem (Grady and Alvino 2008) and to compute fast multigrid solutions (Grady 2008). A nice review of these techniques is given by Singaraju, Grady, Sinop *et al.* (2010).

An even faster way to compute a continuous $[0, 1]$ approximate segmentation is to compute *weighted geodesic distances* between the 0 and 1 seed regions (Bai and Sapiro 2009), which can also be used to estimate soft alpha mattes (Section 10.4.3). A related approach by Criminisi, Sharp, and Blake (2008) can be used to find fast approximate solutions to general binary Markov random field optimization problems.

5.5.1 *Application*: Medical image segmentation

One of the most promising applications of image segmentation is in the medical imaging domain, where it can be used to segment anatomical tissues for later quantitative analysis. Figure 5.25 shows a binary graph cut with directed edges being used to segment the liver tissue (light gray) from its surrounding bone (white) and muscle (dark gray) tissue. Figure 5.26 shows the segmentation of bones in a $256 \times 256 \times 119$ computed X-ray tomography (CT) volume. Without the powerful optimization techniques available in today's image segmentation algorithms, such processing used to require much more laborious manual tracing of individual X-ray slices.

The fields of medical image segmentation (McInerney and Terzopoulos 1996) and medical image registration (Kybic and Unser 2003) (Section 8.3.1) are rich research fields with their own specialized conferences, such as *Medical Imaging Computing and Computer Assisted Intervention (MICCAI)*,[11] and journals, such as *Medical Image Analysis* and *IEEE Transactions on Medical Imaging*. These can be great sources of references and ideas for research in this area.

[11] http://www.miccai.org/.

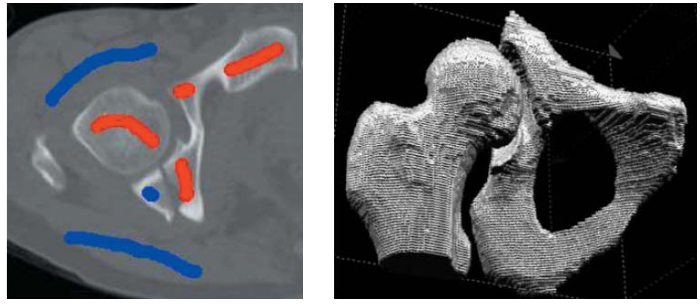

(a) (b)

Figure 5.26 3D volumetric medical image segmentation using graph cuts (Boykov and Funka-Lea 2006) © 2006 Springer: (a) computed tomography (CT) slice with some seeds; (b) recovered 3D volumetric bone model (on a $256 \times 256 \times 119$ voxel grid).

5.6 Additional reading

The topic of image segmentation is closely related to clustering techniques, which are treated in a number of monographs and review articles (Jain and Dubes 1988; Kaufman and Rousseeuw 1990; Jain, Duin, and Mao 2000; Jain, Topchy, Law *et al.* 2004). Some early segmentation techniques include those describerd by Brice and Fennema (1970); Pavlidis (1977); Riseman and Arbib (1977); Ohlander, Price, and Reddy (1978); Rosenfeld and Davis (1979); Haralick and Shapiro (1985), while examples of newer techniques are developed by Leclerc (1989); Mumford and Shah (1989); Shi and Malik (2000); Felzenszwalb and Huttenlocher (2004b).

Arbeláez, Maire, Fowlkes *et al.* (2010) provide a good review of automatic segmentation techniques and also compare their performance on the Berkeley Segmentation Dataset and Benchmark (Martin, Fowlkes, Tal *et al.* 2001).[12] Additional comparison papers and databases include those by Unnikrishnan, Pantofaru, and Hebert (2007); Alpert, Galun, Basri *et al.* (2007); Estrada and Jepson (2009).

The topic of active contours has a long history, beginning with the seminal work on snakes and other energy-minimizing variational methods (Kass, Witkin, and Terzopoulos 1988; Cootes, Cooper, Taylor *et al.* 1995; Blake and Isard 1998), continuing through techniques such as intelligent scissors (Mortensen and Barrett 1995, 1999; Pérez, Blake, and Gangnet 2001), and culminating in level sets (Malladi, Sethian, and Vemuri 1995; Caselles, Kimmel, and Sapiro 1997; Sethian 1999; Paragios and Deriche 2000; Sapiro 2001; Osher and Paragios 2003; Paragios, Faugeras, Chan *et al.* 2005; Cremers, Rousson, and Deriche 2007; Rousson and Paragios 2008; Paragios and Sgallari 2009), which are currently the most widely

[12] http://www.eecs.berkeley.edu/Research/Projects/CS/vision/grouping/segbench/.

used active contour methods.

Techniques for segmenting images based on local pixel similarities combined with aggregation or splitting methods include watersheds (Vincent and Soille 1991; Beare 2006; Arbeláez, Maire, Fowlkes *et al.* 2010), region splitting (Ohlander, Price, and Reddy 1978), region merging (Brice and Fennema 1970; Pavlidis and Liow 1990; Jain, Topchy, Law *et al.* 2004), as well as graph-based and probabilistic multi-scale approaches (Felzenszwalb and Huttenlocher 2004b; Alpert, Galun, Basri *et al.* 2007).

Mean-shift algorithms, which find modes (peaks) in a density function representation of the pixels, are presented by Comaniciu and Meer (2002); Paris and Durand (2007). Parametric mixtures of Gaussians can also be used to represent and segment such pixel densities (Bishop 2006; Ma, Derksen, Hong *et al.* 2007).

The seminal work on spectral (eigenvalue) methods for image segmentation is the *normalized cut* algorithm of Shi and Malik (2000). Related work includes that by Weiss (1999); Meilă and Shi (2000, 2001); Malik, Belongie, Leung *et al.* (2001); Ng, Jordan, and Weiss (2001); Yu and Shi (2003); Cour, Bénézit, and Shi (2005); Sharon, Galun, Sharon *et al.* (2006); Tolliver and Miller (2006); Wang and Oliensis (2010).

Continuous-energy-based (variational) approaches to interactive segmentation include Leclerc (1989); Mumford and Shah (1989); Chan and Vese (1992); Zhu and Yuille (1996); Tabb and Ahuja (1997). Discrete variants of such problems are usually optimized using binary graph cuts or other combinatorial energy minimization methods (Boykov and Jolly 2001; Boykov and Kolmogorov 2003; Rother, Kolmogorov, and Blake 2004; Kolmogorov and Boykov 2005; Cui, Yang, Wen *et al.* 2008; Vicente, Kolmogorov, and Rother 2008; Lempitsky and Boykov 2007; Lempitsky, Blake, and Rother 2008), although continuous optimization techniques followed by thresholding can also be used (Grady 2006; Grady and Ali 2008; Singaraju, Grady, and Vidal 2008; Criminisi, Sharp, and Blake 2008; Grady 2008; Bai and Sapiro 2009; Couprie, Grady, Najman *et al.* 2009). Boykov and Funka-Lea (2006) present a good survey of various energy-based techniques for binary object segmentation.

5.7 Exercises

Ex 5.1: Snake evolution Prove that, in the absence of external forces, a snake will always shrink to a small circle and eventually a single point, regardless of whether first- or second-order smoothness (or some combination) is used.

(Hint: If you can show that the evolution of the $x(s)$ and $y(s)$ components are independent, you can analyze the 1D case more easily.)

Ex 5.2: Snake tracker Implement a snake-based contour tracker: